# Stability of wurtzite, unbuckled wurtzite, and rocksalt phases of SiC, GaN, InN, ZnO, and CdSe under loading of different triaxialities

K. Sarasamak, A. J. Kulkarni, M. Zhou, and S. Limpijumnong 1

<sup>1</sup>School of Physics, Suranaree University of Technology and National Synchrotron Research Center, Nakhon Ratchasima 30000, Thailand <sup>2</sup>The George W. Woodruff School of Mechanical Engineering, Georgia Institute of Technology, Atlanta, Georgia 30332-0405, USA (Received 29 August 2007; revised manuscript received 16 November 2007; published 7 January 2008)

First principles calculations are carried to study the structural stability of SiC, GaN, InN, ZnO, and CdSe which are found to transform from a fourfold coordinated *wurtzite* (WZ) structure under ambient conditions to two different crystalline structures under loading of different triaxialities. Under hydrostatic compression, transformation into a sixfold coordinated *rocksalt* (RS) structure occurs, and under uniaxial compression along the [0001] direction and uniaxial tension along the [01 $\bar{1}$ 0] crystalline direction (except SiC and GaN), transformation into a fivefold coordinated *unbuckled wurtzite* phase (HX) is observed. The lack of the WZ $\rightarrow$ HX transformation for SiC and GaN under uniaxial tension along the [01 $\bar{1}$ 0] direction is because for these two materials the tensile stress required for the enthalpy of HX to become lower than the enthalpy of WZ is higher than their corresponding ultimate tensile strength. Critical stress levels for the transformations are found to depend on the formation energies of the WZ, HX, and RS structures which in turn are related to the ionicity of each material. The transformations are a manifestation of the tension-compression response asymmetry of these materials.

### DOI: 10.1103/PhysRevB.77.024104 PACS number(s): 61.50.Ks, 62.20.-x, 64.70.K-

### I. INTRODUCTION

One-to-one binary compounds obeying the octet rule (i.e., I-VII, II-VI, III-V, or IV-IV materials) are generally semiconductors or insulators. Although these type AB compounds have the same chemical formula units, their crystal structures under ambient conditions show significant variations with bond ionicity. While highly ionic compounds such as CsCl (I-VII) prefer dense crystal structures with a coordination number of 8 (CN=8), compounds such as NaCl (also I-VII) with lower degrees of ionicity gravitate toward the rocksalt (RS) structure  $(Fm\bar{3}m$  space group) with CN=6. As the degree of ionicity decreases (shifting toward covalent bonding states), compounds such as ZnO (II-VI), GaN (III-V), and SiC (IV-IV) stabilize in wurtzite (WZ) (P63mc) structures with CN=4. In such covalent compounds, the valence electron counting (two electrons in each bond) is satisfied through the formation of four bonds for each atom. However, in compounds with higher degrees of ionicity such as CsCl and NaCl, the gain in cation-anion attractions leads to the formation of structures with higher CN. Nevertheless, bond ionicity should not be considered as the only factor in determining crystalline structures in such compounds since the assumption of a particular structure also depends on intrinsic factors such as composition, band structure, valence electrons, bonding states, and structural symmetries. Extrinsic factors such as loading and temperature also play significant roles.

Calculations and experiments have been carried out to study the structural stabilities of these materials. Over two decades ago, first principles calculations have been used to evaluate the formation energies of different crystalline structures (see, e.g., Refs. 1 and 2). X-ray diffraction experiments have been used to determine the natural occurring structures. Consequently, the stable crystalline structures under ambient conditions are well established (for a comprehensive review,

see Ref. 3). Furthermore, advances in experimental techniques, such as the use of intense and tunable x ray from synchrotron radiation, have also allowed x-ray diffraction analyses under external loading. For hydrostatic compression, it is observed that most materials with low CN structures (e.g., WZ and ZB) transform into a more compressed crystalline form with higher CN structures (e.g., RS).<sup>3–13</sup> First principles and empirical potential calculations have yielded phase equilibrium pressures that are comparable but always lower than the transformation pressures measured from experiments.<sup>3,14–23</sup> The higher experimental values are attributed to the existence of an energy barrier between the phases for each transformation. This finding is supported by, for example, the observation that critical pressure for the upward WZ→RS transformation is higher than the critical pressure for the downward RS→WZ transformation<sup>3,18</sup> or the trapping of nanocrystallite ZnO in the RS phase under ambient condition after a high heat-high pressure treatment.24 If there was no transformation barrier, the upward and downward transformations would occur at the same pressure and there would be no trapping of the metastable high pressure phase.

The recent synthesis of quasi-one-dimensional nanostructures such as nanowires, nanobelts, and nanorods of GaN, ZnO, and CdSe (see, e.g., Refs. 25 and 26) necessitates understanding the response of such materials to uniaxial loading. These nanostructures are single crystalline and nearly defect-free and, therefore, are endowed with high strengths and the ability to undergo large deformations without failure. Also, their high surface-to-volume ratios enhance atomic mobility and promote phase transformations under loading. A novel fivefold coordinated *unbuckled wurtzite* phase (HX) within the  $P6_3/mmc$  space group was observed in  $[01\bar{1}0]$ -oriented ZnO nanowires under uniaxial tensile loading. The stability of this novel phase and the stabilities of WZ and RS phases of ZnO under uniaxial tension

along the [0110] direction as well as hydrostatic compression were analyzed through enthalpy calculations. It is found that the HX structure cannot be stabilized by a hydrostatic pressure. Instead, both empirical potential based molecular dynamics (EP-MD) simulations and first principles calculations showed that transformation into the HX structure can occur under either tensile loading along the  $[01\overline{1}0]$  direction or compressive loading along the [0001] direction of sufficient magnitude. For this WZ-HX transformation, the uniaxial stress deforms the crystal in only one direction. Since the unit cell of HX is significantly shorter than the unit cell of WZ in the c or [0001] direction (details later), either compression along the c direction or tension along the perpendicular [0110] direction can cause the transformation. For compression along the c direction, the corresponding contribution to enthalpy by mechanical work is linearly proportional to  $-\sigma_c \Delta c$ , with  $\sigma_c$  and  $\Delta c$  being the compressive stress and the change in unit cell size in the c direction, respectively. For tension along the b direction, the corresponding contribution to enthalpy by mechanical work is linearly proportional to  $-\sigma_b \Delta b$ , with  $\sigma_b$  and  $\Delta b$  being the tensile stress and the change in unit cell size in the b direction, respectively. In contrast, for the WZ \rightarrow RS transformation, the all around external pressure uniformly compresses the WZ crystal in all directions and causes it to collapse into the RS phase which has a lower equilibrium unit cell volume. The mechanical work contribution to enthalpy is  $p\Delta V$ , with p and  $\Delta V$  being the external pressure and volume reduction, respectively. The discovery of the novel HX phase has subsequently been confirmed in [0001]-oriented ZnO nanoplates<sup>29</sup> and nanowires.<sup>30</sup>

To gain insight into the existence of the WZ, HX, and RS structures in materials with different ionicities, we analyze here the energetic favorability of these phases for ZnO and CdSe (groups II-VI), GaN and InN (III-V), and SiC (IV-IV) under uniaxial loading along the  $[01\bar{1}0]$  and [0001] crystalline axes as well as under hydrostatic compression. The likelihood of transformations from WZ into HX or RS and the effort of load triaxialities on the transformations are analyzed.

### II. CRYSTAL STRUCTURES

The natural form of the five materials studied is wurtzite, as shown in Fig. 1 (left column). This structure is quantified customarily by the lattice constant a, the c/a ratio, and the internal parameter u which specifies the relative distance along the c axis between the two hexagonal-close-packed cation and anion sublattices. To describe the HX and RS structures and the transformation from WZ to each of these phases, an extra lattice parameter b and an internal parameter v are introduced. v0 defines the horizontal distance along the v0 axis between the cation and anion sublattices. Out of the five parameters v0 and v0 illustrated in Fig. 1, only the three external ones v0 and v0 can be directly manipulated through applied loading. The two internal parameters v0 and v0 cannot be varied directly. These parameters are determined such that, for any given configuration,

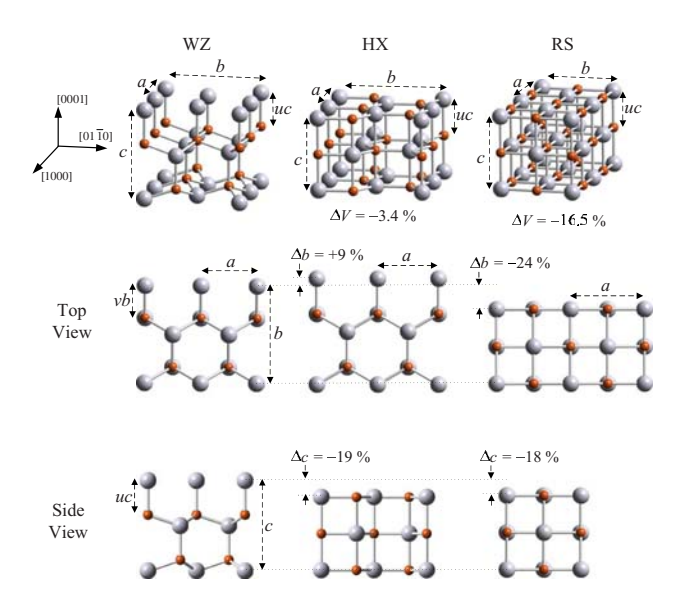


FIG. 1. (Color online) Schematic illustration of the WZ, HX, and RS structures: small spheres represent anions and large spheres represent cations. The middle and bottom rows show top view and side view, respectively. Parameters a, b, c, u, and v are indicated. For realistic rendering, the images shown are drawn to scale using parameters for ZnO at equilibrium conditions, i.e., ambient pressure for WZ,  $\sigma = -\sigma_c^{eq}$  for HX, and  $p = p^{eq}$  for RS.  $\Delta V$ ,  $\Delta b$ , and  $\Delta c$  are the percentage changes in V (volume), b, and c relative to the same quantities for WZ.

the net forces on all atoms in the unit cell vanish. An analysis of the variations of u with c/a and v with b/a can be found in Refs. 19 and 20. The three structures are significantly different, with  $c/a \approx 1.63$  and  $b/a \approx 1.73$  for WZ,  $c/a \approx 1.20$  and  $b/a \approx 1.73$  for HX, and  $c/a \approx 1.00$  and  $b/a \approx 1.00$  for RS. The ideal values of c/a, b/a, u, and v for WZ, HX, and RS under no load and zero temperature are listed in Table I. The c/a value for HX is obtained via enthalpy minimization. All other parameters are determined from the geometry of each structure, for instance, perfect tetrahedral coordination for WZ and perfect cubic for RS. Actual values of these parameters can deviate from those in the table, depending on the material, loading, and temperature.

### III. COMPUTATIONAL METHOD

First principles calculations are carried out to evaluate the total energy of each material in its natural and deformed

TABLE I. Ideal lattice parameters for WZ, HX, and RS crystal-line structures.

Parameters	WZ	HX	RS
c/a	$\sqrt{8/3} = 1.63$	1.20	1.00
и	3/8 = 0.37	0.50	0.50
b/a	$\sqrt{3} = 1.73$	$\sqrt{3} = 1.73$	1.00
v	1/3 = 0.33	1/3 = 0.33	0.50

states. The calculations are based on the density functional theory (DFT) with local density approximation (LDA) and ultrasoft pseudopotentials,  $^{31}$  as implemented in the VASP code.  $^{32}$  Test calculations have shown that generalize gradient approximations (GGAs) give the results that are qualitatively the same as LDA.  $^{33}$  Zinc  $^{3}$ d, gallium  $^{3}$ d, indium  $^{4}$ d, and cadmium  $^{4}$ d electrons are treated as valence electrons. Cutoff energies for the plane wave expansion are 400 eV for ZnO, 180 eV for CdSe, 350 eV for nitrides, and 300 eV for SiC. The  $^{k}$ -point sampling set is based on a  $^{7}$ ×7 division of the reciprocal unit cell based on the Monkhorst-Pack scheme  $^{34}$  with the  $^{\Gamma}$  point included, which gives approximately 100 inequivalent  $^{k}$  points.

The stability of each crystal structure and compound can be determined by analyzing enthalpy as a function of c/a and b/a. The enthalpy per a *wurtzite unit cell* under uniaxial loading is

$$H(c/a,b/a) = E(c,b,a,u,v) - A_{ik}\sigma_i q_i, \tag{1}$$

where E is the formation energy per wurtzite unit cell,  $\sigma_i$  is the stress along the i direction,  $q_i$  is the lattice parameter in the i direction,  $A_{jk}$  is the cross section area of the unit cell perpendicular to the stress direction, and  $A_{jk}\sigma_iq_i$  (summation not implied) is the external work. For tension along the b axis, i=b,  $A_{ac}=ac/2$ , and  $q_b=b$ , with  $\sigma_b$  being the tensile stress. For compression along the c axis, c axis, c and c being the compressive stress. For hydrostatic compression, the enthalpy is

$$H(c/a, b/a) = E(c, b, a, u, v) + pV,$$
 (2)

where p and V=abc/2 are the pressure and unit cell volume, respectively. Under ambient pressure, the enthalpy is equal to the internal formation energy. Note that a wurtzite unit cell contains two cation-anion pairs, i.e., 2 f.u. and occupy the volume V=abc/2.

For each c/a and b/a pair, the internal parameters u and v and the unit cell volume V are allowed to relax so that the configuration that yields the minimum H is obtained. For a given load condition, the minima on the enthalpy surface with c/a and b/a as the independent variables identify the corresponding stable and metastable structures. For the analyses at hand, the parameter ranges considered are [1.00, 1.63] for c/a and [1.00, 1.73] for b/a, with the increments of 0.05 for c/a and 0.10 for b/a. This meshing of the structural space results in approximately 170 strained configurations. For tensile loading along the b direction, additional configurations with b/a up to 2.30 are also investigated, increasing the number of total configurations to 200. Out of these 170 configurations, or those around (c/a,b/a) $\approx$  (1.63, 1.73), (1.2, 1.73), and (1.00, 1.00) are more carefully analyzed since these three parameter sets define the neighborhoods of stable WZ, HX, and RS structures, respectively, for the given load condition.

For each strained configuration (each c/a-b/a pair), the energies associated with at least four different unit cell volumes are calculated. An equation of state (energy-volume relation) is obtained by a third-degree polynomial fit. Under loading, the volume that minimizes H is not the same as the volume that minimizes E. The equation of state allows the

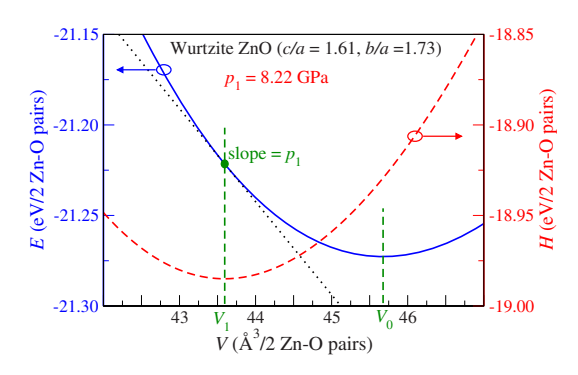


FIG. 2. (Color online) Energy (solid curve) and enthalpy (dashed curve) as functions of volume for wurtzite (c/a=1.61 and b/a=1.73) ZnO. At hydrostatic pressure  $p_1=8.22$  GPa, the volume that minimizes enthalpy ( $V_1$ ) is smaller than the volume at ambient pressure ( $V_0$ ).

minimum enthalpy for each combination of c/a-b/a pair and loading condition to be obtained. As an illustration, the energy and enthalpy are shown in Fig. 2 as functions of volume for WZ ZnO (c/a=1.61 and b/a=1.73) under hydrostatic pressure. At ambient pressure (p $\approx$ 0), the energy and enthalpy are equal and the minimum enthalpy is equal to  $E(V_0)$ , with  $V_0$  being the equilibrium volume of WZ in a stress-free state. At p= $p_1$ , the minimum enthalpy occurs at V= $V_1$  for which dE/dV= $-p_1$ .

### IV. RESULTS AND DISCUSSIONS

### A. Ambient conditions (stress-free state)

Figure 3(a) shows the energy (or enthalpy at zero external loading) landscape for ZnO. The global minimum occurs at the wurtzite structure with (c/a,b/a)=(1.61,1.73). The sections of the surface along b/a=1.73 (solid line) and 1.00 (dash line) are shown in Fig. 3(b). By virtue of symmetry, b/a is fixed at  $\sqrt{3} \approx 1.73$ ) for WZ and HX and at 1.00 for RS. Clearly, in stress-free state, WZ is the most stable structure with the lowest energy, HX has higher energy and is not stable (no local minimum), and the RS structure is metastable with a high energy. For CdSe, GaN, InN, and SiC, the shapes of the energy landscapes (not shown but can be found online<sup>35</sup>) are similar to that of ZnO. Their two-dimensional (2D) sections at b/a=1.73 and 1.00 are shown in Fig. 4. The energy difference (see Ref. 36) between HX and WZ  $(\Delta E^{\text{HX-WZ}})$  and that between RS and WZ  $(\Delta E^{\text{RS-WZ}})$  are tabulated in Table II. The energies of the three phases for all compounds except CdSe follow the order of  $E^{RS} > E^{HX} > \hat{E}^{WZ}$ . For CdSe,  $E^{RS} < E^{HX}$ . This exception can be attributed to the fact that for compounds such as CdSe with high ionicity, the energy differences between RS, HX, and WZ are relatively small. Under this situation, other effects, such as energy cost for bond distortions, can affect the ordering in energies.

There are significant variations of  $\Delta E^{\rm HX-WZ}$  or  $\Delta E^{\rm RS-WZ}$  among the materials, partly reflecting differences in the ionicity. Several indices are available to describe the ionicity of materials. Although LDA calculation is sometimes believed

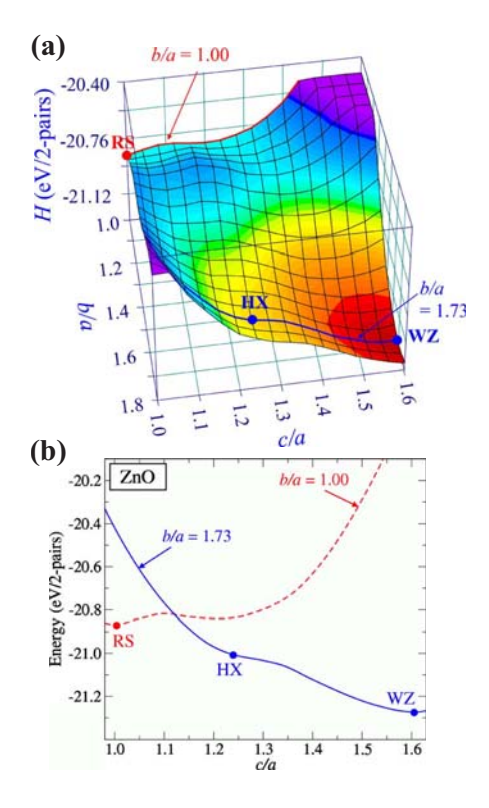


FIG. 3. (Color online) (a) Energy (E) (or enthalpy H under zero external loading) landscape for ZnO (in eV per wurtzite unit cell which contains two cation-anion pairs or 2 f.u.). Each point on the surface represents the minimum energy for a given combination of c/a and b/a. To arrive at the minimum, u, v, and V are allowed to relax while a, b, and c are kept constant. Energy levels above -20.50 eV are truncated as they are not of interest in the discussions here. (b) 2D sections of the energy surface for b/a=1.73 (solid line) and 1.00 (dashed line).

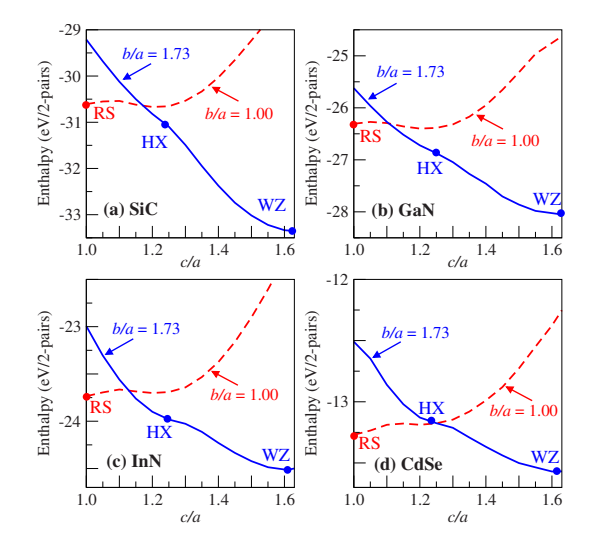


FIG. 4. (Color online) 2D sections of (a) SiC, (b) GaN, (c) InN, and (d) CdSe energy surfaces (Ref. 35) for b/a=1.73 (solid lines) and 1.00 (dashed lines).

TABLE II. Energy difference (eV/2 pairs) between HX (or RS) and the WZ structure. The Phillips ionicity parameters  $(f_i)$  are also listed. (Ref. 37).

Compounds	Phillips' $f_i$	$E^{\mathrm{HX}} - E^{\mathrm{WZ}}$ (eV)	$E^{\text{RS}} - E^{\text{WZ}}$ (eV)
SiC	0.177	2.53	2.74
GaN	0.500	1.32	1.74
InN	0.578	0.61	0.78
ZnO	0.616	0.26	0.41
CdSe	0.699	0.44	0.30

to slightly overestimate the ionicity in materials, the trend of ionicity between materials should be qualitatively correct. Therefore, Phillips' ionic scale  $(f_i)^{37}$  which has the range between 0 (the least ionic) and 1(the most ionic), is used here by choice. The values of  $f_i$  for the compounds studied here are listed in Table II.37 The variations of  $\Delta E^{\mathrm{HX-WZ}}$  and  $\Delta E^{\text{RS-WZ}}$  with  $f_i$  are shown in Fig. 5. For RS,  $\Delta E^{\text{RS-WZ}}$  (solid line) decreases monotonically as  $f_i$  increases. For HX,  $\Delta E^{\text{HX-WZ}}$  (dash line) decreases monotonically with  $f_i$  (except for CdSe). This is expected because compounds with higher levels of ionicity can significantly lower their energies through increases in CN. While ionicity is not the only factor that determines the relative stability of crystal structures, it clearly affects the stability of structures. For covalent compounds (e.g., SiC and GaN), the structure with fourfold coordination is highly favored, resulting in large differences between the formation energies of RS (sixfold) and WZ (fourfold) and between the formation energies of HX (fivefold) and WZ. On the other hand, for compounds with higher levels of ionicity, the differences in formation energies among RS, HX, and WZ are lower. In this paper, only ionic compounds that have fourfold coordinated structures (WZ) under ambient conditions are considered.

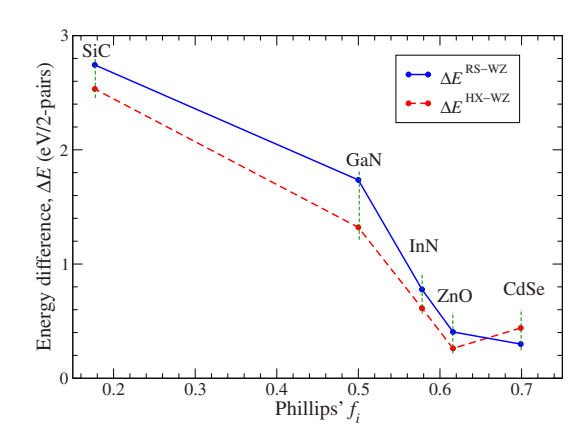


FIG. 5. (Color online) Correlation between the formation energy differences ( $\Delta E$ ) and the ionicity as quantified by Phillips'  $f_i$  for SiC, GaN, InN, ZnO, and CdSe.  $\Delta E^{\rm RS-WZ}$  is shown in solid line and  $\Delta E^{\rm HX-WZ}$  is shown in dash line. For all compounds, WZ has the lowest energy and RS has the highest energy, except for CdSe whose RS phase has a slightly lower energy than its HX phase.

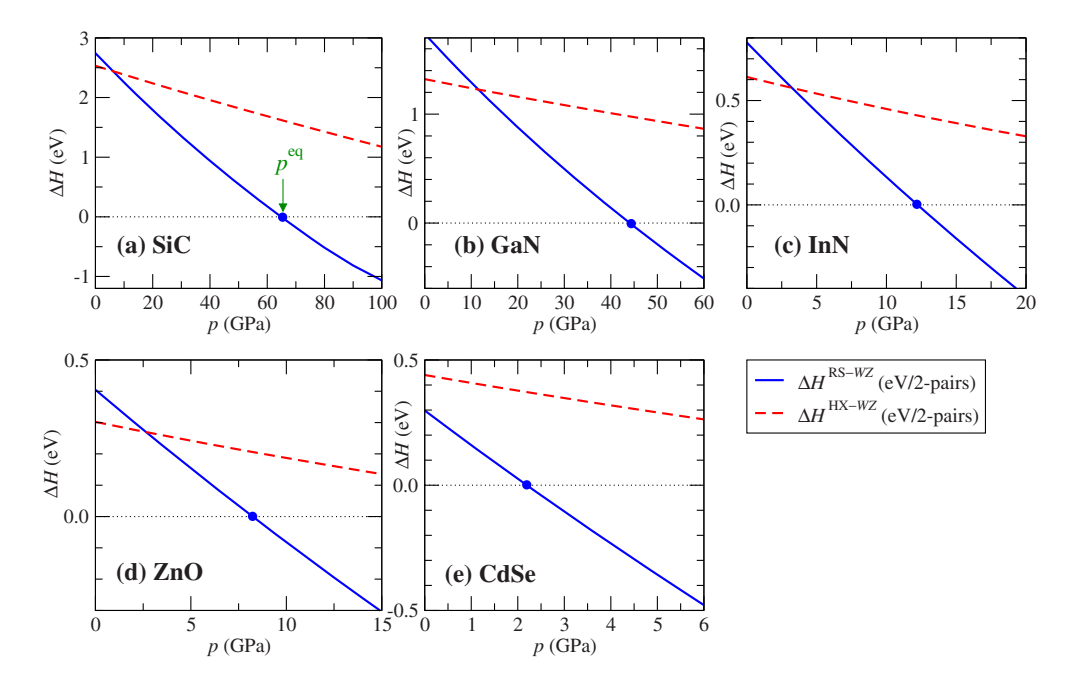


FIG. 6. (Color online) Enthalpy differences ( $\Delta H$ ), in the unit of eV/2 pairs, between RS and WZ (solid line) and HX and WZ (dashed line) as a function of hydrostatic pressure for (a) SiC, (b) GaN, (c) InN, (d) ZnO, and (e) CdSe. As the pressure reaches the equilibrium value ( $p^{eq}$ , indicated by solid dots), the enthalpies for RS and WZ become equal. Above  $p^{eq}$ , RS is more stable. Note that HX is never stable under hydrostatic loading.

### B. Hydrostatic compression

Sufficiently high pressures can cause the WZ structure to collapse into the denser RS phase. As shown in Fig. 1, the volume of the RS structure is  $\sim 17\%$  smaller than the volume of the WZ structure ( $\Delta V \approx -0.17V_0$ , with  $V_0$  being the equilibrium volume of WZ). For a given constant pressure p, the difference in contributions to enthalpy by mechanical work between RS and WZ is approximately  $p\Delta V$  (neglecting the difference in bulk moduli of the two phases). If p is sufficiently high, mechanical work can overcome the formation energy difference, driving the transformation forward. Figure 6 shows  $\Delta H^{\rm RS-WZ} = H^{\rm RS} - H^{\rm WZ}$  and  $\Delta H^{\rm HX-WZ} = H^{\rm HX} - H^{\rm WZ}$  as functions of p for the five compounds studied. The rather linear trends confirm that the bulk moduli of the WZ, HX, and RS phases are quite comparable. The slight deviation from linearity of  $\Delta H^{\rm RS-WZ}$  reflects the fact that the bulk modulus of RS is somewhat higher (approximately 25%) than that of WZ. Note that the slope of the  $\Delta H^{\text{RS-WZ}}$  line is approximately five times that of the  $\Delta H^{\text{HX-WZ}}$  line, consistent with the fact that the volume decrease associated with the WZ→RS transformation (17%) is approximately five times of that associated with the WZ-HX transformation (3.6%).

The equilibrium pressure  $p^{eq}$  between the WZ and RS structures (the pressure at which the enthalpies of RS and WZ become equal) can be obtained by examining the enthalpy surfaces at several pressures. This pressure is identified with the intercept of the enthalpy curve with the horizontal axis in Fig. 6. The enthalpy surfaces of all five materials at their equilibrium pressure  $p^{eq}$  are qualitatively the same (not shown here but can be found online<sup>35</sup>). There-

fore, we choose to present only the enthalpy surface for InN in Fig. 7(a). The corresponding 2D section is shown in Fig. 7(b). At  $p < p^{eq}$ , WZ has the lowest enthalpy. As p is increased above  $p^{eq}$ , RS has a lower enthalpy than WZ.  $p^{eq}$ depends strongly on the ionicity of the compound. This is expected because the initial energy difference between WZ and RS ( $\Delta E^{\text{RS-WZ}} = E^{\text{RS}} - E^{\text{WZ}}$ ) depends on the ionicity of the material (from  $\Delta E^{\text{RS-WZ}} = 2.74 \text{ eV}$  for SiC to 0.30 eV for CdSe). SiC has the highest  $\Delta E^{\text{RS-WZ}}$  and therefore the highest  $p^{\text{eq}}$  (64.9 GPa). CdSe has the lowest  $\Delta E^{\text{RS-WZ}}$  and therefore the lowest  $p^{eq}$  (2.2 GPa). The equilibrium pressures of the five materials are listed in Table III. Our calculated equilibrium pressures are in good agreement with other calculated results in general (see Table III). To compare with experiments, one should not directly compare the calculated equilibrium pressure with either the critical pressures of the upward or downward WZ to RS transformations. This is because there is a transformation barrier between the two phases that causes the upward critical pressure to be higher (and the downward critical pressure to be lower) than the equilibrium pressure.<sup>3,18</sup> The averages between the upward and downward critical pressures, shown as  $p_t$  in Table III, are shown as an approximate experimental equilibrium pressures and are in good agreement with the calculated equilibrium pressures.

To gain insight on the transformation enthalpy barrier, we extracted (from the plots) the *homogeneous* transformation barrier (in the unit of eV/2 pairs) of these five materials and tabulated in Table III using square brackets. The barrier for ZnO of 0.30 eV/2 pairs is the same as Limpijumnong and Jungthawan have previously reported. <sup>18</sup> The barriers for SiC and GaN of 1.26 and 0.76 eV/2 pairs are in good agreement

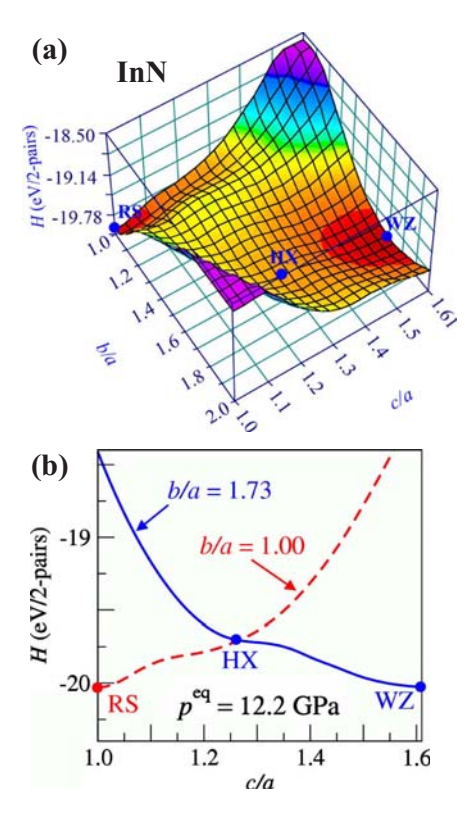


FIG. 7. (Color online) (a) Enthalpy surface maps (in eV/2 pairs) for InN at its RS-WZ equilibrium pressures,  $p^{\rm eq}$ =12.2 GPa. (b) 2D sections of the enthalpy surface for b/a=1.73 (solid line) and 1.00 (dashed line).

with the calculated values reported by Miao and Lambrecht<sup>38</sup> (for SiC) of 1.2 eV/2 pairs and by Limpijumnong and Lambrecht<sup>20</sup> (for GaN) of 0.9 eV/2 pairs. We can see that the magnitude of the barrier increases with the zero pressure energy difference between phases ( $\Delta E^{\rm RS-WZ}$ ), hence the ionicity. The detailed investigation of the barriers will be a subject of further study on more materials in the future.

Figure 8 shows the variation of equilibrium pressure with the initial energy difference. An approximately linear dependence of  $p^{\rm eq}$  on  $\Delta E^{\rm RS-WZ}$  is seen. The linear fit gives

$$p^{\text{eq}} \approx 25.97(\Delta E^{\text{RS-WZ}}) - 4.68.$$
 (3)

The units of  $p^{\rm eq}$  and  $\Delta E^{\rm RS-WZ}$  are in GPa and eV/2 pairs, respectively. This approximate universal relationship can be used to estimate the difference in the formation energy of the RS and WZ phases when the equilibrium pressure is known or vice versa.

Figure 6 also shows that the  $\Delta H^{\text{HX-WZ}}$  line never intercepts the horizontal axis for all five materials over the pressure range analyzed. Obviously, HX is not a thermodynamically stable structure under hydrostatic compression and the WZ $\rightarrow$ HX transformation does not occur for such conditions.

### C. Uniaxial compression along the [0001] direction

Figure 1 shows that HX has a lattice constant c significantly shorter ( $\sim$ 19%) than that of WZ in the [0001] direc-

TABLE III. Equilibrium pressure, transformation barrier, and stresses for SiC, GaN, InN, ZnO, and CdSe for the WZ $\rightarrow$ RS and WZ $\rightarrow$ HX transformations.  $p^{\rm eq}$  is the hydrostatic pressure that establishes the equilibrium between the WZ and RS structures and  $p_{\rm t}$  (reported here as an average between the experimental upward and downward pressure of transformations) is the corresponding experimental value.  $-\sigma_c^{\rm eq}$  ( $\sigma_b^{\rm eq}$ ) is the value of the compressive (tensile) force per unit area along the c direction (b direction) at which the WZ and HX structures are in equilibrium. For CdSe, although  $-\sigma_c^{\rm eq}=3.8$  GPa provides equilibrium between the WZ and HX phases, the RS phase has a lower enthalpy (hence more stable) under this condition. The transformation enthalpy barrier in eV/2 pairs between the WZ and RS phases at a given equilibrium pressure are given in square brackets following  $p^{\rm eq}$  in the same column.

		RS			НХ	
Material	p <sup>eq</sup> (GPa) (Present)	p <sup>eq</sup> (GPa) (Other)	P <sub>t</sub> (GPa) (Expt.)	$-\sigma_c^{\mathrm{eq}}$ (GPa)	$\sigma_b^{ m eq}$ (GPa)	
SiC	64.9[1.26]	60, <sup>a</sup> 66.6, <sup>b</sup> 66, <sup>c</sup> 92 <sup>d</sup>	67.5 <sup>e</sup>	60.5		
GaN	44.1[0.76]	51.8, <sup>f</sup> 42.9 <sup>g</sup>	52.2, <sup>h</sup> 31 <sup>i</sup>	30.5		
InN	12.2[0.51]	21.6, <sup>f</sup> 11.1 <sup>g</sup>	10, <sup>j</sup> 12.1 <sup>h</sup>	9.6	14.7	
ZnO	8.2[0.30]	6.6, <sup>k</sup> 9.3, <sup>l</sup> 8.0 <sup>m</sup>	5.5, <sup>n</sup> 8.5°	6.0	10.8	
CdSe	2.2[0.40]	2.5 <sup>p</sup>	2.1 <sup>q</sup>	3.8	5.8	

<sup>a</sup>DFT (GGA) calculations by Miao and Lambrecht (Ref. 41).

<sup>b</sup>DFT (LDA) calculations (of zincblende to RS) by Karch *et al.* (Ref. 17).

<sup>c</sup>DFT (LDA) calculations (of zincblende to RS) by Chang and Cohen (Ref. 42).

<sup>d</sup>DFT (B3Lyp) calculations (of zincblende to RS) by Catti (Ref. 43). <sup>e</sup>Synchrotron angle dispersive x-ray diffraction (ADX) experiment by Yoshida *et al.* (Ref. 10).

<sup>f</sup>DFT (LDA) calculations by Christensen and Gorczyca (Ref. 14). <sup>g</sup>DFT (LDA) calculations by Serrano *et al.* (Ref. 44).

<sup>h</sup>ADX experiment by Ueno et al. (Ref. 6).

<sup>i</sup>Synchrotron energy-dispersive x-ray diffraction (EDX) by Xia *et al.* (Ref. 8).

<sup>j</sup>Synchrotron EDX experiment by Xia et al. (Ref. 9).

<sup>k</sup>DFT (LDA) calculations by Jaffe et al. (Ref. 16).

<sup>1</sup>DFT (GGA) calculations by Jaffe *et al.* (Ref. 16).

<sup>m</sup>DFT (GGA) calculations by Ahuja et al. (Ref. 45).

<sup>n</sup>Synchrotron EDX experiment by Desgreniers. (Ref. 5).

<sup>o</sup>Synchrotron EDX experiment by Recio et al. (Ref. 46).

PDFT (LDA) calculations by Côté et al. (Ref. 23).

<sup>q</sup>EDX experiment by Cline and Stephens (Ref. 4).

tion. This difference allows WZ to transform into HX via compression in the c direction. Under constant compressive stess  $-\sigma_c$  (negative sign indicates compression), the mechanical contribution to the enthalpy difference between WZ and HX is  $-A_{ab}\sigma_c\Delta c$ , where  $\Delta c \approx -0.19c$ . A sufficiently high  $-\sigma_c$  would allow mechanical work to offset the energy difference between HX and WZ, affecting the transformation into the HX structure. The shapes of the enthalpy surfaces for SiC, GaN, InN, and ZnO at their respective equilibrium compressive stress  $-\sigma_c^{eq}$  are qualitatively the same (not shown here but can be found online 35). Therefore, we choose

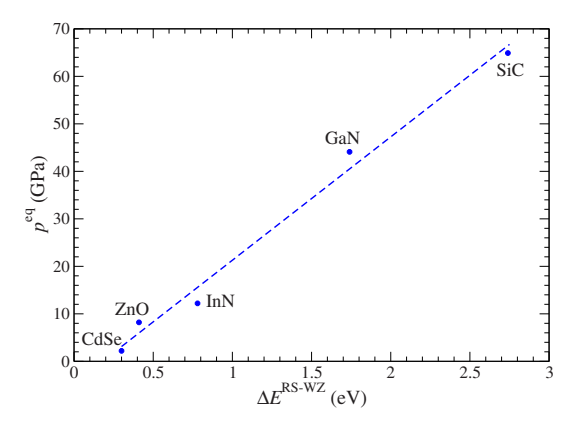


FIG. 8. (Color online) Correlation between equilibrium hydrostatic pressure  $(p^{\rm eq})$  and the difference in energy  $(\Delta E)$  between the RS and WZ phases of the five materials.  $p^{\rm eq}$  is the pressure at which the WZ and RS structures are in equilibrium, as illustrated in Fig. 6 and tabulated in Table III. The energy difference  $\Delta E = E^{\rm RS} - E^{\rm WZ}$  is calculated under the conditions of zero external loading and is tabulated in Table II.

to present the enthalpy surface for InN with a 2D section plot in Fig. 9(a). The stability of the HX phase can be better analyzed through the enthalpy difference  $\Delta H^{\rm HX-WZ} = H^{\rm HX} - H^{\rm WZ}$  as a function of the compressive stress along the c direction (dashed lines, Fig. 10). If the elastic moduli of HX and WZ along the c direction are assumed to be equal,  $\Delta H$  would vary linearly with  $-\sigma_c$  with an approximate slope of  $A_{ab}\Delta c \approx -0.19(abc/2) \approx -0.19V$ . Figure 10 also shows the enthalpy difference between RS and WZ,  $\Delta H^{\rm RS-WZ} = H^{\rm RS} - H^{\rm WZ}$  (solid lines). Note that  $\Delta H^{\rm HX-WZ}$  and  $\Delta H^{\rm RS-WZ}$ 

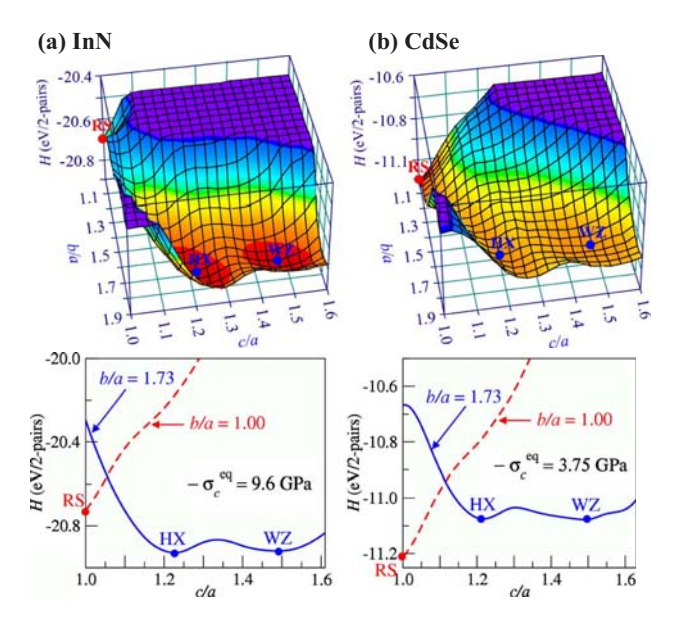


FIG. 9. (Color online) Enthalpy surface maps for (a) InN and (b) CdSe at their respective HX-WZ equilibrium c direction stress  $(-\sigma_c^{\text{eq}})$ . Their 2D sections for b/a=1.73 (solid line) and 1.00 (dashed line) are also shown in the bottom panel. Note that, unlike other materials studied here, CdSe favors RS over HX phase under c-direction stress.

show similar trends, with similar slopes. This is because for the WZ $\rightarrow$ RS transformation,  $\Delta c/c \approx 18\%$ , while for the WZ $\rightarrow$ HX transformation,  $\Delta c/c \approx 19\%$ .

For all materials except CdSe,  $\Delta H^{\rm HX-WZ}$  is always lower than  $\Delta H^{\text{RS-WZ}}$ , indicating that HX is more stable than RS under compression in the c direction. For CdSe, where initially (i.e., under no load condition) the RS phase has a slightly lower energy than HX,  $\Delta H^{RS-WZ}$  is always lower than  $\Delta H^{\rm HX-WZ}$ , indicating that RS is the preferred structure over HX under uniaxial compression along the [0001] direction as well as under hydrostatic compression. As a result, the the enthalpy surface at  $-\sigma_c^{eq}$  of CdSe [Fig. 9(b)] is qualitatively different from those of the other four materials [represented by Fig. 9(a)], i.e., the RS phase has lower enthalpy. The equilibrium stress for the transformation  $(-\sigma_c^{eq})$  of each material is shown in Fig. 10. Below  $-\sigma_c^{eq}$ , WZ phase is stable. Above  $-\sigma_c^{eq}$ , HX is stable (RS for CdSe). The values of  $-\sigma_c^{\rm eq}$  depend on the initial energy difference  $(\Delta E)$ between WZ and HX and are listed in Table III. For SiC,  $\Delta E = E^{HX} - E^{WZ} = 2.53 \text{ eV}$ , the stress required to cause the  $HX \rightarrow WZ$  transformation is high  $(-\sigma_c^{eq} = 60.5 \text{ GPa})$ . On the other hand, for ZnO,  $\Delta E = 0.26$  eV and  $-\sigma_c^{eq} = 6.0$  GPa which is only 1/10 of the stress level required for SiC. This linear trend is clearly seen in Fig. 11 which shows  $-\sigma_c^{eq}$  as a function of  $\Delta E$  for the materials analyzed. The linear fit gives

$$-\sigma_c^{\text{eq}} \approx 25.72(\Delta E^{\text{HX-WZ}}) - 4.56.$$
 (4)

The coefficients in the equation are based on the units of  $-\sigma_c^{\rm eq}$  and  $\Delta E^{\rm HX-WZ}$  in GPa and eV/2 pairs, respectively. The similarity in the numerical values of coefficients of Eqs. (4) and (3) is fortuitous. Note that the WZ-HX homogeneous transformation enthalpy barrier is significantly lower than that of WZ-RS, i.e., always less than 0.1 eV/2 pairs for all materials studied except SiC. However, for SiC, the barrier is only slightly higher, i.e., 0.13 eV/2 pairs.

### D. Uniaxial tension along the $[01\overline{1}0]$ direction

The HX structure also has a longer dimension in the [0110] direction compared to the WZ structure (longer by approximately 9%, see Fig. 1, middle column). This difference allows WZ to transform into HX via tension in the b ([0110]) direction. Note that the difference in b between the two structures is only about half of the difference in c. Accordingly, the mechanical enthalpy contribution  $A_{ac}\sigma_b\Delta b$  is roughly half of the case of c compression for the comparable stress magnitude. Only three (InN, ZnO, and CdSe) out of the five materials studied have a local minimum corresponding to the HX structure under tensile loading along the b direction. We choose to present the enthalpy surfaces for InN (those for ZnO and CdSe can be found online35) at the equilibrium tensile stress  $\sigma_b^{\rm eq}$  [Fig. 12(a)] with its 2D section plot [Fig. 12(b)]. The plot<sup>35</sup> between the enthalpy differences  $\Delta H^{\rm HX-WZ} = H^{\rm HX} - H^{\rm WZ}$  as functions of tensile stress  $\sigma_b$  are similar to the compressive stress case. The equilibrium tensile stress  $\sigma_b^{\text{eq}}$  (14.7, 10.8, and 5.8 GPa for InN, ZnO, and CdSe, respectively) is approximately twice the equilibrium compressive stress  $-\sigma_c^{\rm eq}$  for the c direction. EP-MD simula-

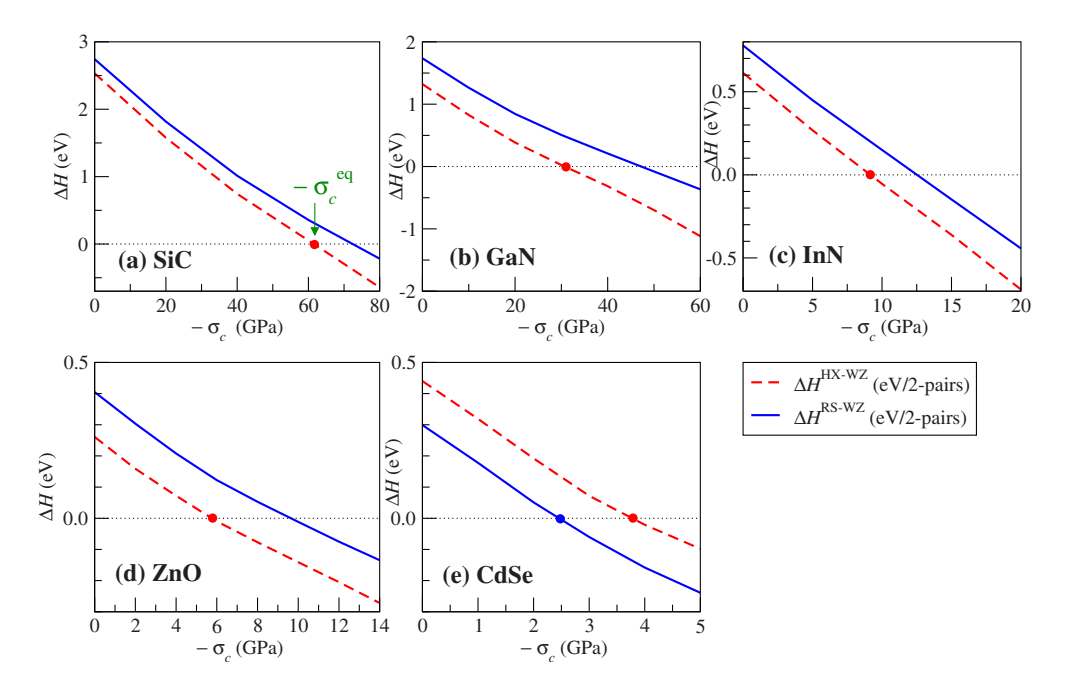


FIG. 10. (Color online) Enthalpy differences ( $\Delta H$ ) between the RS and WZ (solid line) and HX and WZ (dashed line) as a function of c-direction stress ( $-\sigma_c$ ) for (a) SiC, (b) GaN, (c) InN, (d) ZnO, and (e) CdSe. As the magnitude of the stress reaches the equilibrium value ( $-\sigma_c^{\rm eq}$ , indicated by solid dots), enthalpies of the HX and WZ structures become comparable. At stresses above  $-\sigma_c^{\rm eq}$ , the HX phase is more stable.

tions have shown that under tensile loading,  $[01\overline{1}0]$ -oriented ZnO nanowires can indeed transform into the HX structure under tensile loading.<sup>28</sup> The nanowires can sustain tensile stresses up to 14 GPa before failure, which is well above the equilibrium stress  $\sigma_b^{\rm eq}$  predicted here. The equilibrium transformation stress of  $\sigma_b^{\rm eq}$ =5.8 GPa for CdSe is the lowest among the materials studied. For nanostructures, other factors such as surface effects may contribute to facilitate the WZ $\rightarrow$ HX transformation.<sup>39</sup> As a result, HX can emerge as

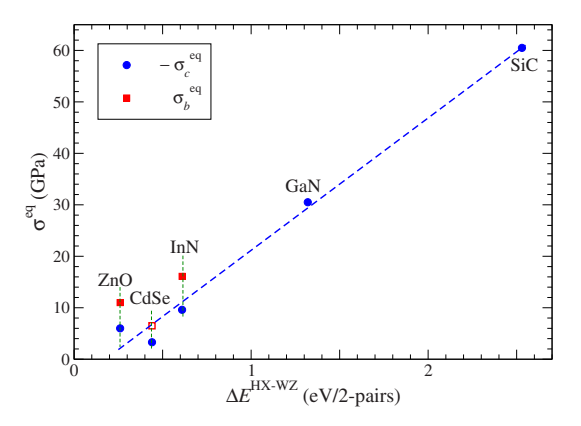


FIG. 11. (Color online) Correlation between equilibrium stresses  $(-\sigma_c^{\rm eq}$  and  $\sigma_b^{\rm eq})$  and the difference in energy  $(\Delta E)$  between the HX and WZ phases for the five materials.  $-\sigma_c^{\rm eq}$   $(\sigma_b^{\rm eq})$  is the equilibrium value of the c-direction compressive stress (b-direction tensile stress) for the HX and RS structures (see Table III). The energy difference  $\Delta E = E^{\rm HX} - E^{\rm WZ}$  is calculated under conditions of zero external loading and is tabulated in Table II.

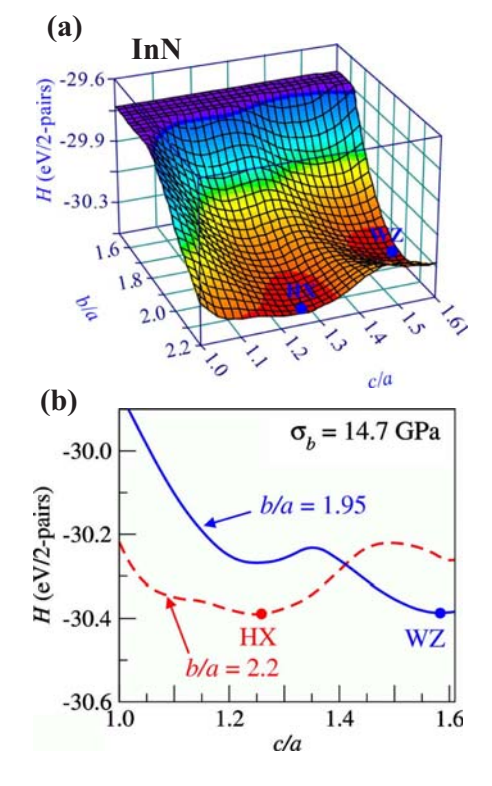


FIG. 12. (Color online) (a) Enthalpy surface maps (in eV/2 pairs) for InN at its HX-WZ stresses along the *b* direction,  $\sigma_b^{\rm eq}$ =14.7 GPa. (b) 2D sections of the enthalpy surface for b/a=1.95 (solid line) and 2.20 (dashed line).

an intermediate phase during a WZ $\rightarrow$ RS transformation in CdSe nanorods, <sup>39</sup> even though it does not have the lowest enthalpy in the bulk calculations. The relationship between  $\sigma_b^{\rm eq}$  and  $\Delta E^{\rm HX-WZ} = E^{\rm HX} - E^{\rm WZ}$  is shown Fig. 11. Note that the  $\sigma_b^{\rm eq}$  of CdSe may be higher than its fracture strength.

A local minimum for HX is not observed in the enthalpy surfaces for SiC and GaN, even at extremely high theoretical levels of  $\sigma_b$  (60 GPa for SiC and 30 GPa for GaN). The lack of transformation in these materials can be attributed to the fact that their equilibrium transformation stresses are higher than their respective ultimate tensile strengths ( $\sigma_b^{\rm eq} \gg \sigma_{\rm UTS}$ ). Indeed, EP-MD simulations have shown that for GaN nanowires,  $\sigma_{\rm UTS} \approx$  30 GPa, only a fraction of the rough estimation of equilibrium stress of  $\sigma_c^{\rm eq} \gg$  60 GPa. The  $\sigma_b^{\rm eq}$  of SiC is even higher since it has a higher energy difference between WZ and HX, making it more likely to have fractured before reaching its theoretical equilibrium stress of  $\sigma_c^{\rm eq} \gg$  120 GPa.

### V. CONCLUSIONS

First principles calculations are carried out to study the stability of the WZ, RS, and HX phases of SiC, GaN, InN, ZnO, and CdSe under loading of different triaxialities. The energy of the materials correlates with their ionicity. At ambient conditions, WZ has the lowest energy level, HX has the second highest energy level, and RS has the highest energy level (with the exception of CdSe whose RS phase has a lower energy level than its HX phase). All five materials have the fourfold wurtzite structure as their stable and naturally occurring phase. Under all around hydrostatic compression, the materials can transform into the sixfold coordinated RS structure. Under uniaxial compression along the [0001] direction and uniaxial tension along the [0110] direction, the materials can transform into the fivefold coordinated unbuckled wurtzite structure. The equilibrium conditions for the transformations are outlined. For the WZ→RS transformation, the equilibrium hydrostatic pressures  $(p^{eq})$  are predicted

to be 64.9, 44.1, 12.2, 8.2, and 2.2 GPa for SiC, GaN, InN, ZnO, and CdSe, respectively. These values are in good agreement with other theoretical calculations and experimental measurements. For the WZ-HX transformation under uniaxial compression along the [0001] direction, the equilibrium stresses  $(-\sigma_c^{eq})$  are 60.5, 30.5, 9.6, and 6.0 GPa for SiC, GaN, InN, and ZnO, respectively. For CdSe, uniaxial compression along the [0001] direction induces a WZ→RS transformation at a stress of 2.4 GPa instead of the WZ -> HX transformation because the formation energy of RS is lower than HX for CdSe. For the WZ -> HX transformation under uniaxial tension along the  $[01\overline{1}0]$  direction, the equilibrium transformation stresses ( $\sigma_b^{\rm eq}$ ) are 14.7, 10.8, and 5.8 GPa for InN, ZnO, and CdSe, respectively. The stress level for CdSe is close to its fracture limit. No transformation is observed for SiC and GaN under tension along the  $[01\overline{10}]$ direction due to the fact that their theoretical equilibrium transformation stresses are well above their respective ultimate fracture strengths. The magnitudes of  $p^{eq}$ ,  $-\sigma_c^{eq}$ , and  $\sigma_b^{eq}$ are approximately linearly dependent with the formation energy differences between the relevant phase of the materials. Based on the calculations of five materials, we established a general linear function between  $p^{eq}$  and RS-WZ energy difference that could be useful for predicting the difference in formation energy of the RS and WZ phases of other materials when the equilibrium pressure is known or vice versa.

### **ACKNOWLEDGMENTS**

This work was supported by NANOTEC (NN49-024) and Thailand Research Fund (BRG4880015 and PHD/0264/2545). A.J.K. and M.Z. are supported by NSF (CMS9984298) and NSFC (10528205). Computations are carried out at the National Synchrotron Research Center (Thailand) and at NAVO and ASC MSRCs through AFOSR MURI (D49620-02-1-0382).

### APPENDIX

Tables IV-VIII.

TABLE IV. Lattice parameters for WZ, HX, and RS SiC under equilibrium loading conditions.

Parameters	WZ $p=0$ GPa	$HX - \sigma_c^{\text{eq}} = 60.5 \text{ GPa}$	RS $p^{\text{eq}} = 64.9 \text{ GPa}$
a (Å)	3.05 (3.06, a 3.08b)	3.32	4.00 (3.68, <sup>a,c</sup> 3.84 <sup>d</sup> )
b (Å)	5.28	5.74	4.00
(Å)	4.97	3.98	4.00
$V = \frac{abc}{2}  (\text{Å}^3)$	40.0	38.0	32.0
$c/a^2$	1.63	1.20	1.00
o/a	1.73	1.73	1.00
ı	0.38	0.50	0.50
υ	0.35	0.33	0.50

<sup>&</sup>lt;sup>a</sup>DFT (LDA) calculations by Karch et al. (Ref. 17).

<sup>&</sup>lt;sup>b</sup>XRD experiment by Schultz et al. (Ref. 47).

<sup>&</sup>lt;sup>c</sup>Synchrotron ADX by Yoshida et al. (Ref. 10).

<sup>&</sup>lt;sup>d</sup>DFT (LDA) calculations by Hatch et al. (Ref. 48).

TABLE V. Lattice parameters for WZ, HX, and RS GaN under equilibrium loading conditions.

Parameters	WZ $p=0$ GPa	HX $-\sigma_c^{\text{eq}} = 30.5 \text{ GPa}$	RS $p^{\text{eq}} = 44.1 \text{ GPa}$
a (Å)	3.15 (3.19, <sup>a</sup> 3.16, <sup>b,c</sup> 3.10 <sup>d</sup> )	3.43	4.16 (4.01, <sup>a</sup> 4.10, <sup>b</sup> 4.07 <sup>e</sup> )
b (Å)	5.46	5.94	4.16
c (Å)	5.11	4.12	4.16
$V = \frac{abc}{2}  (\mathring{A}^3)$	44.0	42.0	36.0
$c/a^2$	1.62	1.20	1.00
b/a	1.73	1.73	1.00
и	0.38	0.50	0.50
v	0.35	0.33	0.50

<sup>&</sup>lt;sup>a</sup>Synchrotron EDX experiment by Xia et al. (Ref. 8).

TABLE VI. Lattice parameters for WZ, HX, and RS InN under equilibrium loading conditions.

	WZ	Н	RS	
Parameters	p=0 GPa	$-\sigma_c^{\text{eq}}$ =9.6 GPa	$\sigma_b^{\rm eq}$ =14.7 GPa	$p^{\text{eq}} = 12.2 \text{ GPa}$
a (Å)	3.54 (3.53, <sup>a</sup> 3.54, <sup>b,c</sup> 3.52 <sup>d</sup> )	3.82	3.48	4.64 (4.67, <sup>e</sup> 4.62 <sup>d</sup> )
b (Å)	6.13	6.62	7.66	4.64
c (Å)	5.70	4.59	4.35	4.64
$V = \frac{abc}{2}  (\mathring{A}^3)$	61.9	58.1	58.0	50.0
$c/a^{-2}$	1.61	1.20	1.25	1.00
b/a	1.73	1.73	2.20	1.00
и	0.38	0.50	0.51	0.50
v	0.35	0.33	0.31	0.50

<sup>&</sup>lt;sup>a</sup>DFT (LDA) calculations by Kim et al. (Ref. 50).

TABLE VII. Lattice parameters for WZ, HX, and RS ZnO under equilibrium loading conditions.

	WZ	Н	RS	
Parameters	p=0 GPa	$-\sigma_c^{\text{eq}}$ =6.0 GPa	$\sigma_b^{\rm eq}$ =10.8 GPa	$p^{\text{eq}} = 8.2 \text{ GPa}$
a (Å)	3.21 (3.20, <sup>a</sup> 3.25, <sup>b,c</sup> 3.26 <sup>d</sup> )	3.49	3.24	4.24 (4.28, <sup>b</sup> 4.27 <sup>c,e</sup> )
b (Å)	5.54	6.03	6.46	4.24
c (Å)	5.15 (5.17, <sup>a</sup> 5.22 <sup>d</sup> )	4.19	4.20	4.24
$V = \frac{abc}{2}  (\text{Å}^3)$	45.7 (46.69, <sup>e</sup> 47.24, <sup>f</sup> 47.98 <sup>d</sup> )	44.1	44.0	38.1 (39.03, <sup>e</sup> 38.16 <sup>f</sup> )
$c/a^{-2}$	1.61 (1.59 <sup>f</sup> )	1.20	1.30	1.00
b/a	1.73	1.73	2.00	1.00
и	0.38 (0.38 <sup>a,d,f</sup> )	0.50	0.50	0.50
v	0.33	0.33	0.31	0.50

<sup>&</sup>lt;sup>a</sup>DFT (LDA) calculations by Malashevich and Vanderbilt (Ref. 56).

<sup>&</sup>lt;sup>b</sup>XRD experiment by Xie et al. (Ref. 49).

<sup>&</sup>lt;sup>c</sup>DFT (LDA) calculations by Kim et al. (Ref. 50).

<sup>&</sup>lt;sup>d</sup>DFT (LDA) calculations by Yeh et al. (Ref. 51).

eXRD experiment by Lada et al. (Ref. 52).

<sup>&</sup>lt;sup>b</sup>DFT (LDA) calculations by Yeh et al. (Ref. 51).

<sup>&</sup>lt;sup>c</sup>XRD experiments by Osamura et al. (Ref. 53).

<sup>&</sup>lt;sup>d</sup>DFT (LDA) calculations by Furthmüller *et al.* (Ref. 54).

eADX experiment by Ueno et al. (Ref. 6).

<sup>&</sup>lt;sup>b</sup>Synchrotron EDX experiments by Desgrenier (Ref. 5).

<sup>&</sup>lt;sup>c</sup>XRD experiments by Karzel et al. (Ref. 55).

<sup>&</sup>lt;sup>d</sup>EXAFS experiments by Decremps et al. (Ref. 57).

<sup>&</sup>lt;sup>e</sup>DFT (GGA) calculations by Jaffe et al. (Ref. 16).

<sup>&</sup>lt;sup>f</sup>DFT (GGA) calculations by Ahuja et al. (Ref. 45).

	WZ	НХ	HX		
Parameters	p=0 GPa	$-\sigma_c^{\text{eq}}$ =3.75 GPa	$\sigma_b^{\rm eq}$ =5.8 GPa	RS $p^{\text{eq}} = 2.2 \text{ GPa}$	
a (Å)	4.27 (4.30 <sup>a</sup> )	4.66	4.18	5.54 (5.58, <sup>a</sup> 5.71 <sup>b</sup> )	
b (Å)	7.39	8.06	8.78	5.54	
c (Å)	6.96	5.59	5.44	5.54	
$V = \frac{abc}{2}  (\text{Å}^3)$	109.8	105.0	99.9	85.0	
c/a	1.63	1.20	1.30	1.00	
b/a	1.73	1.73	2.10	1.00	
и	0.38	0.50	0.50	0.50	
v	0.35	0.33	0.31	0.50	

TABLE VIII. Lattice parameters for WZ, HX, and RS CdSe under equilibrium loading conditions.

- <sup>1</sup>C. T. Chan, D. Vanderbilt, S. G. Louie, and J. R. Chelikowsky, Phys. Rev. B **33**, 7941 (1986).
- <sup>2</sup>S. Fahy, S. G. Louie, and M. L. Cohen, Phys. Rev. B **34**, 1191 (1986).
- <sup>3</sup> A. Mujica, A. Rubio, A. Muñoz, and R. J. Needs, Rev. Mod. Phys. **75**, 863 (2003).
- <sup>4</sup>C. F. Cline and D. R. Stephens, J. Appl. Phys. **36**, 2869 (1965).
- <sup>5</sup>S. Desgreniers, Phys. Rev. B **58**, 14102 (1998).
- <sup>6</sup>M. Ueno, M. Yoshida, A. Onodera, O. Shimomura, and K. Takemura, Phys. Rev. B 49, 14 (1994).
- <sup>7</sup>X. Wu, Z. Wu, L. Guo, C. Liu, J. Liu, X. Li, and H. Xu, Solid State Commun. **135**, 780 (2005).
- <sup>8</sup> H. Xia, Q. Xia, and A. L. Ruoff, Phys. Rev. B **47**, 12925 (1993).

  <sup>9</sup> O. Xia, H. Xia, and A. L. Ruoff, Mod. Phys. Lett. B **8**, 345.
- <sup>9</sup>Q. Xia, H. Xia, and A. L. Ruoff, Mod. Phys. Lett. B **8**, 345 (1994).
- <sup>10</sup>M. Yoshida, A. Onodera, M. Ueno, K. Takemura, and O. Shimomura, Phys. Rev. B **48**, 10587 (1993).
- <sup>11</sup>C. H. Bates, W. B. White, and R. Roy, Science **137**, 993 (1962).
- <sup>12</sup> J. Z. Jiang, J. S. Olsen, L. Gerward, D. Frost, D. Rubie, and J. Peyronneau, Europhys. Lett. **50**, 48 (2000).
- <sup>13</sup> K. Kusaba, Y. Syono, and T. Kikegawa, Proc. Jpn. Acad., Ser. B: Phys. Biol. Sci. 75, 1 (1999).
- <sup>14</sup>N. E. Christensen and I. Gorczyca, Phys. Rev. B **50**, 4397 (1994).
- <sup>15</sup>J. E. Jaffe and A. C. Hess, Phys. Rev. B **48**, 7903 (1993).
- <sup>16</sup>J. E. Jaffe, J. A. Snyder, Z. Lin, and A. C. Hess, Phys. Rev. B 62, 1660 (2000).
- <sup>17</sup>K. Karch, F. Bechstedt, P. Pavone, and D. Strauch, Phys. Rev. B 53, 13400 (1996).
- <sup>18</sup>S. Limpijumnong and S. Jungthawan, Phys. Rev. B **70**, 054104 (2004).
- <sup>19</sup>S. Limpijumnong and W. R. L. Lambrecht, Phys. Rev. B 63, 104103 (2001).
- <sup>20</sup>S. Limpijumnong and W. R. L. Lambrecht, Phys. Rev. Lett. **86**, 91 (2001).
- <sup>21</sup> J. Serrano, A. H. Romero, F. J. Manjon, R. Lauck, M. Cardona, and A. Rubio, Phys. Rev. B **69**, 094306 (2004).
- <sup>22</sup> A. Zaoui and W. Sekkal, Phys. Rev. B **66**, 174106 (2002).

- <sup>23</sup> M. Côté, O. Zakharov, A. Rubio, and M. L. Cohen, Phys. Rev. B 55, 13025 (1997).
- <sup>24</sup>F. Decremps, J. Pellicer-Porres, F. Datchi, J. P. Itie, A. Polian, F. Baudelet, and J. Z. Jiang, Appl. Phys. Lett. 81, 4820 (2002).
- <sup>25</sup> S. Y. Bae, H. W. Seo, J. Park, H. Yang, J. C. Park, and S. Y. Lee, Appl. Phys. Lett. **81**, 126 (2002).
- <sup>26</sup>Z. W. Pan, Z. R. Dai, and Z. L. Wang, Science **291**, 1947 (2001).
- <sup>27</sup> A. J. Kulkarni, K. Sarasamak, S. Limpijumnong, and M. Zhou, Philos. Mag. 87, 2117 (2007).
- <sup>28</sup> A. J. Kulkarni, M. Zhou, K. Sarasamak, and S. Limpijumnong, Phys. Rev. Lett. **97**, 105502 (2006).
- <sup>29</sup>L. Zhang and H. Huang, Appl. Phys. Lett. **89**, 183111 (2006).
- <sup>30</sup>L. Zhang and H. Huang, Appl. Phys. Lett. **90**, 023115 (2007).
- <sup>31</sup>D. Vanderbilt, Phys. Rev. B **41**, 7892 (1990).
- <sup>32</sup>G. Kresse and J. Furthmüller, Comput. Mater. Sci. 6, 15 (1996).
- <sup>33</sup>Here, we are interested only in the energy differences between phases. The calculations show that GGA *consistently give slightly larger energy differences* of between 0.1 and 0.4 eV/2 pairs (the largest case is for SiC which the energy difference by itself is large, i.e., 3 eV).
- <sup>34</sup>H. J. Monkhorst and J. D. Pack, Phys. Rev. B 13, 5188 (1976).
- <sup>35</sup> See EPAPS Document No. E-PRBMDO-77-026802 for additional enthalpy surface maps. For more information on EPAPS, see http://www.aip.org/pubservs/epaps.html.
- <sup>36</sup>For some low pressure or low stress loading conditions, the enthalpy surface (or energy surface for the stress-free case) might not have a local minimum near the HX structure. In such cases, the c/a and b/a defining the enthalpy of the HX phase is taken from the first (meta)stable HX when the pressure and/or stress is increased.
- <sup>37</sup>J. C. Phillips, Rev. Mod. Phys. **42**, 317 (1970).
- <sup>38</sup>M. S. Miao and W. R. L. Lambrecht, Phys. Rev. B 68, 092103 (2003).
- <sup>39</sup> M. Grunwald, E. Rabani, and C. Dellago, Phys. Rev. Lett. **96**, 255701 (2006).
- <sup>40</sup> Z. Wang, X. Zu, L. Yang, F. Gao, and W. J. Weber, Phys. Rev. B 76, 045310 (2007).

<sup>&</sup>lt;sup>a</sup>DFT calculations by Benkhettou et al. (Ref. 58).

<sup>&</sup>lt;sup>b</sup>XRD experiment by Wickham *et al.* (Ref. 59).

- <sup>41</sup> M. S. Miao and W. R. L. Lambrecht, Phys. Rev. B **68**, 092103 (2003).
- <sup>42</sup>K. J. Chang and M. L. Cohen, Phys. Rev. B **35**, 8196 (1987).
- <sup>43</sup> M. Catti, Phys. Rev. Lett. **87**, 035504 (2001).
- <sup>44</sup>J. Serrano, A. Rubio, E. Hernandez, A. Munoz, and A. Mujica, Phys. Rev. B **62**, 16612 (2000).
- <sup>45</sup>R. Ahuja, L. Fast, O. Eriksson, J. M. Wills, and B. Johansson, J. Appl. Phys. **83**, 8065 (1998).
- <sup>46</sup>J. M. Recio, M. A. Blanco, V. Luana, R. Pandey, L. Gerward, and J. S. Olsen, Phys. Rev. B **58**, 8949 (1998).
- <sup>47</sup>H. Schulz and K. H. Thiemann, Solid State Commun. **32**, 783 (1979).
- <sup>48</sup>D. Hatch, H. T. Stokes, J. Dong, J. Gunter, H. Wang, and J. Lewis, Phys. Rev. B **71**, 184109 (2005).
- <sup>49</sup> Y. Xie, Y. Qian, S. Zhang, W. Wang, X. Liu, and Y. Zhang, Appl. Phys. Lett. **69**, 334 (1996).
- <sup>50</sup> K. Kim, W. R. L. Lambrecht, and B. Segall, Phys. Rev. B **53**, 16310 (1996).
- <sup>51</sup>C. Y. Yeh, Z. W. Lu, S. Froyen, and A. Zunger, Phys. Rev. B 46,

- 10086 (1992).
- <sup>52</sup>M. Lada, A. G. Cullis, P. J. Parbrook, and M. Hopkinson, Appl. Phys. Lett. **83**, 2808 (2003).
- <sup>53</sup> K. Osamura, S. Naka, and Y. Murakami, J. Appl. Phys. **46**, 3432 (1975).
- <sup>54</sup> J. Furthmuller, P. H. Hahn, F. Fuchs, and F. Bechstedt, Phys. Rev. B **72**, 205106 (2005).
- <sup>55</sup>H. Karzel, W. Potzel, M. Kofferlein, W. Schiessl, M. Steiner, U. Hiller, G. M. Kalvius, D. W. Mitchell, T. P. Das, P. Blaha, K. Schwarz, and M. P. Pasternak, Phys. Rev. B 53, 11425 (1996).
- <sup>56</sup>A. Malashevich and D. Vanderbilt, Phys. Rev. B **75**, 045106 (2007).
- <sup>57</sup>F. Decremps, F. Datchi, A. M. Saitta, A. Polian, S. Pascarelli, A. D. Cicco, J. P. Itie, and F. Baudlet, Phys. Rev. B 68, 104101 (2003).
- <sup>58</sup> N. Benkhettou, D. Rached, B. Soudini, and M. Driz, Phys. Status Solidi B **241**, 101 (2004).
- <sup>59</sup>J. N. Wickham, A. B. Herhold, and A. P. Alivisatos, Phys. Rev. Lett. **84**, 923 (2000).

# Molecular dynamics and density functional studies of a body-centered-tetragonal polymorph of ZnO

J. Wang, A. J. Kulkarni, K. Sarasamak, S. Limpijumnong, F. J. Ke, And M. Zhou<sup>2,\*</sup>

1 Department of Physics, Beihang University, Beijing 100083, China

2 School of Mechanical Engineering, Georgia Institute of Technology, Atlanta, Georgia 30332-0405, USA

3 School of Physics, Suranaree University of Technology, Nakhon Ratchasima 30000, Thailand
and National Synchrotron Research Center, Nakhon Ratchasima 30000, Thailand

4 Institute of Mechanics, Chinese Academy of Sciences, Beijing 100080, China
(Received 13 September 2007; published 13 November 2007)

We report a previously unknown body-centered-tetragonal structure for ZnO. This structure results from a phase transformation from wurtzite in [0001]-oriented nanorods during uniaxial tensile loading and is the most stable phase for ZnO when stress is above 7 GPa. The stress-induced phase transformation has important implications for the electronic, piezoelectric, mechanical, and thermal responses of ZnO. The discovery of this polymorph brings about a more complete understanding of the extent and nature of polymorphism in ZnO. A crystalline structure-load triaxiality map is developed to summarize the relationship between structure and loading.

DOI: 10.1103/PhysRevB.76.172103 PACS number(s): 61.50.Ks, 61.46.-w, 62.25.+g, 64.70.Nd

Natural selection of the lowest energy state determines the bonding state and atomic arrangement of a material under ambient conditions. Deviations from this natural state occur when external stimuli such as mechanical loading and temperature changes are provided, leading to failure through bond breaking or polymorphism due to atomic rearrangement. At the macroscopic scale, failure is dominant since atomic mobility is relatively low and defects are more prevalent. At the nanoscale, however, high surface-to-volume ratios and nearly defect-free structures lead to higher atomic motilities and more pronounced polymorphic transitions. Consequently, polymorphs previously unknown for bulk materials can be revealed. Recently, a fivefold coordinated hexagonal phase (referred to as HX) of ZnO was observed in [0110]-oriented ZnO nanowires under uniaxial tensile loading.<sup>1,2</sup> This discovery has subsequently been confirmed in [0001]-oriented ZnO nanoplates<sup>3</sup> and nanowires.<sup>4</sup> Here, we report yet another polymorph of ZnO with a bodycentered-tetragonal structure with four-atom rings (referred to as BCT-4, space group P42/mnm), which occurs under uniaxial tensile loading along the [0001] crystalline axis of the wurtzite structure. While similar structures have been reported for carbon<sup>5</sup> and lithium aluminum oxide, <sup>6,7</sup> this polymorph has been reported here for a binary system. The results here show that the extent of polymorphism in ZnO (and perhaps in other groups IV, III-V, and II-VI materials such as GaN and CdSe) is much more pronounced than previously known. With the discovery of these phases, a more complete picture has emerged for the polymorphism of ZnO under the influence of mechanical loading with all realistic triaxialities. The recent fabrication and applications of defect-free, single-crystalline nanowires, nanobelts, and nanorings of materials such as ZnO, GaN, and CdSe highlights the need for understanding the extent of polymorphism. Characterization of the thermomechanical and electrical responses of the relevant phases is crucial since the performance and functionalities of these slender quasi-onedimensional materials as components in ultrasensitive chemical and biological sensors, nanoresonators, field effect

transistors, and nanogenerators<sup>8–11</sup> are either significantly affected by or utilize the phase transitions. <sup>12–14</sup>

Our analyses include both molecular dynamics (MD) simulations and density functional theory (DFT) based first principles calculations. The MD simulations are performed to study the phase transformation and the associated mechanical response of ZnO nanorods with the [0001] growth direction under loading and subsequent unloading. The first principles calculations are carried out to determine the energetic favorability and the electronic band structures of the parent and transformed phases. The impact of this phase transformation on the thermal, mechanical, and electric responses of the nanorods is also evaluated.

The as-synthesized hexagonal ZnO nanorods have a wurtzite structure with a sixfold symmetry around the [0001] axis and six  $\{01\overline{1}0\}$  lateral crystalline surfaces, <sup>15,16</sup> as illustrated in Fig. 1(a). The lattice parameters (Ref. 16) are a = 3.25 Å, u = 0.38, and c = 5.21 Å as shown in Fig. 2(a). The

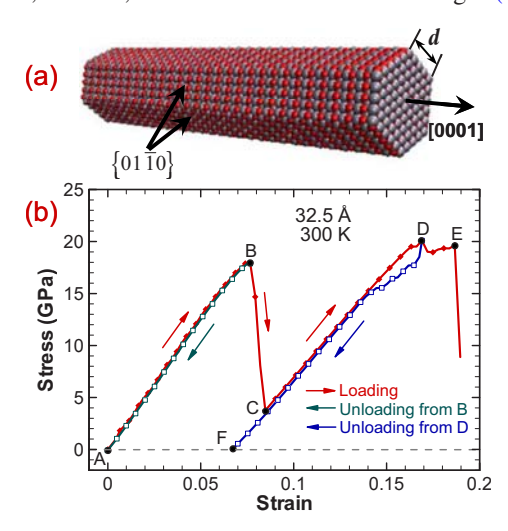


FIG. 1. (Color online) (a) [0001] nanorod with d=32.5 Å and (b) stress-strain curve of this nanorod at 300 K during loading and unloading.

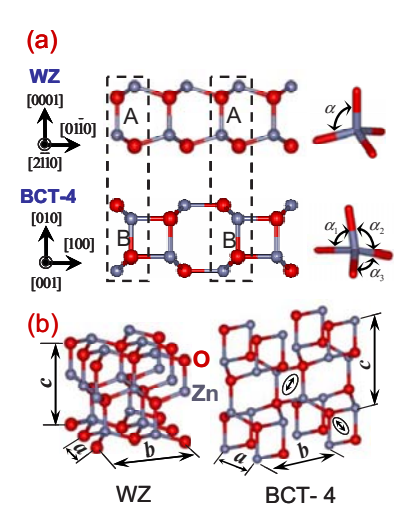


FIG. 2. (Color online) (a) Wurtzite (WZ) and body-centered-tetragonal with four-atom rings (BCT-4) structures and (b) crystal-lographic transition through breaking and formation of bonds and differences in bond angles between the WZ and the BCT-4 structures.

nanorods analyzed here have the same length of 145.8 Å and five different cross-sectional widths (d=19.5, 26.0, 32.5, 39.0, and 45.5 Å). A Buckingham-type potential with charge interactions is used to define atomic interactions in the MD calculations. <sup>13,17,18</sup> The analysis concerns quasistatic deformation at 300 K.<sup>1</sup>

Figure 1(b) shows the stress-strain response of a nanorod with lateral dimension d=32.5 Å. Four distinct stages are observed. The first stage  $(A \rightarrow B)$  corresponds to the elastic stretching of the wurtzite (WZ) structure up to a strain of 7.5%. Further deformation results in a precipitous stress drop (B→C) associated with the WZ to BCT-4 phase transformation. The transformation completes at a strain of 8.5%. Continued loading causes elastic stretching of the BCT-4 structure  $(C \rightarrow D)$  and culminates in the eventual failure at a strain of 16.9% (point E). To analyze the stability of the parent and transformed structures, unloading is performed from states prior to transformation initiation (first peak tensile stress, point B) and failure initiation of the nanorod (second peak tensile stress, point D). The unloading path from B coincides with the loading path, confirming that the deformation from A to B is indeed the elastic response of the WZ-structured nanorod. Unloading from D also results in the elastic recovery of the BCT-4 structure, and continued unloading beyond the transformation completion strain (point C) does not result in a reverse transformation. Instead, the nanorod retains the BCT-4 structure when the stress is reduced to zero [F in Fig. 1(b)].

The WZ to BCT-4 transformation occurs through a combination of (1) the breaking of every other Zn-O bond along the [0001] direction [bond A in Fig. 2(a)] and (2) the formation of an equal number of Zn-O bonds along the same direction [bond B in Fig. 2(a)] next to the broken bonds. This process repeats on alternate planes along the [0110] direction. The transformed structure retains the tetrahedral coordination with each Zn/O atom at the center and four O/Zn

TABLE I. Lattice constants for WZ and BCT-4 ZnO in tension along the  $\it c$  axis obtained via MD and DFT (in square brackets) calculations.

	WZ		ВС	T-4	
Parameters	$\sigma=0$	$\sigma=0$	σ=4	<i>σ</i> =7	σ=10
<i>a</i> (Å)	3.29	3.24	3.22	3.20	3.19
	[3.20]	[3.17]	[3.13]	[3.09]	[3.06]
b (Å)	5.67	5.58	5.54	5.51	5.48
	[5.55]	[5.48]	[5.42]	[5.35]	[5.32]
c (Å)	5.17	5.52	5.67	5.77	5.84
	[5.13]	[5.48]	[5.71]	[5.87]	[5.98]
V=abc (Å <sup>3</sup> )	96.4	99.8	101.2	101.7	102.1
	[91.1]	[95.2]	[96.9]	[97.0]	[97.3]
$\Delta V (Å^3)$	0.0	3.4	4.8	5.3	5.7
	[0.0]	[4.1]	[5.8]	[5.9]	[6.2]
c/a	1.57	1.71	1.76	1.80	1.83
	[1.60]	[1.73]	[1.82]	[1.9]	[1.95]
b/a	1.72	1.72	1.72	1.72	1.71
	[1.73]	[1.73]	[1.73]	[1.73]	[1.73]

atoms are at the vertices of a tetrahedron. The geometry of the tetrahedron can be characterized through the O-Zn-O bond angles  $(\alpha_i, i=1-6)$ , as shown in Fig. 2(a). For WZ, all bond angles are approximately equal  $(\alpha_i \approx 108^\circ)$ . For BCT-4, the formation of four-atom rings results in three distinct bond angles  $(\alpha_1 \approx 90^\circ, \alpha_2 \approx 112.7^\circ, \text{ and } \alpha_3 \approx 113.7^\circ)$ .

As seen from Fig. 2(b), the transformed phase consists of four-atom (two Zn and two O) rings arranged in a BCT lattice. Note that the four-atom ring at the center is rotated by 90° relative to the rings at the corners of the tetragonal lattice cell. Strictly speaking, the unit cell consists of two-ring clusters (one of each orientation, total of eight atoms) positioned in a simple tetragonal primitive lattice. Figure 2(b) also shows the lattice parameters a, b, and c for the WZ and BCT-4 structures. Their respective values as obtained from MD and DFT calculations (in square brackets) at various stress levels are listed in Table I along with unit cell volumes. For WZ, the ratios c/a and b/a are 1.60 and 1.73, respectively. Throughout the transformation, the b/a ratio remains at its initial value of 1.73 (±0.02), reflecting the symmetries of the loading and the lattice. On the other hand, upon transformation to BCT-4 at a stress above 7 GPa, the c/a ratio increases to 1.8. Phenomenologically, the predilection for the BCT-4 phase over the WZ phase under the tensile loading conditions considered here can be explicated by its elongated configuration in the [0001] direction (higher c/a ratio) relative to that of the WZ structure. Upon unloading, the residual strain at F in Fig. 1(b) is 6.8% according to both MD and DFT. It reflects the dimensional difference between the unstressed WZ and BCT-4 structures in the [0001] direction. This unstressed BCT-4 structure corresponds to the "ideal" BCT-4 structure predicted by the DFT calculations with b/a = c/a = 1.73 in Fig. 3(a).

The relative favorability of the two phases is studied by calculating the enthalpy (per four Zn-O pairs) using DFT calculations.<sup>2,19</sup> The complete enthalpy surfaces (not shown

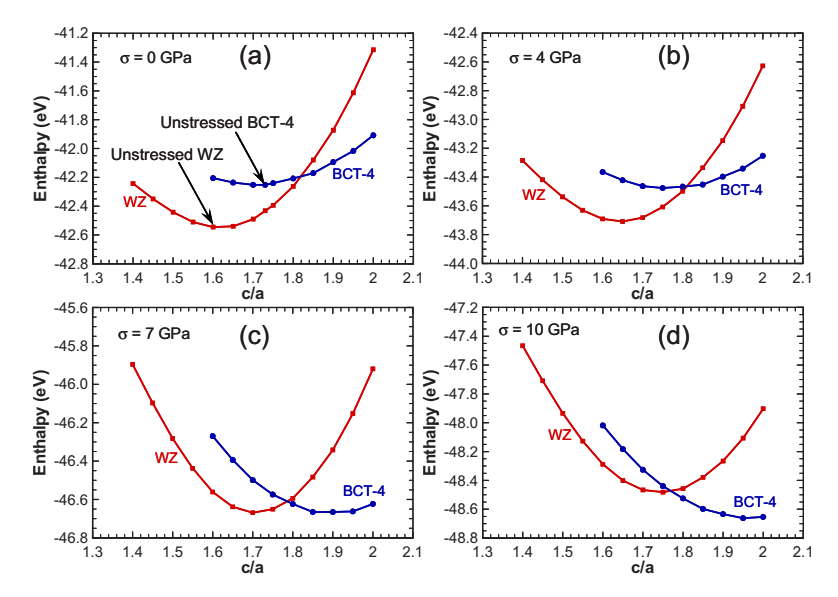


FIG. 3. (Color online) Enthalpy (per four Zn-O pairs) as a function of c/a obtained from DFT calculations for b/a=1.73 at tensile stresses of (a)  $\sigma=0$  GPa, (b)  $\sigma=4$  GPa, (c)  $\sigma=7$  GPa, and (d)  $\sigma=10$  GPa in the  $\lceil 0001 \rceil$  direction.

due to space limitation) show that the BCT-4 structure has minimum enthalpy at b/a=1.73 for all values of tensile stress considered. For clarity without loss of generality, the discussions here use Fig. 3 which shows the enthalpy values (eV per four Zn-O pairs) for both structures for b/a=1.73 at  $\sigma$ =0, 4, 7, and 10 GPa. At any stress level, each structure has its own enthalpy minimum. The first minimum is in the vicinity of  $c/a \approx 1.6$  which corresponds to WZ with lattice parameters slightly different from those at zero stress, and the second minimum is in the vicinity of  $c/a \approx 1.7-1.9$ , which corresponds to BCT-4. At zero stress, WZ is the stable crystal structure and its enthalpy is lower than that of BCT-4 by 0.3 eV [Fig. 3(a)]. As the stress is increased to 4 GPa [Fig. 3(b)], the difference in enthalpies decreases, and at a stress of 7 GPa [Fig. 3(c)], the two minima become comparable indicating that WZ and BCT-4 are equally favored. This value of stress corresponds to the equilibrium transition stress for the two phases. Since an energy barrier (associated with intermediate transitional states) exists for the transformation, a stress level higher than the 7 GPa equilibrium stress is required to initiate the transformation. At a stress of 10 GPa [Fig. 3(d)], the enthalpy of BCT-4 is lower, and this structure is clearly favored. Further increases in stress result in the eventual initiation of the phase transformation. The specific stress level at which the transformation initiates depends on the rod size and temperature. For the particular nanorod in Fig. 1 at 300 K, the critical stress level is  $\sigma$ =17.9 GPa. The gradual evolution of the local enthalpy minimum for the BCT-4 at  $\sigma$ =0 into a global minimum as stress increases confirms that the phase transformation observed in MD simulations is indeed energetically favored.

The phase transformation observed here alters the electrical, thermal, and mechanical responses of the nanorods. Recently, WZ-structured ZnO nanorods have been used to successfully generate direct electric current through mechanical bending. The transformation from the piezoelectric WZ structure to the nonpiezoelectric BCT-4 structure establishes an upper bound for the maximum possible current generation and operational strain for this application. Specifically, the electric field output  $E_3$  can be related to the longitudinal

strain  $\varepsilon_3$  through  $E_3 = \varepsilon_3/d_{33}$ , where  $d_{33} \approx 20.5$  pm/V is the piezoelectric coefficient for the ZnO nanorods. Since the strain at the initiation of transformation [B in Fig. 1(b)] is approximately 7.5% for all rod sizes, the maximum electric field output is therefore 3.7 V/nm. The mechanical response of BCT-4 also differs significantly from that of WZ. In particular, the enthalpy curves for BCT-4 are flatter than those for WZ (Fig. 3), indicating that the elastic stiffness of BCT-4 is lower than that for WZ. Indeed, in Fig. 1(b), the slope of curve AB (228 GPa, which is the [0001] elastic modulus of WZ) is higher than that of curve FD (167 GPa, which is the corresponding modulus of BCT-4). The thermal response of semiconductors such as ZnO is dominated by phonons and the interactions between phonons and surfaces.<sup>21</sup> The WZ to BCT-4 phase transformation changes the atomic arrangement and hence the phonon spectrum, resulting in potentially large changes in thermal conductivity. The electronic band structures of WZ and BCT-4 are shown in Fig. 4. Note that the total number of bands for BCT-4 is twice that for WZ because the unit cell of BCT-4 has twice as many atoms as WZ. Both phases have direct band gaps at  $\Gamma$ . Although DFT calculations with local density approximations are known to underestimate band gaps and therefore are not normally used to predict absolute band gap values, they can provide valid

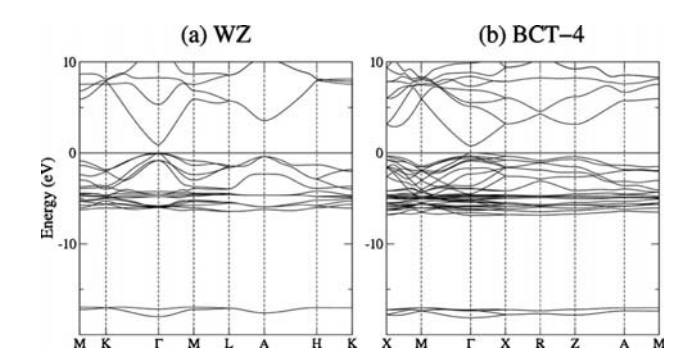


FIG. 4. Band structures of (a) WZ ZnO and (b) BCT-4 ZnO obtained by DFT calculations. The energy is relative to the top of the valence bands.

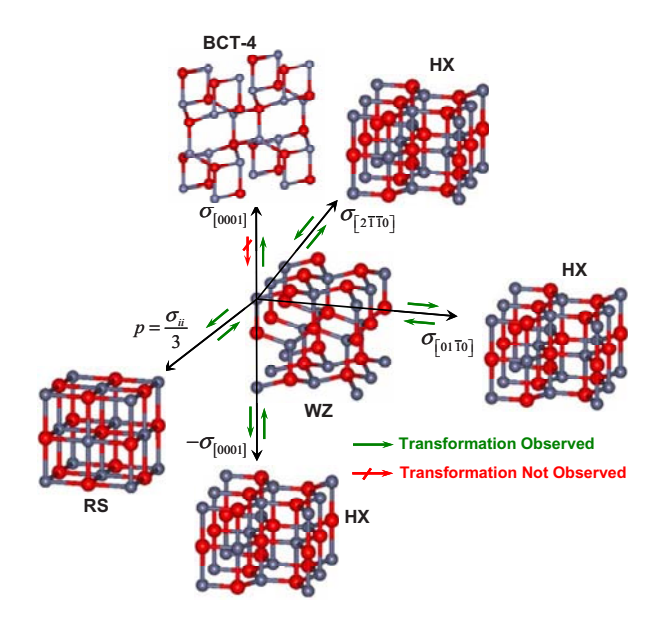


FIG. 5. (Color online) Crystalline structure-load triaxiality map summarizing the nature and much wider extent of polymorphism in ZnO than previously known; WZ is the natural state at ambient conditions, RS occurs under hydrostatic or near hydrostatic compression, HX occurs under tension along the [2110] and [0110] directions as well as compression along the [0001] direction, and BCT-4 occurs under tension along the [0001] direction. The green and red arrows indicate, respectively, possible and impossible transformation paths under relevant load direction reversals. ZB can only be grown epitaxially on certain crystalline planes of cubic crystals and cannot be obtained via a transformation from WZ under external loading; therefore, it is not included in this map.

relative comparisons between the two phases. The calculated band gap and average electron effective mass of BCT-4 are, respectively, 12% and 17% smaller than those of WZ, giving the nanorod a smaller band gap and potentially higher electron mobility after the WZ-to-BCT-4 transformation. These mechanically induced electrical property shifts may have applications in devices that depend on coupling between responses.

Most importantly, the identification of the BCT-4 structure leads to a more complete understanding of the nature and extent of polymorphism in ZnO and its dependence on load triaxiality. Joining wurtzite (WZ), zinc blende (ZB), rocksalt (RS), and HX, BCT-4 constitutes the fifth polymorph of ZnO discovered so far. It is now possible to construct a structureload triaxiality map for ZnO, as shown in Fig. 5. Among the previously well known phases, WZ is the most stable and naturally occurring phase and RS is observed under hydrostatic compressive conditions. Both BCT-4 and HX are stabilized under uniaxial loading, with HX occurring under tension along the  $[01\overline{1}0]$  and/or  $[2\overline{1}\overline{1}0]$  directions as well as compression along the [0001] direction and BCT-4 occurring under tension along the [0001] direction. It is worthwhile to note that ZB grows epitaxially on specific surfaces of cubic crystals and cannot be obtained via a transformation from WZ under external loading; therefore, it is not included in this map.

Support from NSF (CMS9984298), NSFC (10772012, 10432050, and 10528205), NANOTEC (NN49-024), and TRF (BRG4880015 and PHD/0264/2545) is acknowledged. Computations are carried out at the NAVO, ARL, ASC MSRCs, NSRC, and the LSEC of the CAS.

<sup>\*</sup>Author to whom correspondence should be addressed; FAX: 404-894-0186; min.zhou@gatech.edu

<sup>&</sup>lt;sup>1</sup> A. J. Kulkarni, K. Sarasamak, S. Limpijumnong, and M. Zhou, Philos. Mag. **87**, 2117 (2007).

<sup>&</sup>lt;sup>2</sup> A. J. Kulkarni, M. Zhou, K. Sarasamak, and S. Limpijumnong, Phys. Rev. Lett. 97, 105502 (2006).

<sup>&</sup>lt;sup>3</sup>L. Zhang and H. Huang, Appl. Phys. Lett. **89**, 183111 (2006).

<sup>&</sup>lt;sup>4</sup>L. Zhang and H. Huang, Appl. Phys. Lett. **90**, 023115 (2007).

<sup>&</sup>lt;sup>5</sup>P. A. Schultz and E. B. Stechel, Phys. Rev. B **57**, 3295 (1998).

<sup>&</sup>lt;sup>6</sup>M. Marezio, Acta Crystallogr. **19**, 396 (1965).

<sup>&</sup>lt;sup>7</sup>M. Marezio and J. P. Remeika, J. Chem. Phys. **44**, 3348 (1966).

<sup>&</sup>lt;sup>8</sup> M. S. Arnold, P. Avouris, Z. W. Pan, and Z. L. Wang, J. Phys. Chem. **107**, 659 (2003).

<sup>&</sup>lt;sup>9</sup> X. D. Bai, P. X. Gao, Z. L. Wang, and W. G. Wang, Appl. Phys. Lett. 82, 4806 (2003).

<sup>&</sup>lt;sup>10</sup>E. Comini, G. Faglia, G. Sberveglieri, Z. W. Pan, and Z. L. Wang, Appl. Phys. Lett. **81**, 1869 (2002).

<sup>&</sup>lt;sup>11</sup> Z. L. Wang and J. Song, Science **312**, 242 (2006).

<sup>&</sup>lt;sup>12</sup>J. Diao, K. Gall, and M. L. Dunn, Phys. Rev. B **70**, 075413 (2004).

<sup>&</sup>lt;sup>13</sup> A. J. Kulkarni, M. Zhou, and F. J. Ke, Nanotechnology **16**, 2749 (2005)

<sup>&</sup>lt;sup>14</sup>W. Liang and M. Zhou, Phys. Rev. B **73**, 115409 (2006).

<sup>&</sup>lt;sup>15</sup> A. Umar, B. Karunagaran, E. K. Suh, and Y. B. Hahn, Nanotechnology 17, 4072 (2006).

<sup>&</sup>lt;sup>16</sup> A. Wei, X. W. Sun, C. X. Xu, Z. L. Dong, Y. Yang, S. T. Tan, and W. Huang, Nanotechnology 17, 1740 (2006).

<sup>&</sup>lt;sup>17</sup>D. J. Binks and R. W. Grimes, J. Am. Ceram. Soc. **76**, 2370 (1993).

<sup>&</sup>lt;sup>18</sup> A. J. Kulkarni and M. Zhou, Acta Mech. Sin. **22**, 217 (2006).

<sup>&</sup>lt;sup>19</sup>S. Limpijumnong and S. Jungthawan, Phys. Rev. B **70**, 054104 (2004).

<sup>&</sup>lt;sup>20</sup>M. H. Zhao, Z. L. Wang, and S. X. Mao, Nano Lett. 4, 587 (2004).

<sup>&</sup>lt;sup>21</sup> A. J. Kulkarni and M. Zhou, Appl. Phys. Lett. **88**, 141921 (2006).

### First principles study of Mn impurities in PbTiO<sub>3</sub> and PbZrO<sub>3</sub>

### Adisak Boonchun

School of Physics, Suranaree University of Technology, Nakhon Ratchasima 30000, Thailand

#### M. F. Smith

National Synchrotron Research Center, Nakhon Ratchasima 30000, Thailand

### B. Cherdhirunkorn

Department of Physics, Thammasat University, Patum Thani 12121, Thailand

### Sukit Limpijumnonga)

School of Physics, Suranaree University of Technology, Nakhon Ratchasima 30000, Thailand and National Synchrotron Research Center, Nakhon Ratchasima 30000, Thailand

(Received 29 September 2006; accepted 30 December 2006; published online 27 February 2007)

A first principles study of an Mn impurity in PbTiO<sub>3</sub> and PbZrO<sub>3</sub> has been carried out to determine its favorable location and its electronic and magnetic properties. We find that it is energetically favorable for the Mn atom to substitute for Ti/Zr (as opposed to substituting for Pb and O or to residing in an interstitial position) under all equilibrium crystal growth conditions. The Mn defect mainly occurs as neutral-charge Mn substitute Ti/Zr, which has a total electron spin of 3/2. When no other impurities are present, a small concentration of charged Mn impurities that also form tends to make the sample slightly p type (n type) in oxygen-rich (poor) equilibrium growth conditions. © 2007 American Institute of Physics. [DOI: 10.1063/1.2654120]

### I. INTRODUCTION

The piezoelectric ceramics, including  $PbZr_{1-x}Ti_xO_3$  (henceforth PZT), have been applied in a wide variety of electrical devices, such as high-voltage high-power generators and sensors. <sup>1-3</sup> The advantages of PZT over other piezoelectric ceramics include a higher value for the piezoelectric coupling coefficient and easier modification of its response properties via chemical doping. When the amount of Ti and Zr is roughly equal, the PZT system undergoes a low-temperature rhombohedral-tetragonal crystal phase transition. <sup>4-6</sup> The strongest piezoelectric response and highest sensitivity to impurity doping effects are observed for doping levels that are close to this phase boundary. <sup>6-8</sup>

There is a rich literature that describes the modification of the piezoelectric response and other properties of PZT by various types of impurities (see, e.g., Refs. 9–12), and this remains an active area of research. Usually, donor-type impurities, when substituting for either Pb or Ti/Zr, tend to increase the piezoelectric coupling constant (as well as affecting other electric properties), whereas acceptor-type impurities tend to reduce this coupling constant. The former are referred to as soft dopants, and the latter as hard dopants in this context.

One dopant that has been the subject of interest is Mn.  $^{13,14}$  Although mainly used as a hard dopant, which substitutes for the Ti/Zr site and causes a reduction in the piezoelectric coupling strength close to rhombohedral-tetragonal phase boundary, recent studies have indicated that the role of Mn may be more complex.  $^{15}$  It was observed that a small concentration of Mn ( $\sim$ 0.5 at. %) actually can have a softening effect on PZT. As the concentration of this im-

purity is increased (>1 at. %), there is a recovery of the expected hardening effect, so that a further increase of Mn concentration results in a decrease of the piezoelectric coupling. This finding corresponds interestingly with an electron spin resonance (ESR) experiment on PbTiO<sub>3</sub>, which indicates that the fraction of Mn ions that act as acceptors (rather than neutral substitutes) decreases with increasing Mn concentration before reaching a minimum near 1 at. % and then rapidly increasing. <sup>16</sup>

This intriguing behavior of the piezoelectric response as a function of Mn impurity concentration, along with an interest in the magnetic state of the Mn impurity in the PZT environment, provides motivation for the present study. Although there may be many factors beyond the scope of this work that influence the electric response of the doped piezoelectric system, we can, as a starting point, try to understand the basic properties of the impurity introduced, such as its preferred site of occupation and charge state. For this purpose, we carry out first principles calculations of the electronic properties of PbTiO<sub>3</sub> and PbZrO<sub>3</sub> (henceforth PT and PZ, respectively) in the presence of a small number of Mn atoms. These simpler stoichiometric materials are considered because of the high computational cost of studying the PZT alloy. An application of our work to the PZT system is to be understood as an interpolation between the PT and PZ results.

The outline of this article is as follows. In Sec. II we present a detailed analysis of the allowable equilibrium growth conditions of PT and PZ (i.e., the range of allowed atomic chemical potentials), so that any dependence of the Mn defect position and charge state on growth conditions may be later determined. The discussion in that section may be useful in future studies of other types of impurities and defects in PZT. The details of our theoretical and computa-

a) Electronic mail: sukit@sut.ac.th

tional method are described in Sec. III. In Sec. IV we present our main results: the formation energy of possible Mn impurity types in PT and PZ as well as that of relevant native defects in these materials. We also discuss the midgap defect states associated with the Mn impurity. We conclude in Sec. V.

## II. DEFECT FORMATION ENERGIES AND CRYSTAL GROWTH CONDITIONS

If a certain type of defect has the formation energy  $E_f$ , then the concentration c of this defect, for a sample under thermal equilibrium, can be written as  $^{16,17}$ 

$$c(X^{q}) = N_{\text{sites}} \exp[-E_{f}(X^{q})/k_{B}T], \tag{1}$$

where  $N_{\rm sites}$  is the number of (symmetry-equivalent) possible defect sites per unit volume and  $c(X^q) \ll N_{\rm sites}$ . To calculate the defect formation energy  $E_f(X^q)$ , we use a so-called supercell approach. In the supercell approach, a single defect is included within a sufficiently large supercell (containing several unit cells of the bulk material), which is then repeated periodically through space. The defect formation energy  $E_f(X^q)$  of the defect labeled X with charge q is defined as the energy gained by the supercell when the defect is added to it and is given by  $^{18,19}$ 

$$E_f(X^q) = E_{\text{tot}}(X^q) - E_{\text{tot}}(0) - \sum_i \Delta n_i \mu_i + q \varepsilon_F, \tag{2}$$

where the first two terms on the right side are the result of a total energy calculation for the supercell with and without the defect, respectively. The sum in the third term is taken over all the species of atoms that must be added or removed from the supercell to form the defect,  $\Delta n_i$  is the number of atoms of element i that are added, and  $\mu_i$  is the corresponding atomic chemical potential. The final term in Eq. (1) depends on the charge of the defect and the Fermi energy  $\varepsilon_E$ .

The Fermi energy can be estimated by assuming that the sample is charge neutral, i.e., by assuming that the total charge of all impurities, valence band holes, and conduction band electrons is zero. Nevertheless, it is often useful to imagine that the Fermi energy can be freely varied within the band gap and that, as  $\varepsilon_F$  is raised through the energy levels associated with defects, electrons move from an external reservoir into the system to occupy these levels. In this picture, the stable charge state [i.e., the charge state q that gives the minimum defect energy  $E_f(X^q)$ ] changes as the Fermi level is varied such that the defect levels can be identified with kinks in a graph of the defect energy for the stable charge state versus  $\varepsilon_F$ . The levels that are determined in this way, known as thermodynamic transition levels, correspond to measurable quantities: they can be observed in an experiment for which the structure is allowed to relax after a transition, such as deep-level transient spectroscopy. One should keep in mind that these levels might not directly correspond to those measured in optical experiments, where the system does not have time to relax. Below, based on first principles calculations, we predict the positions of defect levels associated with various Mn defects in PT and PZ.

In using Eqs. (1) and (2) to determine the abundance of defects, one needs to know the chemical potentials, which

can vary greatly depending on growth and postgrowth treatment processes. However, the range of possible values of  $\mu_i$  can be roughly determined by considering the requirements for controllable growth of the crystal. <sup>20,21</sup>

In our case, equilibrium growth of the PbTiO<sub>3</sub> crystal requires that the following condition on the chemical potentials be satisfied:

$$\mu_{\text{Ti}} + \mu_{\text{Pb}} + 3\mu_{\text{O}} = \mu_{\text{PbTiO}_3}.$$
 (3)

Here, each atomic chemical potential is defined as the energy with respect to its elemental phase value, for example,  $\mu_{Ti}$  =0 corresponds to the chemical potential of the Ti atom in metallic titanium. With this choice of reference energies, we calculated  $\mu_{PbTiO_3}$ =-13.41 eV.

If the sum on the left-hand side of Eq. (3) was larger than the right-hand side, then rapid, uncontrolled growth of the PbTiO<sub>3</sub> crystal would occur. If the sum on the left-hand side was smaller than the right-hand side, then the crystal would disintegrate rather than grow. We also have to take into account additional constraints to ensure that the growth of other compounds, which contain some or all of the constituent elements of PbTiO<sub>3</sub>, is energetically less favorable than the growth of PbTiO<sub>3</sub> itself.

The requirement that the PbTiO<sub>3</sub> crystal growth is favorable over the formation of metallic Pb, Ti, or O<sub>2</sub> gas restricts the chemical potentials to the octant  $\mu_{Ti}$ ,  $\mu_{Pb}$ ,  $\mu_{O}$ <0. Along with Eq. (3), planes corresponding to equilibrium growth of PbO<sub>2</sub> and TiO<sub>2</sub>,

$$\mu_{\text{Pb}} + 2\mu_{\text{O}} = \mu_{\text{PbO}_2} \tag{4}$$

and

$$\mu_{\text{Ti}} + 2\mu_{\text{O}} = \mu_{\text{TiO}_2} \tag{5}$$

are relevant, respectively. Regions (of the three-dimensional chemical potential space) in which the right sides of Eqs. (4) and (5) exceed the left sides correspond to growth conditions for which PbO<sub>2</sub> and TiO<sub>2</sub> crystals disintegrate. For stable growth of PbTiO<sub>3</sub> to be ensured, a point ( $\mu_{Ti}$ ,  $\mu_{Pb}$ ,  $\mu_{O}$ ) must lie on the segment of the plane of Eq. (3) that is within the region in which both PbO<sub>2</sub> and TiO<sub>2</sub> are disintegrating. (Other competing phases, such as PbO and TiO, have been considered but found to give no further restriction on the allowed chemical potentials.)

In Fig. 1 we illustrate the determined conditions for stable PbTiO<sub>3</sub> growth with a shaded region on the  $\mu_{Ti}$ - $\mu_{Pb}$  plane. The values ( $\mu_{Ti}$ ,  $\mu_{Pb}$ ) that lie within this shaded region correspond to

$$C + \frac{1}{2}\mu_{\text{Ti}} < \mu_{\text{Pb}} < K + 2\mu_{\text{Ti}} \quad \text{and} \quad \mu_{\text{Pb}} < 0,$$
 (6)

where

$$C = \mu_{\text{PbTiO}_3} - \frac{3}{2}\mu_{\text{TiO}_2} = 1.96 \text{ eV},$$
 (6a)

$$K = 3\mu_{\text{PbO}_2} - 2\mu_{\text{PbTiO}_3} = 16.21 \text{ eV}.$$
 (6b)

For every point within the shaded region, there is a value of  $\mu_0$  given by Eq. (3) for which PbTiO<sub>3</sub> crystals grow in equi-

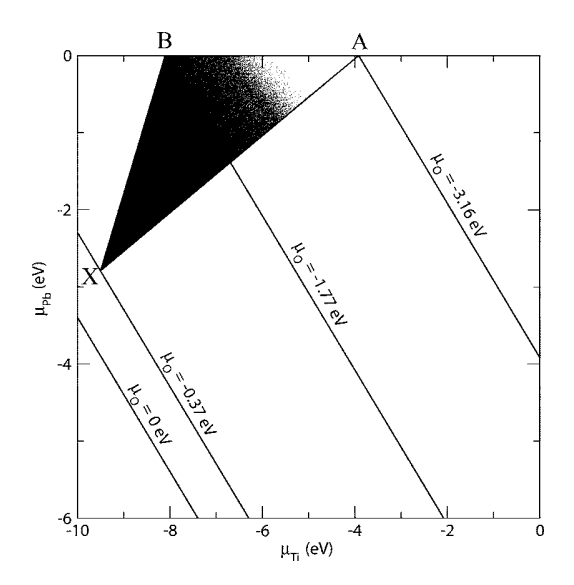


FIG. 1. An illustration of the allowed thermal equilibrium growth conditions for PbTiO<sub>3</sub>. The axes are the chemical potentials of Ti and Pb, each measured relative to its value in the natural elemental phase. For stable growth of PbTiO<sub>3</sub>, ( $\mu_{\rm Ti}, \mu_{\rm Pb}$ ) must lie in the shaded region. The chemical potentials of the constituent elements are related through Eq. (3) such that the allowed chemical potential of oxygen  $\mu_{\rm O}$  is uniquely determined once  $\mu_{\rm Ti}$  and  $\mu_{\rm Pb}$  are chosen (selected values of  $\mu_{\rm O}$  are shown). The significance of A, B, and X is discussed in the text.

librium without losing out to other phases. Selected values for  $\mu_0$  are given in the figure.

In the  $(\mu_{\text{Ti}}, \mu_{\text{Pb}}, \mu_{\text{O}})$  coordinate system, the point  $\mu_X \equiv (-9.50, -2.79, -0.37)$  eV, marked as X in Fig. 1, describes oxygen-rich growth conditions (this point has the highest possible  $\mu_{\text{O}}$ ). Note that this point also corresponds to both Ti-poor and Pb-poor conditions. Oxygen-poor (and Ti-rich) growth occurs at  $\mu_A \equiv (-3.92, 0, -3.16)$  eV, marked as A in the figure. There is no unique Pb-rich growth condition but rather a line of allowed points having  $\mu_{\text{Pb}} = 0$ . The point marked B in Fig. 1 is  $\mu_B \equiv (-8.11, 0, -1.77)$  eV, and its significance is explained below.

We are interested in determining whether an Mn impurity prefers to occupy the A site (the Pb site) or the B site (the Ti/Zr site) in PbTiO<sub>3</sub> and PbZrO<sub>3</sub>. This depends on the difference in the formation energies for a Mn atom occupying these two sites. In thermal equilibrium, the ratio of Mn atom occupancy at the A and B sites is simply given by

$$\frac{c(\mathrm{Mn_{Pb}})}{c(\mathrm{Mn_{Ti}})} = \exp\left[-\frac{E_f(\mathrm{Mn_{Pb}}) - E_f(\mathrm{Mn_{Ti}})}{k_B T}\right],\tag{7}$$

where  $Mn_{Pb}$  labels a defect for which Mn substitutes for Pb and

$$E_f(Mn_{Pb}) - E_f(Mn_{Ti}) = E_{tot}(Mn_{Pb}) - E_{tot}(Mn_{Ti}) + (\mu_{Pb} - \mu_{Ti}).$$
 (8)

Of the terms on the right side of Eq. (8), only  $(\mu_{Pb} - \mu_{Ti})$  depends on growth conditions.

From Eq. (8), it is clear that the growth conditions that provide the best chance for Mn to substitute Pb are those for which  $\mu_{\text{Pb}} - \mu_{\text{Ti}}$  is the least. Within the region of allowed growth,  $\mu_{\text{Pb}} - \mu_{\text{Ti}}$  has its minimum value at  $\mu_A$ . On the other hand,  $\mu_{\text{Pb}} - \mu_{\text{Ti}}$  has its maximum value at  $\mu_B$ , which corre-

sponds to growth conditions that provide the best chance for Mn to substitute Ti. To establish that  $Mn_{Ti}$  are more abundant than  $Mn_{Pb}$  in PT, it is sufficient to show that  $E_f(Mn_{Pb}) > E_f(Mn_{Ti})$  at  $\mu_A$ . If this is true, then Mn-for-Ti substitution is energetically more favorable (than Mn for Pb) for all possible equilibrium growth conditions.

Note that the ratio of equilibrium concentrations of Mn impurities in different lattice sites given in Eq. (7) is independent of  $\mu_{\rm Mn}$ . This means that, to identify whether Mn atoms prefer to occupy A or B site, the value of  $\mu_{\rm Mn}$  is not crucial. However, to roughly estimate the concentration of a given type of Mn impurity, we take  $\mu_{\rm Mn}$  to be equal to the maximum value allowed by the constraint associated with the formation of Mn metal or MnO<sub>2</sub> (whichever imposes the lower maximum). At the point  $\mu_A$  it is the Mn metal, for which  $\mu_{\rm Mn}$ =0, that imposes the stricter condition, whereas over most of the shaded region of Fig. 1 it is MnO<sub>2</sub> that is relevant.

We have carried out the analysis of growth conditions for PbZrO<sub>3</sub> and have found that it proceeds in much the same way as for PbTiO<sub>3</sub>. To avoid repetition, we give only the main results. The conditions needed for stable growth of PZ can be represented by a region in  $(\mu_{Zr}, \mu_{Pb}, \mu_{O})$  space that resembles the shaded area in Fig. 1, and the points X, A, and B for PT all have analog in the PZ case. Oxygen-rich growth corresponds to  $(\mu_{Zr}, \mu_{Pb}, \mu_{O}) = (-8.77, -0.89, -1.30)$  eV, whereas the growth condition most favorable for Mn-for-Pb substitution corresponds to  $(\mu_{Zr}, \mu_{Pb}, \mu_{O}) = (-6.95, 0, -2.25)$  eV and that favoring Mn-for-Zr substitution is  $(\mu_{Zr}, \mu_{Pb}, \mu_{O}) = (-8.38, 0, -1.77)$  eV.

### **III. COMPUTATIONAL METHOD**

We use spin-polarized density functional theory<sup>22</sup> (DFT) with local density approximation (LDA) and ultrasoft pseudopotentials, <sup>23</sup> as implemented in the VASP codes. <sup>24</sup> Spin-orbit couplings are not considered. The plane wave basis set used in the calculation contains plane waves up to a maximum energy of 450 eV. By obtaining the total energy dependence on the volume of the cubic unit cell, we determined the lattice constant for cubic PT and PZ to be a =3.89 and 4.12 Å, in good agreement with previous DFT calculations.<sup>25</sup> The corresponding experimental values of PT and PZ are 3.97 Å (Ref. 26) and 4.13 Å (Ref. 27), respectively. We determine the formation energy of defects by a supercell approach using a 40-atom supercell, which is a 2  $\times 2 \times 2$  repetition of the primitive unit cell, with all atoms in the supercell allowed to relax by minimization of the Hellmann-Feynman force to less than 0.05 eV/Å. To ensure convergence, selected calculations were repeated using a 3  $\times 3 \times 3$  (135-atom) supercell. By repeating calculations with the larger supercell, we have established that the interaction between Mn atoms in neighboring supercells are not important, i.e., that our results are a good approximation of the low concentration limit. For the Brillouin zone integrations, the  $2\times2\times2$  shifted Monkhorst-Pack<sup>28</sup> special k-points are used. The band gaps of PT and PZ at this special k-point are calculated to be 2.59 and 3.29 eV, respectively, which follow the usual LDA tendency of underestimating the band gap.

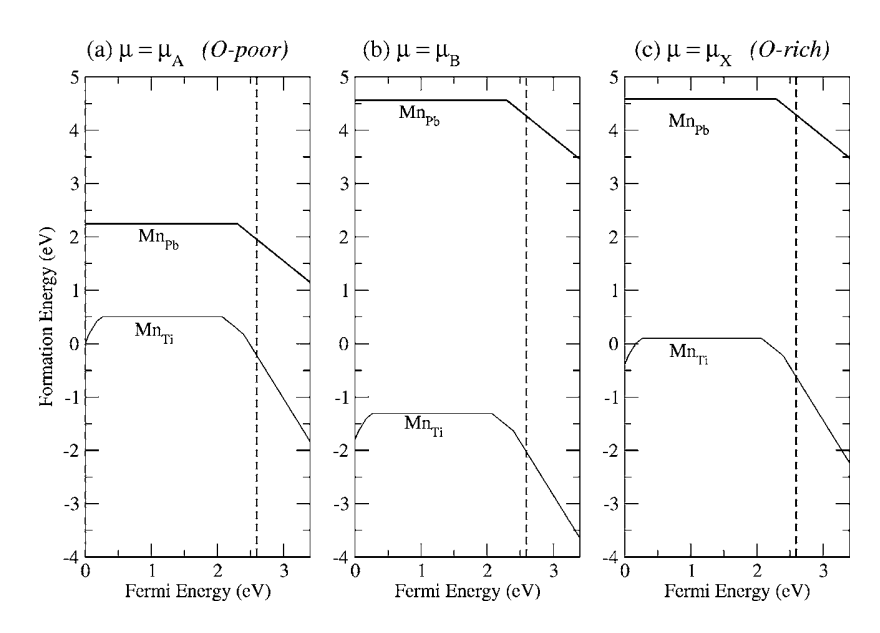


FIG. 2. The defect formation energy for the Mn impurity when substituting for lead (denoted Mn<sub>Pb</sub>) and for titanium  $(Mn_{Ti})$  in  $PbTiO_3$  is plotted vs the electron Fermi energy. The dashed vertical line indicates the calculated conduction band minimum, whereas the full range of the graph corresponds to the experimental band gap. Only the formation energy for the lowest energy charge state is shown. The slopes of the plots reflect the charge states of the defects and the kinks in the plots correspond to the energy positions at which transition from one charge state to another takes place, as discussed in the text. The panels are for different growth conditions.

The experimental band gaps of PT and PZ are 3.40 eV (Ref. 29) and 3.80 eV (Ref. 30), respectively.

For simplicity, we carried out our calculations in the high T cubic phase of PT and PZ. The piezoelectric tetragonal and rhombohedral phases occur at lower temperature. The local environment of the Mn impurity is expected to be similar in all three phases, since the ion shifts associated with the crystal phase changes are small. The cubic system should thus provide a good indication of the role of Mn doping in the low T phases as well.

### **IV. RESULTS**

In Fig. 2 the formation energies of  $Mn_{Pb}$  and  $Mn_{Ti}$  impurities, in the minimum energy charge states, are plotted as a function of the Fermi energy  $\varepsilon_F$ . The plots are for the three choices of growth conditions described above, that is, for  $\mu_A$ ,  $\mu_B$ , and  $\mu_X$  [Figs. 2(a)–2(c) respectively).

First, we note that the formation energy for Mn substituting Ti is always significantly lower than that for Mn substituting Pb. Even for  $\mu_A$ , at which Mn has its best opportunity to substitute Pb, the formation energy of Mn<sub>Pb</sub> is still larger than that of Mn<sub>Ti</sub> by more than 1.5 eV. According to Eq. (7), the equilibrium concentration of  $Mn_{Pb}$  is negligible compared to the concentration of Mn<sub>Ti</sub> defects at any reasonable temperature. (The formation energy of Mn<sub>O</sub>, not shown, is even larger than that of Mn<sub>Pb</sub>.) We can thus safely conclude that, among lattice sites, Mn atoms always prefer the Ti/Zr site in bulk PT and PZ systems. Note that under growth condition  $\mu_B$ , the formation energy of Mn<sub>Ti</sub> is always negative when the maximum possible value of the Mn chemical potential, set by the threshold of metallic Mn growth, is assumed ( $\mu_{Mn}$ =0). This means that, under condition  $\mu_R$ , the chemical potential of Mn must be lower (by at least  $\mu_{Mn} < -1.3$  eV, so that the formation energy of  $Mn_{Ti}$  is positive) than this maximum value in order to maintain stable growth of PT and keep the level of Mn incorporation low.

Next, we consider Mn interstitials. There are two interstitial sites in the perovskite lattice that are plausible candi-

dates for Mn occupation. One is located midway along the line between Pb neighbors, on the edge of the cubic unit cell, as shown in Fig. 3(a), and the other is located along the line between Pb and Ti sites, on the body diagonal, as shown in Fig. 3(b).

Based on our calculated formation energies, Mn interstitials prefer to reside between the Pb-Pb neighboring atoms, Mn<sub>int</sub>, [Fig. 3(a)], rather than between the Pb–Ti neighboring atoms, Mn'<sub>int</sub> [Fig. 3(b)]. (Strictly speaking, Mn'<sub>int</sub> does become slightly energetically favorable in extreme n-type conditions. However, in such conditions the formation energy for Mn<sub>Ti</sub> is much lower than that for either interstitial site thus in all cases the concentration of Mn'<sub>int</sub> is expected to be negligible compared to other Mn defects.) We do not consider Mn'<sub>int</sub> further. On the other hand, Mn<sub>int</sub> [Fig. 3(a)] can be important because of its high positive stable charge state and its low formation energy in p-type conditions. We show in Fig. 4(a) plot of the formation energy of this interstitial defect in comparison with that of Mn<sub>Ti</sub> for the same three choices of growth conditions as Fig. 2 (the formation energy of a titanium vacancy  $V_{Ti}$ , discussed below, is also shown).

The Ti-rich condition  $\mu_A$ , shown in Fig. 4(a), is the most favorable condition for Mn<sub>int</sub> to form. In this case, the for-

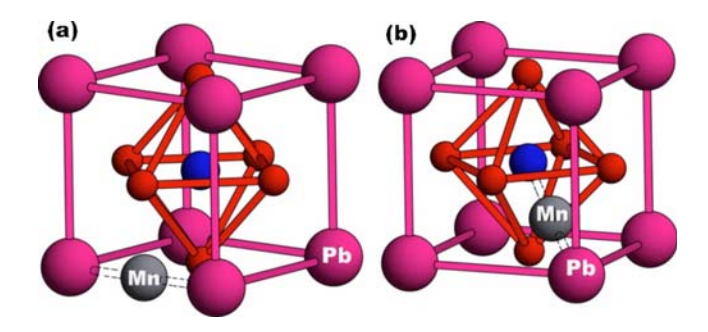


FIG. 3. (Color online) Schematic illustration of Mn interstitials in PbTiO<sub>3</sub>. Two types of Mn interstitials are shown: at the site between (a) the Pb–Pb neighboring atoms (Mn $_{\rm int}$ ) and (b) Pb–Ti neighboring atoms (Mn $_{\rm int}$ ). The large spheres at the corner of unit cell are Pb atoms, the medium-sized sphere at the cube center is a Ti atom, and the small spheres at the face centers are O atoms.

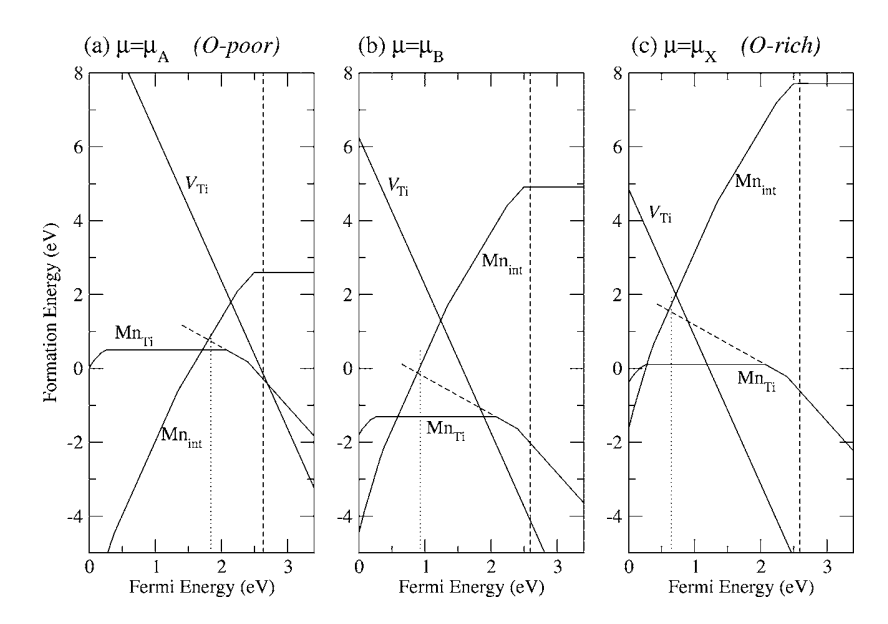


FIG. 4. The defect formation energies of Mn substituting for Ti (denoted Mn<sub>Ti</sub>), Mn interstitial (Mn<sub>int</sub>), and Ti vacancy (V<sub>Ti</sub>) in PbTiO<sub>3</sub> for three growth conditions. The pinned value of the Fermi energy is indicated by a vertical dotted line. This level is determined by assuming perfect charge compensation between the leading acceptor (in this case, Mn<sub>Ti</sub>) and the leading donor ( $Mn_{int}$ ). Since  $Mn_{Ti}$  in 1- charge state should act as the leading acceptor (when no other lowerenergy acceptors are present), its formation energy plot is extended with a dashed line to the intersection with that of the leading donor (Mn<sub>int</sub>).

mation energy of Mn<sub>int</sub> is negative for a wide range of values of the Fermi energy extending from extreme *p*-type to slightly *n*-type conditions. Over this range, the number of Mn interstitial defects would be expected to increase rapidly during growth, while the number of substitutional defects would remain negligible. However, Mn<sub>int</sub> has a high positive charge state whenever it is energetically favored over other forms. Since the system must remain charge neutral, the incorporation of Mn<sub>int</sub> requires a compensating addition of negative charge. This balance ensures that Mn<sub>Ti</sub> defects will always occur in higher concentration than the interstitials under thermal equilibrium growth conditions.

To see this, one may imagine introducing Mn to a Ti-rich PT sample that initially has its Fermi level just above the valence band maximum (VBM). Under this condition, the Mn<sub>int</sub>, which is a donor, would form rapidly (since the formation energy is negative for this Fermi energy). The electrons donated by the Mn interstitials would compensate preexisting intrinsic holes and hence the Fermi level would rise as the Mnint concentration increased. This would continue until some acceptor could form at a concentration comparable to that of  $Mn_{int}$ . In Fig. 4(a), it is clear that  $Mn_{Ti}$  will act as this compensating acceptor. Thus, if we start the Mn doping process with a sample that is p type, the Fermi level will increase until it reaches a value at which the formation energy of Mn<sub>Ti</sub><sup>1-</sup> and Mn<sub>int</sub><sup>3+</sup> are roughly equal. A balance is then achieved between donation by Mn<sup>3+</sup> and acceptance by  $Mn_{Ti}^{1-}$ , which stabilizes the Fermi level. From Eq. (1) we find that the precise value of this pinned Fermi level is  $\varepsilon_F$ ≈ 1.86 eV, indicated with a dotted line in Fig. 4. (Note that free carriers in the valence and conduction bands can be ignored at any reasonable temperature since the pinned Fermi level is deep inside the band gap.) At this Fermi level, the relative concentrations of the most abundant Mn forms are  $c(Mn_{Ti}^0) \approx 8 \times c(Mn_{Ti}^{1-}) \approx 24 \times c(Mn_{int}^{3+})$ , assuming the temperature of 900 °C. Without other lower-energy compensating acceptors, this relative concentration of interstitial defects is the highest value possible for thermal equilibrium growth under any chemical potential conditions. This is the basis of our conclusion that the vast majority of Mn defects are neutral  $Mn_{Ti}$  and that the concentration of  $Mn_{int}$  is always much lower.

We have also considered several fundamental native point defects in PT to determine whether any of them could compensate Mn impurities. Only the Ti vacancy, denoted  $V_{\rm Ti}$ , is found to have sufficiently low formation energy to merit consideration. The titanium vacancy occurs in the 4- charge state and has a reasonably low formation energy under  $\mu_B$  and  $\mu_X$  conditions. However, from Figs. 4(b) and 4(c), we can see that  $V_{\rm Ti}$  never acts as the leading compensating acceptor—it always loses out to an Mn acceptor. Also, since the formation energies of the leading donor (Mn<sub>int</sub>) and leading acceptor (charged Mn<sub>Ti</sub>) at the pinned Fermi level are significantly higher than the formation energy of Mn<sup>0</sup><sub>Ti</sub>, the number of Mn<sup>0</sup><sub>Int</sub> and charged Mn<sub>Ti</sub> is negligible compared to the number of Mn<sup>0</sup><sub>Ti</sub> for  $\mu_B$  and  $\mu_X$  growth conditions.

We summarize the preceding results of our total energy calculations before discussing the defect states inside the band gap. For all thermal equilibrium growth conditions of PT, the vast majority of Mn impurities will substitute for Ti and will have neutral charge state. This neutral Mn<sub>Ti</sub> defect carries a magnetic moment of three electronic spins, as explained below. (ESR measurements have consistently seen evidence of Mn-for-Ti substitutes in the 3/2 spin state in PbTiO<sub>3</sub>, in agreement with our results. Mixed valence states for the Mn-for-Ti substitutes have also been reported in ESR studies, though the presence of non-neutral substitutes appears to depend on experimental growth conditions and firing temperature. 16,31) In addition, our calculations indicate that under Ti-rich conditions, Mn-doped PT cannot be grown p type under thermal equilibrium because of the spontaneous formation of positively charged Mn<sub>int</sub>, which pushes the samples into the *n*-type region. On the other hand, for O-rich conditions, the Mn-doped PT samples could be predicted to be slightly p type because the pinned Fermi level is closer to the VBM than the middle of the band gap.

From the kinks in the graph of  $E_f(Mn_{Ti})$  vs  $\varepsilon_F$ , one can identify several thermodynamic transition levels close to the

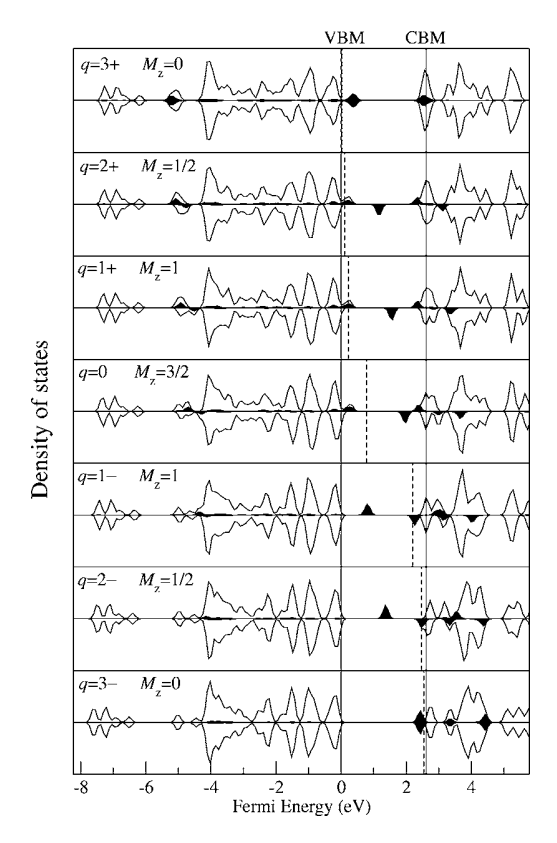


FIG. 5. Spin-polarized density of states for PbTiO $_3$  supercell with a Mn substitute Ti (Mn $_{\rm Ti}$ ). In each panel, the unfilled curve is the total DOS while the filled curve is the Mn local DOS (Ref. 32) and the upper (lower) curves are for spin up (down). All seven possible charge states (from 3+ to 3-) are shown in separate panels. The Fermi level for each charge state is shown as a dashed vertical line that moves from the valence band maximum to the conduction band minimum, each of which is indicated by a solid vertical line, as the charge is decreased. The DOSs inside the band gap are derived from Mn d orbitals.

band edges. If the Fermi level is varied through the band gap starting at the VBM, the stable charge state of Mn<sub>Ti</sub> changes from 3+ to 3- as these Mn levels are being filled one by one. Although the calculated Kohn-Sham (KS) single electron states do not coincide exactly with these transition levels (the difference comes from the structural relaxation energy when changing from one charge state to another), a rough correspondence can be made. It is thus interesting to follow the occupation of these single electron states, along with the magnetization of the supercell, as the defect charge state changes from 3+ to 3-. We describe this progression below and also illustrate it using the calculated density of states (DOS) and Mn local density of states, <sup>32</sup> (LDOS) in Fig. 5. There are a total of six levels, a degenerate triplet for each spin, that are localized near the Mn ion and located inside the band gap. These levels are derived from the  $d_{xy}$ ,  $d_{xz}$ , and  $d_{yz}$ atomic orbitals of Mn, which remain degenerate in the cubic crystal field experienced by the Mn atom at the octahedral Ti site (the doublet corresponding to the other two d orbitals having been split off into the conduction band by the perturbing crystal field). In bulk PT, a Ti atom donates four electrons to O atoms. Therefore, the removal of a neutral Ti atom leaves four holes in the valence band. Upon being inserted as a substitute, the  $3d_54s_2$  Mn atom sheds four electrons to fill these holes. Since none of the modified atomic orbitals of Mn lie below the VBM, the Mn atom donates its remaining three electrons to the reservoir—leaving the system in the 3+ charge state—when the Fermi level is close to the VBM. In all our calculations, we set initial atomic magnetic moments to point along the positive  $\hat{\mathbf{z}}$  direction (note that the spin-orbit coupling is not included, so the spin quantization axis  $\hat{\mathbf{z}}$  is arbitrary). Because of this choice of initial configurations, the fully relaxed configurations are such that the spin-up Mn levels are the first to be occupied when the Fermi energy is increased. The  $\hat{\mathbf{z}}$  component of the total spin of the supercell, denoted  $M_{z}$ , is zero in the 3+ charge state. As electrons are added into the spin-up states,  $M_z$  increases to a maximum of 3/2 when the charge state is neutral and all spin-up (spin-down) Mn levels are filled (empty) before decreasing back to zero as spin-down electrons are added and the charge state goes from neutral to 3-. In the 3+ charge state, the six empty levels are degenerate and lay roughly 0.5 eV above the VBM (see the top panel of Fig. 5). As the spin-up levels become occupied, one by one, the energy of the spin-up triplet drops slightly closer to the VBM due to the system seeking a minimum total energy of all occupied states. The level of the unoccupied spin-down triplet, on the other hand, increases significantly and progressively, owing to the Coulomb repulsion with the electrons present in spin-up states (note the large energy splitting between the spin-up and spin-down Mn states for the intermediate charge states in Fig. 5). Once the spin-up states are filled and the occupation of the spin-down states begins, the trend reverses until the energy levels of the six states are again equal in the 3- charge state, with a value slightly below the conduction band minimum (CBM) (the bottom panel of Fig. 5).

In Fig. 5, the LDOS peaks near the VBM correspond to the Mn ( $d_{xy}$ ,  $d_{xz}$ ,  $d_{yz}$ )-derived triplets. An additional peak in the LDOS occurs close to the conduction band minimum and dips slightly into the band gap for charges between 2+ and 0, as seen in the spin-up LDOS of Fig. 5. This additional peak corresponds to the empty doublet derived from the localized  $d_{x^2-y^2}$  and  $d_{3z^2-r^2}$  Mn orbitals. It does not give rise to thermodynamic levels since the corresponding single electron levels are pushed into the conduction bands once the spin-down ( $d_{xy}$ ,  $d_{yz}$ ,  $d_{yz}$ ) triplet begins to be filled.

The top of the valence band for PT is composed mainly of oxygen p orbitals, whereas the bottom of the conduction band is mainly composed of Ti d orbitals. We thus expect that the dipole-allowed optical transitions at the excitation energy below the bulk band gap will correspond to excitations from valence band to the empty midgap Mn states.

The case of PbZrO<sub>3</sub> is so similar that we merely list our results. The  $Mn_{Zr}$  defect is found to have the lowest formation energy (lower by about 4 eV than the  $Mn_{Pb}$  defect at  $\mu_A$ ). For  $Mn_{Zr}$ , the positions of the two thermodynamic transition levels are very similar to those for  $Mn_{Ti}$ , with the same sequence of stable charge states.

The location of the Mn impurity within the unit cell could be inferred from the extended x-ray absorption spectroscopy (EXAFS) measurement near the Mn absorption threshold. This measurement technique provides information about the distance and identity of neighbors of the Mn atom.

TABLE I. Calculated distances between neutral  $Mn_{Ti}$  (and  $Mn_{Zr}$ ) and its neighbors. The numbers in parentheses are the corresponding distances in bulk PT (and PZ) between the Ti atom (Zr atom) and its neighbors.

	Mn–O distance (Å)	Mn–Pb distance (Å)
Mn <sub>Ti</sub>	1.91 (1.87)	3.35 (3.33)
$Mn_{Zr}$	1.95 (1.84)	3.49 (3.41)

To make an accurate comparison with experimental data the actual position of neighboring atoms, which are displaced due to the insertion of Mn atoms, must be known. For this purpose we list in Table I the distances between the Mn atom and its nearest and next-nearest neighbors in PT and PZ obtained from our first principles calculations. It may be noted that, in all cases, the difference between the relaxed and bulk positions of the atoms is relatively small (all are less than 10%). However, this was not obvious beforehand and could only be assured by performing the structural relaxations as we have done.

As a final point of discussion, we recall that Mn impurities have been observed to have a softening effect on the piezoelectric response of PZT at low concentrations and a hardening effect at higher concentrations. Certainly it is difficult to make a connection between the piezoelectric response and our calculations since structural changes occurring on length scales much larger than a unit cell, which might take place when Mn is introduced, can also affect the former, whereas our results only consider local properties. Still, it may be worth noting that both donor-type and acceptor-type Mn impurities were found above to have a low formation energy under allowable growth conditions of PT and PZ. Thus, although equilibrium growth favors neutral substitutes, it is plausible that a sufficient number of charged Mn substitutes and interstitials might be present and playing a role in the observed hardening/softening effects, especially in nonequilibrium growth conditions. Since softening (hardening) is typically associated with donor (acceptor) impurities, the observation that Mn impurities can have both softening and hardening effects is consistent with our finding that both Mn donors and acceptors are low-energy defects, depending on growth conditions. If one was able to correlate Mn location (measured via EXAFS, for example) with the measured piezoelectric response, then further insight into this issue might result.

### V. CONCLUSIONS

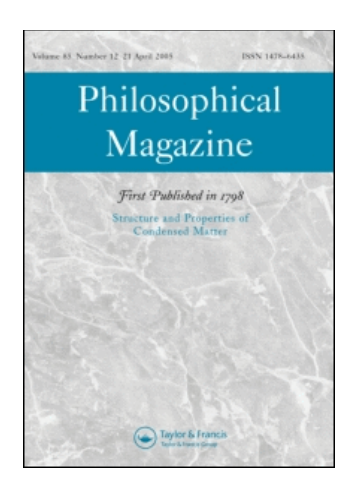
The Mn impurity prefers to occupy the Ti/Zr site  $(Mn_{Ti/Zr})$  over other sites in PbTiO<sub>3</sub> and PbZrO<sub>3</sub> under all equilibrium growth conditions. The majority of  $Mn_{Ti/Zr}$  defects occur in the neutral charge state, with a total electron spin of  $M_z$ =3/2. (Note that spin interactions between Mn atoms were not considered in this study so no claim is being made about dilute magnetism.) There is expected to be a small concentration of  $Mn_{Ti/Zr}$  in a 1– charge state with a total spin of  $M_z$ =1 and a similar amount of Mn interstitials in a 3+ charge state with  $M_z$ =2. These minority impurities could be important for determining the Fermi level since

their total charge, for Mn concentrations on the order of 1%, far exceeds the number of thermally excited free carriers. The Fermi level thus determined suggests that Mn-doped PZT should be slightly p type in O-rich conditions and slightly n type in O-poor conditions if the sample is not dominated by other low-energy impurities. The lattice relaxation in the vicinity of the Mn substitute is minor, with nearest-neighbor bond lengths changing by less than 10%.

### **ACKNOWLEDGMENTS**

We acknowledge S. Rujirawat and P. Songsiriritthigul for fruitful discussions. This work is supported by NANO-TEC (Thailand) under Contract No. NN49-024 and by the Thailand Research Fund under Grant No. BRG4880015.

- <sup>1</sup>S. B. Lang, Phys. Today **58**(8), 31 (2005).
- <sup>2</sup>L. E. Cross, Ferroelectric Ceramics: Tailoring Properties for Specific Application (Birkhauser, Basel, 1993).
- <sup>3</sup>J. F. Scott, *Ferroelectric Memories* (Springer, Berlin, 2000).
- <sup>4</sup>B. Jaffe, W. R. Cook, and H. Jaffe, *Piezoelectric Ceramics* (Academic, New York, 1971).
- <sup>5</sup>B. Noheda, J. A. Gonzalo, L. E. Cross, R. Guo, S.-E. Park, D. E. Cox, and G. Shirane, Phys. Rev. B **61**, 8687 (2000).
- <sup>6</sup>B. Noheda and D. E. Cox, Phase Transitions **79**, 5–20 (2006).
- <sup>7</sup>R. Guo, L. E. Cross, S.-E. Park, B. Noheda, D. E. Cox, and G. Shirane, Phys. Rev. Lett. **84**, 5423 (2000).
- <sup>8</sup>L. Bellaiche, A. Garcia, and D. Vanderbilt, Phys. Rev. Lett. 84, 5427 (2000).
- <sup>9</sup>E. Boucher, D. Guyomar, L. Lebrun, B. Guiffard, and G. Grange, J. Appl. Phys. **92**, 5437 (2002).
- <sup>10</sup>Z. Xu, X. Dai, and D. Viehland, Phys. Rev. B **51**, 6261 (1995).
- <sup>11</sup>J. Frantti, V. Lantto, S. Nishio, and M. Kakihana, Phys. Rev. B 59, 12 (1999)
- <sup>12</sup>I. Franke, K. Roleder, L. Mitoseriu, R. Pitescu, and Z. Ujma, Phys. Rev. B 73, 144114 (2006).
- <sup>13</sup>M. D. Glinchuk, T. P. Bykov, V. M. Kurliand, M. Boudys, T. Kala, and K. Nejezchleb, Phys. Status Solidi A **122**, 341 (1990).
- <sup>14</sup>L. X. Le and C. E. Li, J. Mater. Sci. **35**, 2477 (1990).
- <sup>15</sup>B. Cherdhirunkorn and D. A. Hall, Integr. Ferroelectr. **62**, 61 (2004).
- <sup>16</sup>K. Hayashi, A. Ando, Y. Hamaji, and Y. Sakabe, Jpn. J. Appl. Phys., Part 1 37, 5237 (1998).
- <sup>17</sup>N. W. Ashcroft and N. D. Mermin, *Solid State Physics* (Holt, Rinehart and Winston, New York, 1976).
- <sup>18</sup>S. B. Zhang and J. E. Northrup, Phys. Rev. Lett. **67**, 2339 (1991).
- <sup>19</sup>S. Limpijumnong, S. B. Zhang, S. H. Wei, and C. H. Park, Phys. Rev. Lett. 92, 155504 (2004).
- <sup>20</sup>S. Na-Phattalung, M. F. Smith, K. Kim, M.-H. Du, S.-H. Wei, S. B. Zhang, and S. Limpijumnong, Phys. Rev. B **73**, 125205 (2006); C. G. Van de Walle, S. Limpijumnong, and J. Neugebauer, *ibid*. **63**, 245205 (2001).
- <sup>21</sup>C. Persson, Y.-J. Zhao, S. Lany, and A. Zunger, Phys. Rev. B **72**, 035211 (2005)
- <sup>22</sup>P. Hohenberg and W. Kohn, Phys. Rev. **136**, B864 (1964); W. Kohn and L. J. Sham, Phys. Rev. **140**, A1133 (1965).
- <sup>23</sup>D. Vanderbilt, Phys. Rev. B **41**, 7892 (1990).
- <sup>24</sup>G. Kresse and J. Furthmüller, Comput. Mater. Sci. 6, 15 (1996).
- <sup>25</sup>Ph. Ghosez, E. Cockayne, U. V. Waghmare, and K. M. Rabe, Phys. Rev. B 60, 836 (1999).
- <sup>26</sup>B. G. Shirane and R. Repinsky, Acta Crystallogr. **9**, 131 (1956).
- <sup>27</sup>E. Sawaguchi, J. Phys. Soc. Jpn. **8**, 615 (1953).
- <sup>28</sup>H. J. Monkhorst and J. D. Pack, Phys. Rev. B **13**, 5188 (1976).
- <sup>29</sup>J. Robertson, W. L. Warren, and B. A. Tuttle, J. Appl. Phys. **77**, 3975 (1995).
- <sup>30</sup>V. V. Laguta, M. D. Glinchuk, I. P. Bykov, and Yu. L. Maksimenko, Phys. Rev. B **54**, 12353 (1996).
- <sup>31</sup>C. H. Peng, J.-F. Chang, and S. B. Desu, Mater. Res. Soc. Symp. Proc. 243, 21 (1992).
- $^{32}$ The overall DOS (unfilled curves in Fig. 5) is calculated from a 40-atom supercell containing one  $Mn_{Ti}$ . The Mn LDOS (filled curves in Fig. 5) is the site projected electron density of states in a sphere of a radius of 1.32 Å centered on the Mn atom.



## Philosophical Magazine First published in 1798

Publication details, including instructions for authors and subscription information: <a href="http://www.informaworld.com/smpp/title~content=t713695589">http://www.informaworld.com/smpp/title~content=t713695589</a>

# Characterization of novel pseudoelastic behaviour of zinc oxide nanowires

To cite this Article: Kulkarni, A. J., Sarasamak, K., Limpijumnong, S. and Zhou, M., 'Characterization of novel pseudoelastic behaviour of zinc oxide nanowires',

Philosophical Magazine, 87:14, 2117 - 2134

To link to this article: DOI: 10.1080/14786430701222754 URL: http://dx.doi.org/10.1080/14786430701222754

### PLEASE SCROLL DOWN FOR ARTICLE

Full terms and conditions of use: http://www.informaworld.com/terms-and-conditions-of-access.pdf

This article maybe used for research, teaching and private study purposes. Any substantial or systematic reproduction, re-distribution, re-selling, loan or sub-licensing, systematic supply or distribution in any form to anyone is expressly forbidden

The publisher does not give any warranty express or implied or make any representation that the contents will be complete or accurate or up to date. The accuracy of any instructions, formulae and drug doses should be independently verified with primary sources. The publisher shall not be liable for any loss, actions, claims, proceedings, demand or costs or damages whatsoever or howsoever caused arising directly or indirectly in connection with or arising out of the use of this material.

© Taylor and Francis 2007



# Characterization of novel pseudoelastic behaviour of zinc oxide nanowires

A. J. KULKARNI†, K. SARASAMAK‡, S. LIMPIJUMNONG‡ and M. ZHOU\*†

†The George W. Woodruff School of Mechanical Engineering, Georgia Institute of Technology, Atlanta, Georgia 30332-0405, USA ‡School of Physics, Suranaree University of Technology and National Synchrotron Research Center, Nakhon Ratchasima, Thailand

(Received 4 October 2006; in final form 17 December 2006)

We recently reported the discovery of a novel pseudoelastic behaviour resulting from a reversible phase transformation from wurtzite  $(P6_3mc)$  to a novel graphitelike hexagonal (P63/mmc) structure in [0110]-oriented ZnO nanowires under uniaxial loading [Phys. Rev. Lett. 97 105502 (2006)]. This previously unknown phenomenon is observed in nanowires and has not been reported for bulk ZnO. In this paper, molecular dynamics simulations are carried out to characterize the tensile behaviour dominated by this transformation of nanowires with lateral dimensions of 18–41 Å over the temperature range of 100–700 K. Significant size and temperature effects on the behaviour are observed. Specifically, the critical stress for the initiation of the phase transformation, the recoverable strains associated with the pseudoelasticity and the hysteretic energy dissipation are found to be both size and temperature dependent and can vary by as much as 59%, 32% and 57%, respectively. The large recoverable strains of 10–16% are unusual for the normally rather brittle ZnO ceramic and are due to both elastic stretch and the phase transformation in the slender one-dimensional nanowires. The hysteretic energy dissipation is in the range 0.05–0.14 GJ m<sup>-3</sup> per cycle and such low levels are attributed to the relatively low energy barrier for the transformation. Unlike the pseudoelasticity in fcc metal nanowires of Cu, Ni and Au, which leads to a novel shape memory effect, the pseudoelasticity quantified here does not result in a shape memory of ZnO nanowires. The primary reason is the absence of an energy barrier for the phase transformation at zero stress.

### 1. Introduction

Pseudoelasticity and the shape memory effect (SME) are traditionally associated with shape memory alloys and elastomers [1]. Such effects have recently been discovered in single crystalline metal nanowires as a consequence of their nanoscale dimensionality [2–5]. We have recently reported a novel pseudoelastic behaviour in [0110]-oriented ZnO nanowires which arises from a reversible phase transformation from a tetrahedrally coordinated wurtzite (herein denoted as WZ, *P*63*mc* space group) phase to a newly discovered graphite-like phase (herein denoted as HX,

<sup>\*</sup>Corresponding author. Email: min.zhou@gatech.edu.

P6<sub>3</sub>/mmc space group) [6]. This previously unknown five-fold coordinated polymorph of ZnO can result from either tensile loading along the [0110] direction or compressive loading along the [0001] direction. For [0110] nanowires in tension, recoverable strains, which comprise of the elastic stretching of the WZ and HX phases and a contribution from the transformation, can be up to 16%. This is quite extraordinary since ionic compound semiconductors such as ZnO, GaN, InN and BN are known to be brittle under tensile loading. While the ability to undergo a phase transformation is the primary reason for the unusual pseudoelastic behaviour, the nearly defect-free nature of these nanowires and the large surface-to-volume ratios, which enhance atomic mobility, also contribute to the wires' ability to undergo deformation without fracture. The high strengths, large recoverable strains and property variations associated with transformation make these nanowires ideal candidates for nanocomponents in a variety of nano-electromechanical systems (NEMS), such as sensors, actuators and switches. Since this pseudoelastic behaviour has just been discovered in ZnO nanowires that have only been synthesized recently, a fundamental understanding of the overall constitutive behaviour, the nature of the phase transformation and the characteristics of the transformed phase is needed in order to unleash the potential of these nanowires.

In this paper, the pseudoelastic responses of  $[01\bar{1}0]$  ZnO nanowires with lateral dimensions of  $21.22 \times 18.95$ ,  $31.02 \times 29.42$  and  $40.81 \times 39.89 \, \text{Å}^2$  under quasistatic tensile loading are characterized. The characterization accounts for temperatures between 100 and 700 K. The analysis focuses on the formation of the new HX crystalline structure and the transformation path from WZ to HX under uniaxial tensile loading. In particular, the atomic motions or lattice distortion resulting in the formation of the HX structure are quantified through the gradient of a continuum deformation map. The analysis lends itself to the quantification of the recoverable strains associated with the pseudoelastic behaviour of the nanowires, including contributions from the elastic stretching of the WZ and the HX phases and lattice size change due to the phase transformation. The size and temperature dependence of important parameters, including the critical stress for the initiation of phase transformation, maximum recoverable strain and hysteretic dissipation, are also quantified.

### 2. Computational framework

Molecular dynamics (MD) simulations using the Buckingham potential with charge interactions [7, 8] are carried out. The nanowires considered are single-crystalline and wurtzite-structured, with lattice constants  $a = 3.249 \,\text{Å}$  and  $c = 5.206 \,\text{Å}$  and a growth direction along the [0110] axis [9–11]. The wire structure is generated by repeating a wurtzite unit cell along the [2110], [0001] and [0110] directions (figure 1). Three different cross-sectional sizes (21.22 × 18.95, 31.02 × 29.42 and 40.81 × 39.89 Ų) are considered. The smallest cross-sectional size (21.22 × 18.95 Ų) is chosen such that the short-range cut-off distance in the Buckingham potential [7, 8] is smaller than the smallest wire dimension and long-range interactions are properly considered [12]. Periodic boundary conditions are specified in the axial direction. Calculations with

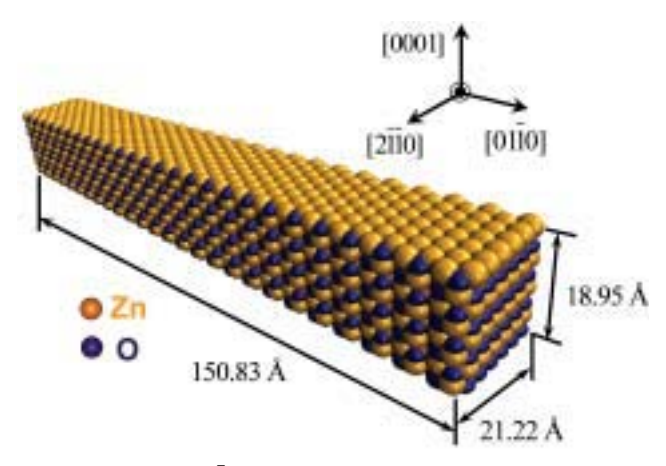


Figure 1. Configuration of a  $[01\overline{1}0]$  nanowire with lateral dimensions of  $21.22 \times 18.95 \,\text{Å}^2$  after geometric construction and before initial relaxation.

different computational cell sizes show that any length greater than 100 Å, irrespective of the cross-section size, is sufficient to avoid image effects [13, 14]. Here, a periodic computational cell length of 150.83 Å is used for all the cross-sections analyzed.

Since the crystallographically constructed nanowires may not be in equilibrium, preloading relaxations are carried out to obtain the wires' free-standing configurations. The relaxations occur at desired temperatures without external loading, until thermodynamic quantities (such as energy, stress, and temperature) indicate that statistical steady states have been reached. A relaxation time of 3 ps is found to be adequate for achieving equilibrium states for the ranges of wire size and temperature considered. During the relaxations, minimization of the wires' energy occurs through surface reconstruction and adjustment of the lattice spacing in the wire core. The surface reconstruction manifests in the forms of decreases in the interlayer spacing between outer surface layers and in-plane contractions of the surfaces [13]. Such morphological changes on surfaces and in the wires' cores are also monitored. This is especially important for nanostructures since their surface-to-volume ratios are high and extensive surface, and in some cases, core reconstructions may occur. For example, [100] oriented fcc metal nanowires are known to reconstruct into [110] orientations as a consequence of surface energy minimization [2, 4, 15, 16].

Following the initial relaxations, a quasistatic loading scheme is employed to effect tensile deformation and to obtain the mechanical response of the nanowires. Approximate quasistatic tensile loading in each deformation increment is achieved though successive loading and equilibration steps using a combination of algorithms for NPT and NVE ensembles [17]. Specifically in each deformation increment, stretching at a specified rate of  $0.005\,\mathrm{ps^{-1}}$  is first carried out for  $0.5\,\mathrm{ps}$  using a modified version of the NPT algorithm of Melchionna *et al.* [18, 19]. Subsequently, with the strain maintained constant, the nanowire is relaxed for 3 ps via an algorithm for NVE ensemble [17] at the specified temperature. This equilibration duration is chosen such that a statistically steady state is reached and no further structural

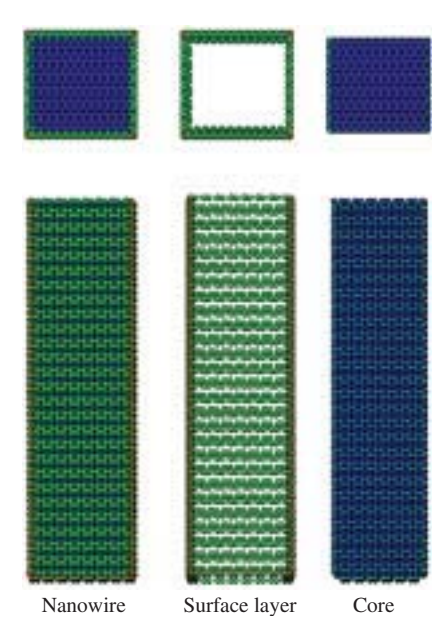


Figure 2. Decomposition of a nanowire into surface atoms and interior atoms using the coordination number (CN); the surface atoms have CNs below 4 and the core atoms have CNs equal to 4.

changes occur. It is possible that the magnitude of the strain increment in each step may affect the calculated stress-strain response. To minimize this error, calculations using series of strain increments between 0.35% and 0.1% were carried out. Based on the results, a strain increment of 0.25% and an equilibration period of 3 ps per loading step are found to minimize fluctuations in the calculated response and are used in the analysis reported. Since the loading proceeds in a series of equilibration steps, this process essentially simulates quasistatic loading of the specimen. Unloading is implemented in a similar manner with a reduction in strain for each unloading step. The virial formula is used to calculate the stress [20].

Changes in lattice structures are characterized using the average lattice constants and the radial distribution function (RDF) [21]. The average lattice constants are calculated at each strain increment by averaging local lattice constants over the bulk volume of the wire. Surface layers (figure 2) are not included in this calculation and the local lattice parameters are computed from coordinates of atoms in the wire core. The RDF describes how atoms in a system are radially packed around each other. It measures the density of atoms in a spherical shell of radius r and thickness dr surrounding an atom in the structure, i.e.

$$g(r) = \frac{n(r, r+dr)/V_S}{N/V},\tag{1}$$

where g(r) is the RDF, n(r, r+dr) is the number of atoms in the spherical shell,  $V_S = 4\pi r^2 dr$  is the volume of the spherical shell, N is the total number of atoms in the system and V is the volume of the structure. The RDFs are generated at the end

of the equilibration stage of a relevant strain increment when a steady state has been achieved. In particular, the RDFs for the WZ structure after initial relaxation and for the HX structure after transformation completion are studied to characterize the structural changes associated with the phase transformation.

### 3. Results and discussion

### 3.1. Loading response

Figure 3a shows the tensile stress–strain curve of a  $40.81 \times 39.89 \, \text{Å}^2$  wire during loading and unloading at  $100 \, \text{K}$ . The configurations of this wire at four different stages (three of which are during loading) of deformation along the curve are shown in figure 3b, with the atoms coloured by their coordination numbers. In the wurtzite structure [initial configuration, (i) in figure 3b], each atom has a coordination number of 4, typical for tetrahedral structures. Atoms on surfaces and edges have coordination numbers of 3 or less. In the HX phase [(ii) and (iii) in figure 3b], on the other hand, each atom has a coordination number of 5 due to an additional Zn–O bond along the [0001] axis as compared to the WZ phase. This five-fold coordination will be discussed later.

The loading response (figure 3a) consists of initial elastic stretching of the WZ wire  $(A \rightarrow B)$ , structural transformation from WZ to HX  $(B \rightarrow D)$  and elastic stretching of the HX wire  $(D \rightarrow E)$ , culminating in the eventual failure at E. The stress–strain relation in the elastic regime between A and B is essentially linear. Deformation beyond the elastic regime results in a stress drop from 11.31 to 10.45 GPa  $(B \rightarrow C)$ . This relaxation event indicates the initiation of a phase transformation [22]. The HX phase nucleates near the wire's surface at a strain of 0.065 (figure 3a). As the deformation progresses, the transformed region sweeps through the whole specimen  $[C \rightarrow D$  and configuration (ii) in figure 3b] and the transformation is completed at a strain of 0.108 and a stress of 10.58 GPa (point D in figure 3a). Continued loading beyond point D causes elastic stretching of the transformed structure  $[D \rightarrow E$  in figure 3a and configuration (iii) in figure 3b] and the eventual failure at a strain of 0.162 and a stress of 12.28 GPa through cleavage along  $(\bar{1}2\bar{1}0)$  type planes.

### 3.2. Crystallographic change

Figure 4 outlines the crystallographic characteristics of the initial WZ phase and the transformed HX phase. Following Limpijumnong and co-workers [23, 24], a common set of lattice parameters (a, b, c, uc and vb) for these two structures is used and illustrated in figure 4a. Additionally, two layers of atoms perpendicular to the [01 $\bar{1}$ 0] direction and two layers perpendicular to the [2 $\bar{1}\bar{1}$ 0] direction are shown in figures 4b and c, respectively, to delineate the atomic motions associated with the transformation. The figure shows that, as a result of the transformation, the (0001) Zn and O basal planes become coplanar and the HX structure acquires a new symmetry (mirror plane perpendicular to the [0001] axis). Consequently, an

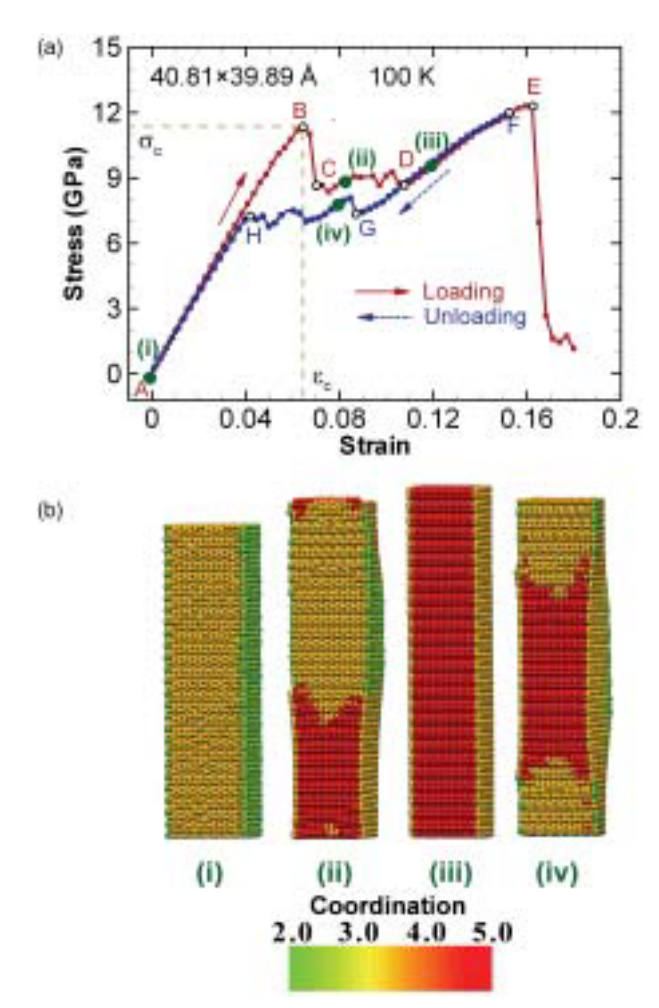


Figure 3. Tensile behaviour of a  $40.81 \times 39.89\,\mathring{A}^2$  nanowire: (a) stress–strain curve under loading and unloading; (b) deformed configurations at different stages of loading and unloading.

additional Zn–O bond is formed along the [0001] axis (figures 4b and c), giving the HX phase a five-fold coordination. Table 1 lists the lattice parameters for the WZ and HX structures at several stress levels for the  $40.81 \times 39.89 \, \text{Å}^2$  wire. During the deformation, u=uc/c changes from its initial value of 0.4 for WZ to a value of 0.5 for HX, implying the flattening of buckled wurtzite basal planes. A similar unbuckled structure has been observed in GaN, MgO and ZnO thin films as a result of extensive surface reconstructions to suppress surface polarity [25–28].

Figure 5 shows the RDF profiles before loading is applied (point A,  $\sigma = 0$  GPa) and upon completion of the WZ  $\rightarrow$  HX transformation (point D,  $\sigma = 8.58$  GPa) for the nanowire in figure 3. The profile for the initial wire (WZ structure) has its first

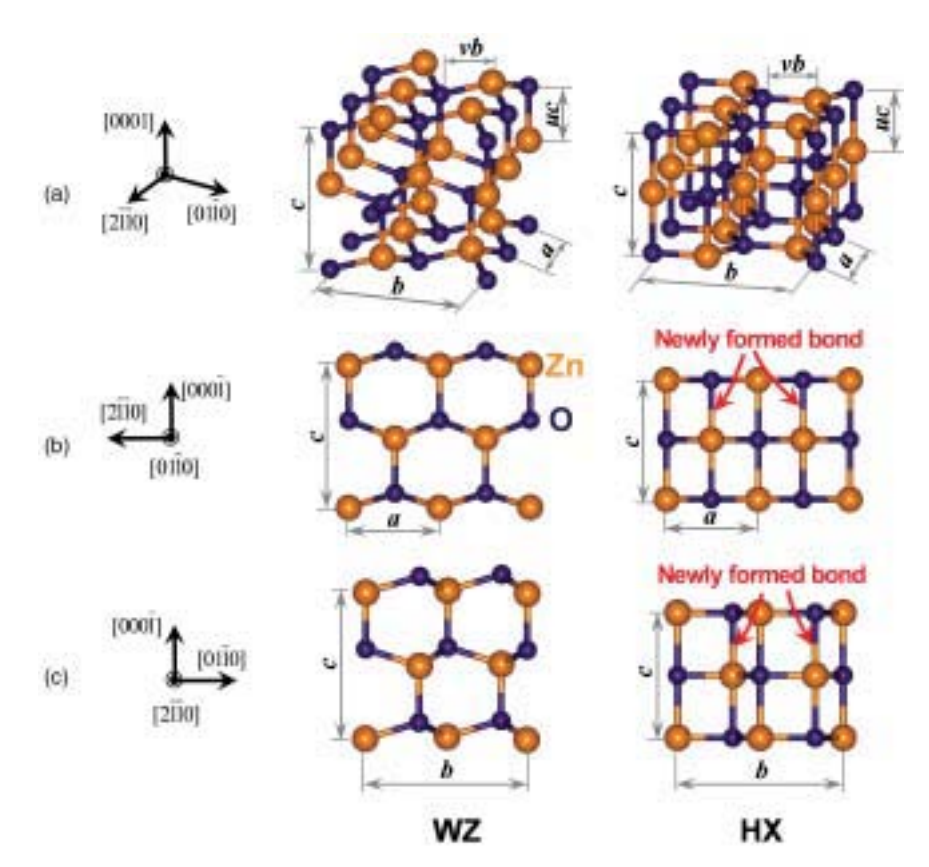


Figure 4. Illustrations of the WZ and HX structures involved in the phase transformation: (a) lattice structures of the WZ and HX phases; (b) atomic arrangement on  $[01\bar{1}0]$  plane; (c) atomic arrangement on  $[2\bar{1}\bar{1}0]$  plane.

Table 1. Lattice parameters for WZ, HX and RS under different loading conditions for a  $40.81 \times 39.89\,\text{Å}^2$  nanowire.

	WZ			HX	
Parameter	$\sigma = 0 \text{ GPa}$ $\varepsilon = 0^{a}$	$\sigma = 0 \text{ GPa}$ $\varepsilon = 0$	$\sigma = 11.39 \text{ GPa}$ $\varepsilon = 0.065$	$\sigma = 8.58 \text{ GPa}$ $\varepsilon = 0.108$	$\sigma = 12.29 \text{ GPa}$ $\varepsilon = 0.162$
(Å) b (Å) v c (Å) u b/a c/a	3.25 5.63 0.33 5.21 0.38 1.73 1.60	3.26 5.62 0.32 5.18 0.41 1.74	3.23 6.05 0.29 4.92 0.46 1.87 1.53	3.38 6.22 0.31 4.30 0.50 1.84	3.40 6.62 0.29 4.15 0.49 1.95

<sup>&</sup>lt;sup>a</sup>Experiment [29].

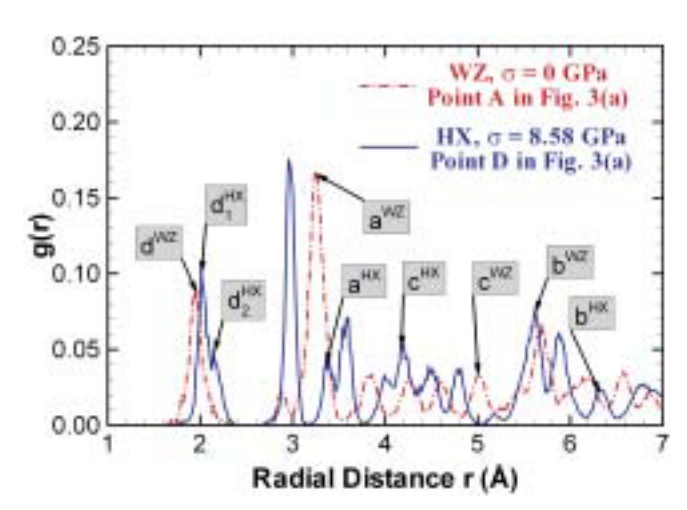


Figure 5. Radial distribution function profiles for a  $40.81 \times 39.89 \,\text{Å}^2$  nanowire before loading (point A in figure 3a] and upon completion of phase transformation (point D in figure 3a).

peak at a radial distance of 1.93 Å, indicating a Zn-O bond distance consistent with the experimental value of 1.95 Å [29]. Upon completion of the WZ  $\rightarrow$  HX transformation at point D, this peak has split into two peaks with the primary peak at 1.98 Å and the secondary peak at 2.20 Å. The primary peak corresponds to Zn-O bonds in the basal ({0001}) plane of the HX structure, while the secondary peak is associated with the additional bonds formed along the [0001] axis (see figure 4). Also seen in figure 5 are peaks corresponding to lattice constants a, b and c. Initially in the WZ phase, the 'a' peak is at 3.26 Å and the 'c' peak is at 5.18 Å. The transformation to HX results in the shift of the 'a' peak to 3.38 Å and the shift of the 'c' peak to 4.30 Å. These shifts indicate that the transformation to the HX structure involves both an expansion of the basal planes (increase in 'a') to accommodate the flattening of the buckled plane and a contraction in 'c' which results in the formation of the Zn-O bond along the [0001] axis. The transformation is also associated with a shift of the 'b' peak from 5.60 Å for WZ to 6.22 Å for HX, consistent with the nature of the applied tensile loading. The values reported in table 1 also show a progressive increase in the lattice parameter b toward 6.22 Å as the stress is increased towards the level of 8.58 GPa at the completion of the transformation. Further load increases are accompanied by increases in b with the associated RDF peak shifting toward a higher value (not shown).

### 3.3. Characterization of the deformation

The deformation can be quantified in a continuum sense through the deformation gradients  $F_i$  (i=1,2, and 3) associated with the three stages of deformation, with i=1 denoting the first stage (elastic stretching of WZ, A  $\rightarrow$  B in figure 3a), i=2 denoting the second stage (transformation from WZ to HX, B  $\rightarrow$  D in figure 3a) and i=3 denoting the third stage (elastic stretching of HX, D  $\rightarrow$  E in figure 3a). In such

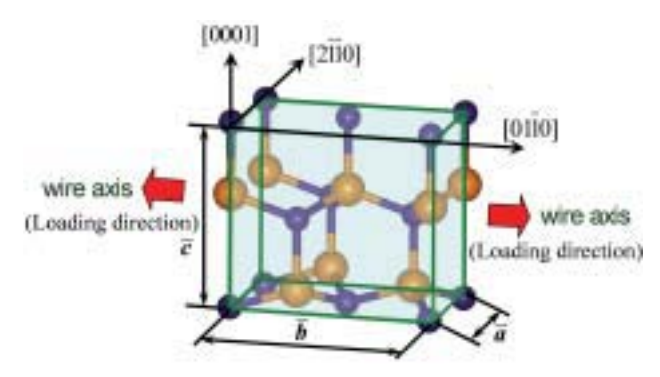


Figure 6. Representative volume defined in a unit cell of the wurtzite lattice for the purpose of deformation analysis.

an analysis, the deformation of a representative volume of  $\Omega = \bar{a} \times \bar{b} \times \bar{c}$  (figure 6) is used, with dimensions  $\bar{a}$ ,  $\bar{b}$  and  $\bar{c}$  being the average values of lattice constants a, b and c, respectively. Since the average values of the lattice parameters are used here, the deformed wire is regarded as a repetition of this representative volume. The deformation gradient for each stage can then be expressed as

$$F_{i} = \begin{pmatrix} \frac{\bar{a}_{i}}{\bar{a}_{i-1}} & 0 & 0\\ 0 & \frac{\bar{c}_{i}}{\bar{c}_{i-1}} & 0\\ 0 & 0 & \frac{\bar{b}_{i}}{\bar{b}_{i-1}} \end{pmatrix}, \quad i = 1, 2, 3.$$
 (2)

In the above expressions,  $\bar{a}_{i-1}$ ,  $\bar{b}_{i-1}$ , and  $\bar{c}_{i-1}$  are the average lattice constants at the beginning of stage i and  $\bar{a}_i$ ,  $\bar{b}_i$ , and  $\bar{c}_i$  are the average lattice constants at the end of stage i. Note that  $\bar{a}_0$ ,  $\bar{b}_0$ , and  $\bar{c}_0$  are the constants for the initial (undeformed, WZ) wire. The relative volume change associated with stage i is

$$\frac{\Omega_i}{\Omega_{i-1}} = \det(\mathbf{F}_i),\tag{3}$$

where  $\Omega$  is the volume of the wire at the beginning and end of stage *i*, respectively. For a  $40.81 \times 39.89 \,\text{Å}^2$  wire at  $100 \,\text{K}$ , the deformation gradient for the first stage (A  $\rightarrow$  B in figure 3a) is

$$F_1 = \begin{pmatrix} 0.991 & 0 & 0 \\ 0 & 0.960 & 0 \\ 0 & 0 & 1.065 \end{pmatrix}. \tag{4}$$

The associated volume increase is 1.27% and the longitudinal (elastic) strain  $\varepsilon_{33} = F_1^{33} - 1 = 0.065$  consistent with that seen from the stress-strain curve in figure 3.

During the second stage of deformation (phase transformation  $B \to D$  in figure 3a),  $\bar{a}$  increases and  $\bar{c}$  decreases. The corresponding deformation gradient is

$$\mathbf{F}_2 = \begin{pmatrix} 1.047 & 0 & 0\\ 0 & 0.876 & 0\\ 0 & 0 & 1.043 \end{pmatrix}. \tag{5}$$

The volume ratio associated with the transformation is  $\Omega_2/\Omega_1 = 0.957$ , indicating a slight decrease in volume of 4.3%. This decrease in volume under tensile loading is counterintuitive. It is a direct consequence of the discrete lattice structure and the structural transformation. Specifically, the uniaxial tensile stress in the [0110] or 'b' direction causes the interatomic distances in the [0001] Zn and O basal planes (a) to increase, causing the two types of basal planes to become coplanar and, therefore, the volume decrease.

The deformation gradient for the elastic deformation of the HX phase in the third stage ( $D \rightarrow E$  in figure 3a) is

$$\mathbf{F}_3 = \begin{pmatrix} 1.008 & 0 & 0\\ 0 & 0.962 & 0\\ 0 & 0 & 1.05 \end{pmatrix}. \tag{6}$$

Although the 'a' and 'b' directions are perpendicular to each other, a increases slightly (with a corresponding strain of  $\varepsilon_{11} = 0.008$ ) under the tensile loading along the 'b' direction. This gives rise to a negative phenomenological Poisson's ratio of

$$v_{13} = -\frac{\varepsilon_{11}}{\varepsilon_{33}} = -0.16. \tag{7}$$

The total elastic strain of the wire beyond the completion of the phase transformation and before fracture (between D and F in figure 3a) is  $\varepsilon_{33} = F_3^{33} - 1 = 0.05$ . Here, the reference state of this strain is the length of the wire at the completion of transformation (point D). The corresponding volume increase is 1.68%.

Overall, the total strain of the wire between points A and E is  $\varepsilon = F_1^{33} F_2^{33} F_3^{33} - 1 = 0.162$ . Here, the reference length is the original length of the wire.

### 3.4. Unloading response

Unloading of an HX structured wire from any strain prior to wire fracture activates a novel pseudoelastic behaviour. Take the wire in figure 3 for example; unloading from a strain of 14.5% (point F) initially results in the recovery of the elastic straining of the HX structure embodied in  $F_3$  and goes beyond the end point of the WZ  $\rightarrow$  HX transformation during loading (point D). This elastic unloading within the HX structure continues until point G where a reverse transformation from HX to WZ initiates at a strain of 0.087 and a stress of 7.38 GPa. Further unloading results in the complete reversal of the HX  $\rightarrow$  WZ transformation at H (with a strain of 0.039 and a stress of 7.04 GPa). Unloading between H and A follows the elastic trend of the WZ phase and the hysteresis loop is completed.

For the wire in figure 3, the total recoverable strain is  $\sim$ 16% which is significant since ZnO is a ceramic. The hysteretic energy dissipation in one loading and

unloading cycle is  $\sim 0.14\,\mathrm{GJ\,m^{-3}}$ . This dissipation level is significantly lower than that observed for wurtzite to rock salt (WZ  $\rightarrow$  RS) transformations in bulk ZnO ( $\sim 1.38\,\mathrm{GJ\,m^{-3}}$  per cycle), therefore, limiting heat generation and heat-related damage and making the nanowires ideal for applications involving cyclic loading and unloading [30]. The low level of dissipation can be attributed to the fact that (i) the crystallographic transition between the WZ and HX structures, which does not require the formation of defects such as dislocations or twin boundaries, is smooth and (ii) the energy barrier for the transformation between the WZ and the HX structures is relatively low [6].

### 3.5. Effects of size and temperature

Temperature and lateral dimensions have significant effects on the pseudoelastic behaviour of the wires. Figures 7a–c show the loading part of the stress–strain curves over 100–700 K for the 21.22 × 18.95, 31.02 × 29.42 and 40.81 × 39.89 Å<sup>2</sup> nanowires, respectively. The critical stress for the nucleation of the HX phase ( $\sigma_c$ ) is marked by open circles in these figures. Figure 7d shows the variation of this critical stress as a function of size and temperature. Overall, the critical stress decreases as the wire size

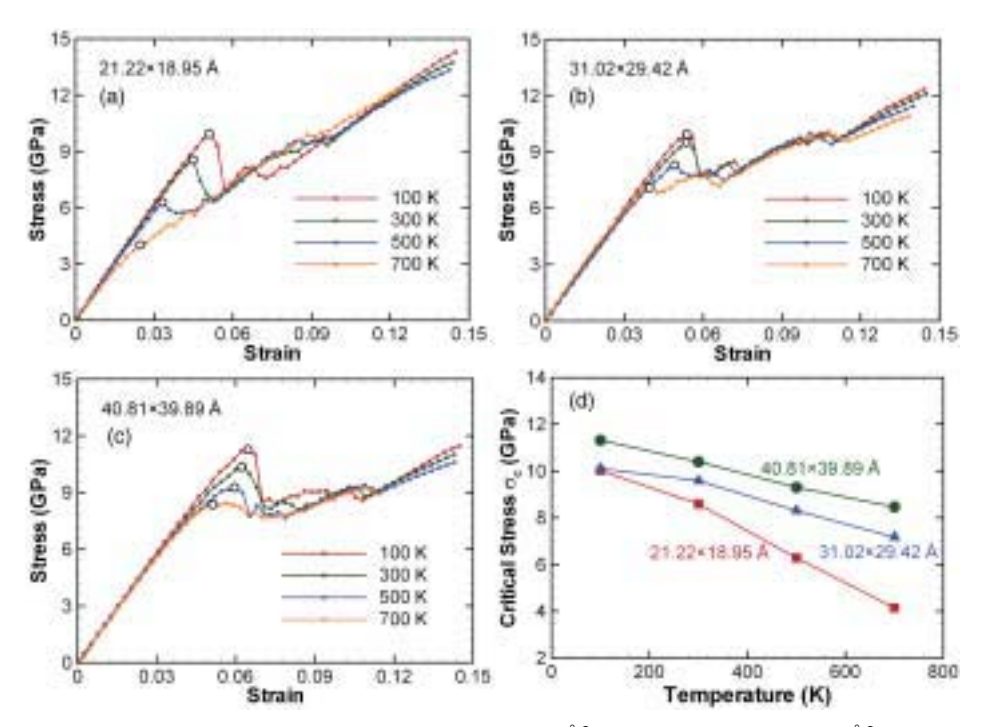


Figure 7. Stress–strain curves of (a) a  $21.22 \times 18.95 \,\text{Å}^2$  wire, (b) a  $31.02 \times 29.42 \,\text{Å}^2$  wire and (c) a  $40.81 \times 39.89 \,\text{Å}^2$  wire at different temperatures. (d) The critical stress for the initiation of phase transform ( $\sigma_c$ ) as a function of lateral dimensions and temperature.

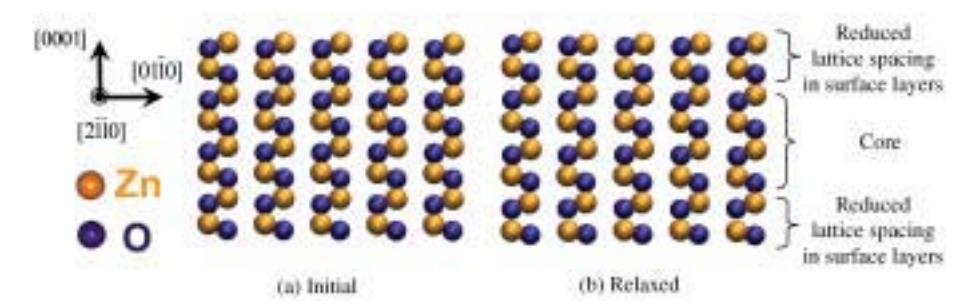


Figure 8. Surface reconstruction of a  $21.22 \times 18.95 \,\mathring{A}^2$  nanowire at  $100 \, K$  relative to its configuration in bulk ZnO, the images correspond to the states of the wire after (a) geometric construction (before initial relaxation) and (b) after initial relaxation.

is reduced. The critical stress also decreases as temperature is increased. Over the temperature range analyzed,  $\sigma_c$  for the  $31.02 \times 29.42\,\text{Å}^2$  wire is up to 42% higher than that for the  $21.22 \times 18.95\,\text{Å}^2$  wire, whereas the values for the  $40.81 \times 39.89\,\text{Å}^2$  wire are approximately 11-15% higher than those for the  $31.02 \times 29.42\,\text{Å}^2$  wire. In contrast to the well-established trend that the stiffness of nanowires increases as wire size is reduced [13],  $\sigma_c$  decreases as the wire size is reduced. The higher surface-to-volume ratios at smaller wire sizes cause both effects. Note that, as the wire size is reduced from 50 Å to 10 Å, the surface-to-volume ratio increases by  $\sim 35\%$ . In particular, for polar (0001) surfaces (figure 1), the imbalance of charges results in extensive surface reconstruction.

Figure 8 shows the positions of atoms on layers perpendicular to the [0001] direction before and after the initial relaxation. Obviously, relative to the ideal bulk structure, the surface layers contract and the Zn and O basal planes become essentially coplanar, resulting in a layered surface structure (LY) which is crystallographically similar to the HX structure. This phenomenon has been predicted by first-principle calculations and observed in experiments on ZnO nanofilms [25, 26]. The reconstructed LY surfaces in the initial wire before loading play an important role because they can act as nucleation sites for and lower the energy barrier of the WZ  $\rightarrow$  HX transformation due to the geometric similarities between the LY and HX structures. The smaller wire cores at smaller wire sizes facilitate the initiation of the phase transformation from the surfaces, resulting in the lower  $\sigma_c$  values.

As the temperature increases from  $100\,\mathrm{K}$  to  $700\,\mathrm{K}$ , a 25.2% decrease in  $\sigma_c$  is observed for the  $40.81\times39.89\,\mathrm{\mathring{A}}^2$  wire (figure 7d). This effect is attributed to thermal softening and the ability of the nanowire to overcome the energy barrier for the transformation at higher temperatures. Note that over the same range of temperature, the elastic modulus of the nanowire decreases by 24% [13]. Temperature changes also significantly affect hysteretic dissipation. To illustrate this effect, the stress-strain curves of the  $40.81\times39.89\,\mathrm{\mathring{A}}^2$  wire at  $100\,\mathrm{K}$ ,  $300\,\mathrm{K}$ ,  $500\,\mathrm{K}$  and  $700\,\mathrm{K}$  are shown in figure 9.

The corresponding dissipation during the loading–unloading cycle, along with those for the  $21.22 \times 18.95$  and  $31.02 \times 29.42$  Å<sup>2</sup> wires at these temperatures, is given

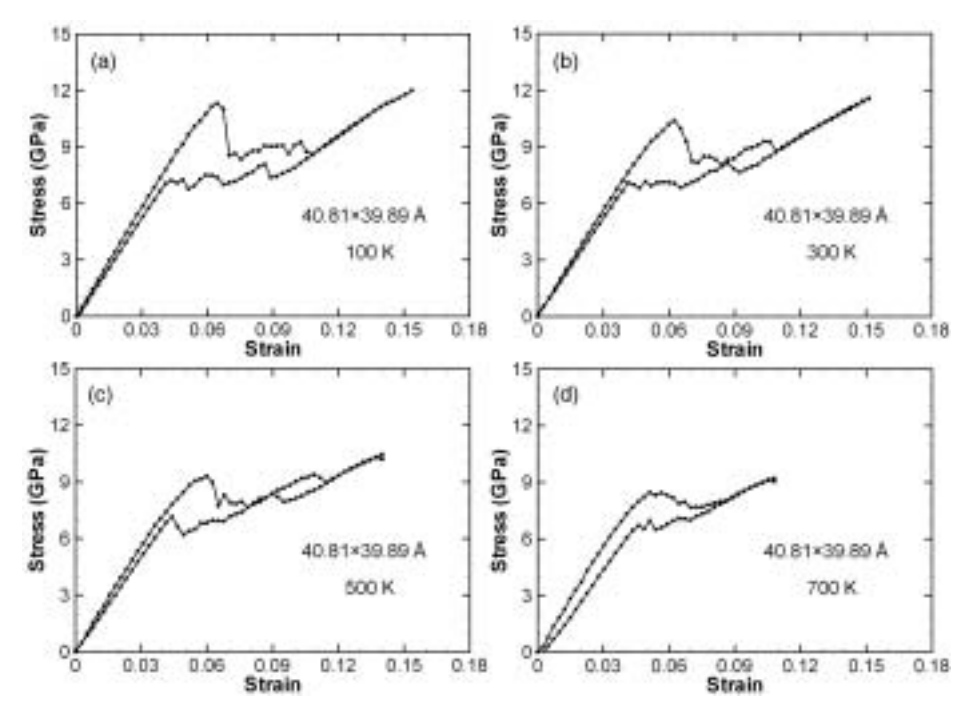


Figure 9. Stress–strain responses of a  $40.81 \times 39.89 \, \text{Å}^2$  wire during one loading–unloading cycle at (a)  $100 \, \text{K}$ , (b)  $300 \, \text{K}$ , (c)  $500 \, \text{K}$  and (d)  $700 \, \text{K}$ .

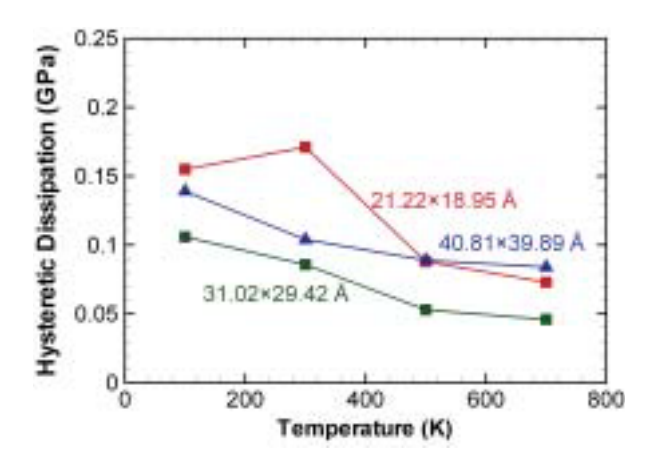


Figure 10. Hysteretic dissipation in one loading-unloading cycle as a function of lateral dimensions and temperature.

in figure 10. For the  $40.81 \times 39.89\,\text{Å}^2$  wire, the dissipation decreases by 39.6% as temperature is increased from  $100\,\text{K}$  to  $700\,\text{K}$ . A similar trend is seen for the  $21.22 \times 18.95$  and  $31.02 \times 29.42\,\text{Å}^2$  wires which show decreases of 52.9% and 56.6%, respectively, over the same temperature range.

Table 2. Size and temperature dependence of the stress-strain response of the nanowires.

Cross-section dimensions $(\mathring{A}^2)$	Temperature (K)	$\sigma_c$ (GPa)	$arepsilon_c$	Strain at completion of transformation	Maximum recoverable strain	Ultimate tensile strength (GPa)	Hysteretic dissipation (GJ m <sup>-3</sup> )
$21.22 \times 18.95$	100	10.02	0.051	0.100	0.165	15.56	0.155
	300	8.59	0.045	0.096	0.155	14.50	0.171
	500	6.29	0.033	0.097	0.148	13.56	0.088
	700	4.15	0.027	0.091	0.127	12.34	0.073
$31.02 \times 29.42$	100	10.10	0.053	0.110	0.155	13.05	0.106
	300	9.59	0.053	0.110	0.154	12.50	0.086
	500	8.31	0.049	0.098	0.140	11.44	0.053
	700	7.17	0.040	0.116	0.138	10.89	0.046
$40.81 \times 39.89$	100	11.32	0.065	0.108	0.159	12.30	0.139
	300	10.40	0.063	0.109	0.162	11.68	0.104
	500	9.31	0.060	0.114	0.143	10.60	0.089
	700	8.47	0.051	0.086	0.108	9.21	0.084

Table 2 lists the values of several key parameters quantifying the pseudoelastic behaviour at various cross-sectional sizes and temperatures. In particular, note that the maximum recoverable strain decreases significantly as temperature is increased, while the strain at which the  $WZ \rightarrow HX$  transformation completes is essentially temperature-independent. The enhanced mobility of atoms at higher temperatures promotes the formation of defects and may be a factor contributing to the failure at lower strain levels.

# 3.6. Pseudoelasticity without shape memory

The pseudoelastic behaviour quantified here is reminiscent of a very similar pseudoelastic behaviour (which leads to a novel shape memory effect) in fcc metal nanowires discovered and analyzed by Liang *et al.* [3, 4]. This similarity in the pseudoelastic behaviours between nanowires of the two classes of materials naturally raises the question of whether a similar SME also exists in the ZnO nanowires analyzed here. To answer this question, we first note that the pseudoelasticity and the SME in the fcc metal nanowires are driven primarily by a surface-stress-induced lattice reorientation process which requires the formation of intermediate transitional structures involving partial dislocations. One attribute of that unique lattice reorientation process is that an energy barrier exists between the phases even at very low temperatures. Therefore, spontaneous relaxation occurs only at temperatures above a critical value. It is this temperature dependence that gives rise to the SME in the fcc metal wires.

To ascertain if a SME exists in the ZnO nanowires analyzed here, partially and fully transformed wires were cooled to various final temperatures, the lowest being 10 K. Subsequently, unloading is carried out at the low temperatures to determine if the HX phase can be retained without external stress. For all wire sizes considered and under all initial/final temperature combinations analyzed, the wires reverted

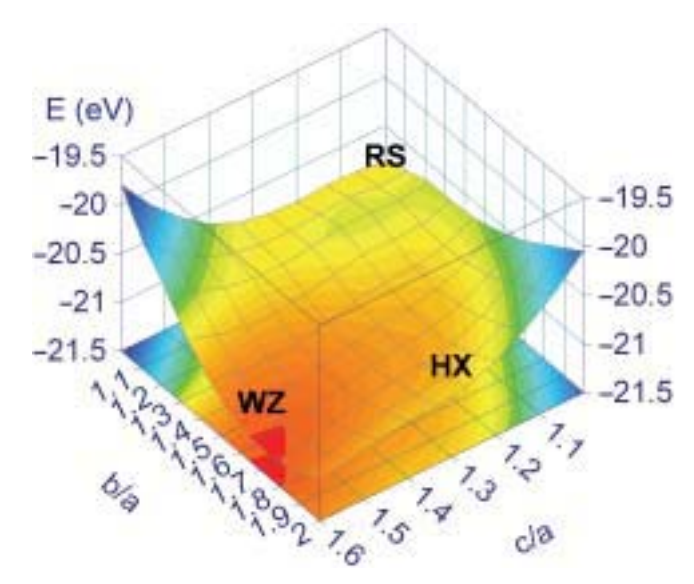


Figure 11. Potential energy map of ZnO with highlights of the WZ, RS and HX lattice structures.

fully back to the WZ structure. This result shows that there is no critical temperature below which either partially or fully HX-structured wires can exist without external loading. The absence of such a critical temperature and the lack of an HX structure at zero loading effectively rule out the possibility of a SME in the ZnO nanowires. This finding can be explained by the enthalpy surface for ZnO at 0 K and zero external loading. Figure 11 shows the potential energy profile of one ZnO unit cell at different structural configurations (when there is no external loading, the enthalpy is equal to the potential energy). This profile is obtained through first principle calculations, details of which are provided by Kulkarni et al. [6] and Limpijumnong and Jungthawan [23]. Lattice structures corresponding to WZ, RS and HX are labelled in this figure. Note that only two local minima (energy wells) exist, one at the WZ structure and the other at the RS structure. A well is not seen at the HX structure. Obviously, WZ is the stable phase and any sample with the HX structure would spontaneously transform into the WZ structure. On the other hand, the RS structure is a metastable phase which may exist if temperature and load histories are carefully controlled. In contrast, it is not possible for HX to exist without loading since no energy well is seen for it on the energy surface. Of course, the enthalpy surface can be modified by appropriate external loading to include a local minimum (well) at the HX structure. Tensile loading of sufficient magnitude along the b-direction is such an example and has been shown to cause the WZ  $\rightarrow$  HX phase transformation [6]. Crystallographically, the two-way WZ ↔ HX transformation occurs through smooth lattice structure evolution without the formation of defects or intermediate structures. In particular, the process can be illustrated by a look at the buckling and unbuckling of the [0001] Zn and O basal planes.

Figure 12 shows the evolution of the 3-D O–Zn–O bond angle ( $\alpha$ ) at various stages of deformation. The strain values are associated with the loading process of

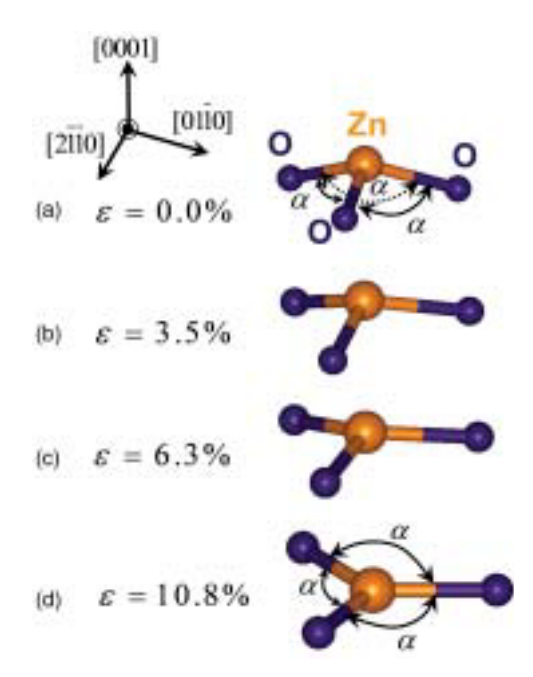


Figure 12. Increase in the O–Zn–O bond angle ( $\alpha$ ) between Zn and O atoms on [0001] basal planes at various levels of strain during tensile loading along the [0110] wire axis.

the  $40.81 \times 39.89 \,\text{Å}^2$  wire. The evolution of  $\alpha$  during unloading is very similar except that the corresponding wire strain values are slightly different. For a perfect, undeformed WZ lattice,  $\alpha \approx 108.2^{\circ}$  (figure 12a). As deformation progresses,  $\alpha$  increases as loading is increased and the structure evolves (figures 12b and c). Upon full WZ  $\rightarrow$  HX transformation, the basal planes flatten out and  $\alpha$  becomes 120° (figure 12d), at the same time, a new bond is formed along the [0001] axis (figures 4b and c). During unloading, the reverse process is seen, with  $\alpha$  decreasing as the load is decreased. The lack of defect or intermediate structure formation in the process makes ZnO nanowires different from FCC metal nanowires such that the energy requirement for the nucleation of the WZ  $\leftrightarrow$  HX transformation is very low. Therefore, during the actual unloading of a HX wire, the barrier for the  $HX \rightarrow WZ$ transformation is primarily due to the breaking of the additional [0001] bond formed during the forward transformation. This barrier is relatively small [6] and is easily overcome by the strain energy stored in the HX structure. Consequently, spontaneous HZ 

WZ transformation occurs at all temperatures and no SME is observed in the ZnO nanowires.

# 4. Conclusions

A novel pseudoelastic behaviour we discovered recently in [0110]-oriented ZnO nanowires over the temperature range 100–700 K has been characterized.

MD simulations of the uniaxial tensile loading and unloading of nanowires with lateral dimensions between 18 and 41 Å show that this behaviour results from a unique structural transformation from WZ to a previously unknown phase (herein referred to as HX). Crystallographically, this newly discovered polymorph of ZnO has a five-fold coordination, in contrast to the four-fold coordination of the initial WZ structure, implying that the transformation proceeds towards higher ionicity. The transformation is fully reversible upon unloading with recoverable strains up to 16%. The hysteretic dissipation associated with a loading-unloading cycle is 0.05–0.14 GJ m $^{-3}$  and this value is significantly lower then the value for the reversible WZ–RS transformation in ZnO.

Significant temperature and size dependence of the pseudoelastic response is observed. In particular, the critical stress for the nucleation of the HX phase and the maximum recoverable strain decreases as temperature increases. In addition, the critical stress is lower at smaller wire sizes. Extensive surface reconstructions that minimize surface charge polarity and surface energy contribute to these temperature-and size-effects.

Unlike the pseudoelasticity in fcc metal nanowires, which was discovered recently by Liang *et al.* [2–4] and underlies a novel shape memory effect, the pseudoelasticity in the ZnO nanowires analyzed here does not lead to a SME. The primary reason for this lack of an SME is the absence of an energy barrier between the WZ and the HX lattice structures when no external loading is applied. The absence of an energy barrier between WZ and HX at zero stress can be regarded as a consequence of the smooth and continuous nature of the crystallographic transition which does not require the formation of defects such as dislocations and twin boundaries. The result is that stretched HX ZnO nanowires can spontaneously revert back to the WZ state at any temperature.

# Acknowledgements

AJK and MZ acknowledge support through NSF grant no. CMS9984298 and NSFC grant no. 10528205. SL & KS are supported by NANOTEC through grant no. NN49-024 and TRF through grant nos. BRG4880015 & PHD/0264/2545. The computations are carried out at the NAVO, ARL and ASC MSRCs through AFOSR MURI no. D49620-02-1-0382. We thank Dr. Bill Smith for sharing the molecular dynamics code DL\_POLY [31]. Images of deformation in this paper are created with the graphics package Visual Molecular Dynamics (VMD) [32].

#### References

- [1] K. Otsuka and C.M. Wayman, *Shape Memory Materials* (Cambridge University Press, New York, 1998).
- [2] W. Liang and M. Zhou, J. Engng Mater. Technol. 127 123 (2005).
- [3] W. Liang and M. Zhou, Phys. Rev. B 73 115409 (2006).

- [4] W. Liang, M. Zhou and F.J. Ke, Nano Lett. 5 2039 (2005).
- [5] H.S. Park, K. Gall and J.A. Zimmerman, Phys. Rev. Lett. 95 255504 (2005).
- [6] A.J. Kulkarni, M. Zhou, K. Sarasamak, et al., Phys. Rev. Lett. 97 105502 (2006).
- [7] D.J. Binks and R.W. Grimes, J. Amer. Ceram. Soc. 76 2370 (1993).
- [8] D. Wolf, P. Keblinski, S.R. Phillpot, et al., J. Chem. Phys. 110 8254 (1999).
- [9] Z.L. Wang, J. Phys. Cond. Matt. 16 R829 (2004).
- [10] Z.L. Wang, Mater. Today 7 26 (2004).
- [11] Z.L. Wang, Annu. Rev. Phys. Chem. 55 159 (2004).
- [12] A.J. Kulkarni, M. Zhou and F.J. Ke, Nanotechnology 16 2749 (2005).
- [13] A.J. Kulkarni and M. Zhou, Acta Mech. Sin. 22 217 (2006).
- [14] A.J. Kulkarni and M. Zhou, Appl. Phys. Lett. 88 141921 (2006).
- [15] J. Diao, K. Gall and M.L. Dunn, Nature Mater. 2 656 (2003).
- [16] J. Diao, K. Gall and M.L. Dunn, Phys. Rev. B 70 075413 (2004).
- [17] J.M. Haile, Molecular Dynamics Simulation (Wiley-Interscience, New York, 1997).
- [18] S. Melchionna, G. Ciccotti and B.L. Holian, Molec. Phys. 78 533 (1993).
- [19] D. Spearot, K. Jacob and D.M. McDowell, Acta Mater. 53 3579 (2005).
- [20] M. Zhou, Proc. R. Soc. 459 2347 (2003).
- [21] J.M.J.V. Leeuwen, J. Groeneveld and J.D. Boer, Physica 25 792 (1959).
- [22] G.B. Olson and M. Cohen, J. Phys., Paris 43 4 (1982).
- [23] S. Limpijumnong and S. Jungthawan, Phys. Rev. B 70 054104 (2004).
- [24] S. Limpijumnong and W.R.L. Lambrecht, Phys. Rev. Lett. 86 91 (2001).
- [25] F. Claeyssens, C.L. Freeman, N.L. Allan, et al., J. Mater. Chem. 15 139 (2005).
- [26] C.L. Freeman, F. Claeyssens, N.L. Allan, et al., Phys. Rev. Lett. 96 066102 (2006).
- [27] J. Goniakowski, C. Noguera and L. Giordano, Phys. Rev. Lett. 93 215702 (2004).
- [28] R.B. Capaz, H. Lim and J.D. Joannopoulos, Phys. Rev. B 51 17755 (1995).
- [29] D.J. Binks, Computational modelling of zinc oxide and related oxide ceramics. PhD thesis, University of Surrey (1994).
- [30] S. Desgreniers, Phys. Rev. B 58 14102 (1998).
- [31] W. Smith and T.R. Forester,  $DL\_POLY a$  Molecular Simulation Routine (Central Laboratory of Research Councils, Daresbury, 1996).
- [32] W. Humphrey and A. Dalke, J. Molec. Graphics 14 33 (1996).



Available online at www.sciencedirect.com



**CERAMICS** INTERNATIONAL

Ceramics International 34 (2008) 727-729

www.elsevier.com/locate/ceramint

# EXAFS study on the site preference of Mn in perovskite structure of PZT ceramics

B. Cherdhirunkorn <sup>a,\*</sup>, M.F. Smith <sup>b</sup>, S. Limpijumnong <sup>b,c</sup>, D.A. Hall <sup>d</sup>

<sup>a</sup> Department of Physics, Faculty of Science and Technology, Thammasart University, Thailand
 <sup>b</sup> National Synchrotron Research Center, Nakhon Ratchasima 30000, Thailand
 <sup>c</sup> School of Physics, Suranaree University of Technology, Nakhon Ratchasima 30000, Thailand
 <sup>d</sup> Manchester Materials Science Centre, University of Manchester, M1 7HS, UK

Available online 25 September 2007

#### Abstract

Synchrotron extended X-ray absorption fine structure (EXAFS) measurements at the Mn K edge were performed on Mn-doped PZT ceramics with Mn concentrations of 0.5, 1.0 and 2.0 mol%. The Fourier transforms of EXAFS structures from all samples are similar and agree well with the model of Mn substituting on the Ti/Zr site (i.e. the B site of the perovskite ABO $_3$  structure). This shows that Mn predominantly substituted for Ti/Zr in the range of concentration under study.

© 2007 Elsevier Ltd and Techna Group S.r.l. All rights reserved.

Keywords: D. PZT; EXAFS and defects

### 1. Introduction

PZT ceramics have been used widely as piezoelectric components in applications such as sensors, actuators, transformers, transducers and ultrasonic motors. The required properties for different applications can be obtained conveniently by the change of the PZT composition (Zr/Ti ratio) and the addition of cation dopants in the structure. Manganese oxide is one of the most effective dopants for hard PZT ceramics. Studies concerning Mn doped PZT ceramics have been reported elsewhere [1–4].

Conventionally, it has been supposed that  $Mn^{2+}$  and  $Mn^{3+}$  ions substitute for  $Zr^{4+}$  and  $Ti^{4+}$  ions on the B-site of the  $ABO_3$  perovskite structure, forming acceptor-type defect. Nevertheless, in recent works [3,5–7], it has been observed that at substitution levels below 1 at%, the addition of Mn to PZT ceramics gives rise to unexpected increases in the dielectric and piezoelectric coefficients, and an increase in nonlinearity. In other words, this could be an indicator for donor defects in low Mn level doped PZT ceramics. However, the nature of the

Synchrotron light is one of the most powerful tools for investigating structure of materials. The extended X-ray absorption fine structure (EXAFS) technique is one of the techniques utilizing the synchrotron light, which allows the local structure of the interesting atoms or ions in the structure of materials to be investigated [8,9]. The local structure around Mn ions within the PZT lattice can be investigated using EXAFS technique.

# 2. Experimental procedure

PZT samples were prepared according to the formula Pb  $(Zr_{0.54}Ti_{0.46})_{1-x-y}$   $Mn_x$   $Mg_y$   $O_3$  (with y=0 and 0.01, x=0, 0.005, 0.01 and 0.02) by a conventional mixed oxides method. Magnesium was employed in some of these compositions to provide a well-defined acceptor-type base composition, which could be compensated by any donor-type defects present. The raw materials, PbO (>99.9%, Penarroya Oxide), TiO<sub>2</sub> (>99.9%, Tioxide Group Limited),  $ZrO_2$  (>99.9%, MEL Chemical E101) and dopants; MnO (>99% Aldrich) and MgO (>99.95% Alfa Aesar) were mixed and milled with isopropanol for 20 h, and were then oven dried at 100 °C. The dried mixtures were calcined at 850 °C.

donor-type defects is still unclear. Furthermore, the site occupation by Mn is still a matter of controversy.

<sup>\*</sup> Corresponding author. Tel.: +66 2 5644529; fax: +66 2 5644484. E-mail address: benya@tu.ac.th (B. Cherdhirunkorn).

The calcined PZT powders were vibrational milled with water for 20 h. At this stage, 0.5 wt% PVA and 0.5 wt% PEG were added in the mixtures. The slurries were freeze dried producing fine uniform powders.

The powders were uniaxially pressed into a 10 mm diameter die with the load of 100 MPa. All samples were sintered in a closed alumina crucible and Pb-rich atmosphere at 1250  $^{\circ}$ C. Crystal structures of sintered specimens were investigated using X-ray diffractometer (Philips PW 3020).

EXAFS measurements were performed on the PZT ceramics in order to study the local structure around Mn ions in the PZT perovskite structure. In addition, the effect of Mn concentration on the site occupation of Mn ions in PZT lattice was investigated. The experiments were carried out at the station 7.1 EXAFS beam line of the synchrotron radiation source (SRS), Daresbury, U.K. For EXAFS experiments at station 7.1, X-rays were monochromatized by a Si (1 1 1) double crystal. The EXAFS spectrum was measured at the Mn K edge in the fluorescence mode due to a low concentration of Mn in the samples. The fluorescence detection system consists of an array of nine high-purity germanium diodes mounted in a common cryostat. To do fluorescence measurements, the sample was aligned at 45° to the line of the beam, in order to maximize the solid angle seen by the detector. The data analysis of all EXAFS measurements was carried out using the analysis programs; EXCALIB (the program developed by SRS) and FEFF7 [10].

# 3. Results and discussion

# 3.1. Phase investigation for Mn-Mg doped PZT ceramics

XRD patterns of Mn doped PZT and Mn–Mg doped PZT ceramics are shown in Figs. 1 and 2, respectively. The splitting of (1 1 1) and (1  $\bar{1}$  1) peaks at 38° 2 $\theta$ , as well as the presence of the  $\{0\ 2\ 0\}_R$  peak at  $2\theta$  of 43° indicates the presence of the rhombohedral phase. The production of rhombohedral PZT in this study was done to avoid the effect of Mn on the shift of MPB (morphotopic phase boundary) toward the rhombohedral phase region as reported by Kim and Yoon [2]. In this case, increasing Mn concentration merely stabilizes the rhombohedral phase rather than causing a change in structure from tetragonal to rhombohedral.

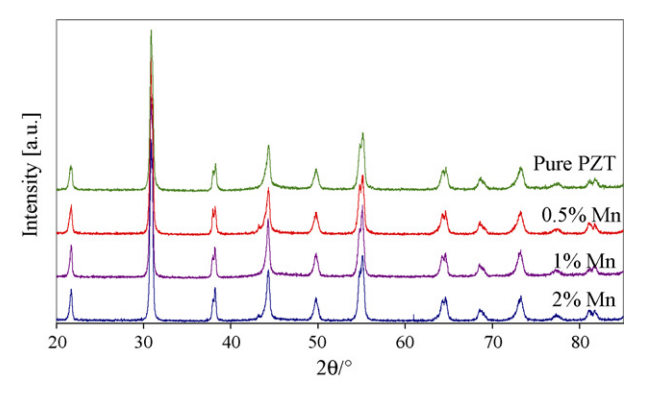


Fig. 1. XRD patterns of Mn doped PZT with the Zr/Ti = 56/44.

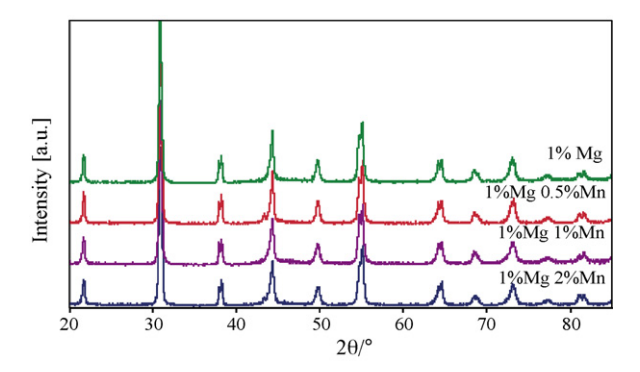


Fig. 2. XRD patterns of Mn-Mg doped PZT with the Zr/Ti = 56/44.

# 3.2. EXAFS study for Mn-Mg doped PZT ceramics

The data analysis of all EXAFS measurements was carried out using the analysis programs; EXCALIB and FEFF7. Figs. 3 and 4 show the Fourier transform for the EXAFS spectra of various Mn doped PZT samples with and without 1% of Mg.

The Fourier transform is a complex function of distance R, the amplitude of which is denoted by the real function  $\rho(R)$ . The

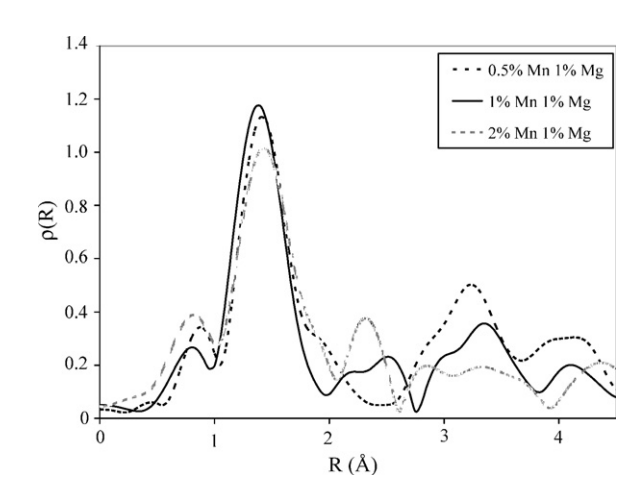


Fig. 3. Fourier transforms of the EXAFS spectra for Mn-Mg doped PZT ceramics.

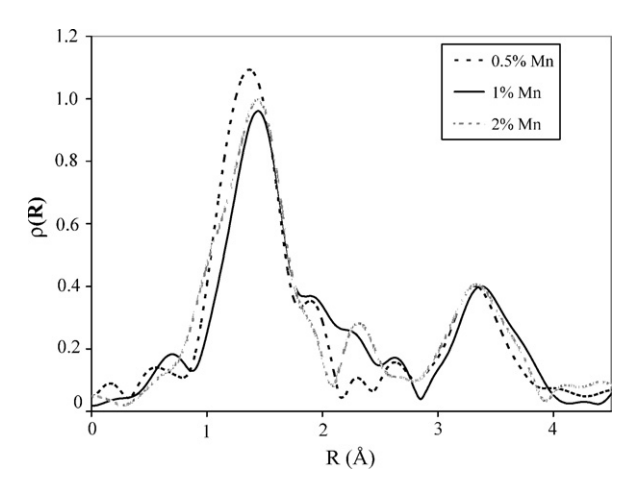


Fig. 4. Fourier transforms of the EXAFS spectra for Mn doped PZT ceramics.

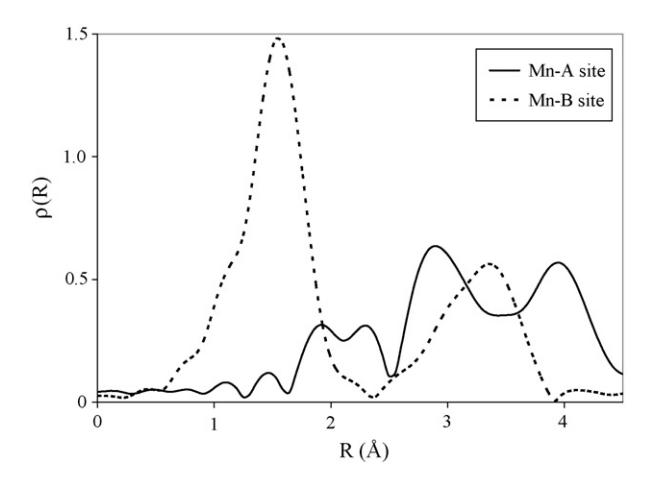


Fig. 5. Simulated EXAFS for rhombohe-dral PZT with Mn impurity in A(Pb)-site and B(Ti/Zr)-site.

position of peaks in  $\rho(R)$  is related to bond distances between the Mn ion and neighbouring ions while the height of each peak is proportional to the number of neighbours. However, the bond lengths and coordination numbers cannot be read directly from  $\rho(R)$ . In order to determine the bond lengths and coordination numbers, the k-dependent amplitude and phase corrections must be made to the EXAFS signal. For instance, prior to the phase correction, the peaks in  $\rho(R)$  are normally smaller than the corresponding bond lengths by 0.5 Å. However, the location of Mn within PZT unit cell can be resolved without making phase and amplitude corrections. By simply comparing the raw Fourier transform,  $\rho(R)$ , for different Mn concentrations, as shown in Figs. 3 and 4, there is no observable change in peak positions, particularly for the first main peak, with Mn concentration over the range of 0.5-2% for either the samples with or without Mg doping. Since the peak position indicates the bond distance between Mn and its neighbours or the location of Mn within the PZT unit cell, the coincidence of the main peaks as seen in Figs. 3 and 4 is evidence that no change in the location of the majority of Mn ions occurs with increasing Mn concentration. Furthermore, the location of Mn appears to be unaffected by the presence of 1% Mg.

In order to determine the preferred site occupation of Mn ions in PZT unit cell, the Fourier transform of EXAFS spectra for rhombohedral PZT with Mn ion occupying A(Pb) and B(Ti/Zr) sites were simulated, as shown in Fig. 5.

For the B-site curve, the first main peak occurring at roughly 1.5 Å is due to the six nearest oxygen atoms, while the second peak at 3.5 Å is attributed to the nearest Pb atoms. There is no significant feature at 1.5 Å for the A-site spectrum. This is the obvious distinction between A-site and B-site EXAFS. Comparing the results shown in Figs. 3 and 4, it is evident that the peaks are clearly incompatible with a simulation of EXAFS when Mn occupies the A(Pb)-site but are in good

qualitative agreement with a simulation that assumes Mn occupies the B(Ti/Zr)-site. However, the minority A-site occupation cannot be ruled out.

#### 4. Conclusions

The X-ray diffraction measurements for all PZT samples indicated the presence of rhombohedral phase.

EXAFS measurements and analysis indicated that Mn ions seemed to be a B-site favoured dopant in the PZT lattice, since the position of the highest peak of the Fourier transform of EXAFS spectra for all Mn–Mg doped PZT samples occurred in the region of 1.5 Å, corresponding to the simulated EXAFS for B-site substitution. The evidence for the A-site substitution was not obviously observed.

#### Acknowledgements

This work was supported by the National Synchrotron Research centre (NSRC), Thailand under contact No. 2548/001. The authors also thank the CCLRC SRS (Daresbury) Facility, UK, for providing access to the beamline and Dr. S Fiddy for technical support. SL is supported by the Thailand Research Fund under grant #BRG4880015.

#### References

- M.D. Glinchuk, I.P. Bykov, V.M. Kurliand, M. Boudys, T. Kala, K. Nejezchleb, Valency states and distribution of manganese ions in PZT ceramics simultaneously doped with Mn and Nb, Phys. Status Solidi A122 (1990) 341–346.
- [2] J.S. Kim, K.H. Yoon, Physical and electrical properties of MnO<sub>2</sub>-doped Pb(Zr<sub>x</sub>Ti<sub>1-x</sub>)O<sub>3</sub> ceramics, J. Mater. Sci. 29 (1994) 809–815.
- [3] L.X. He, C.E. Li, Effects of addition of MnO on piezoelectric properties of lead zirconate titanate, J. Mater. Sci. 35 (2000) 2477–2480.
- [4] A.P. Barranco, F.C. Piñar, P. Martínez, E.T. García, Effects of MnO<sub>2</sub> additives on the properties of PbZrO<sub>3</sub>–PbTiO<sub>3</sub>–PbCu<sub>1/4</sub>Nb<sub>3/4</sub>O<sub>3</sub> ferroelectric ceramic system, J. Eur. Ceram. Soc. 21 (2001) 523–529.
- [5] H. Du, S. Qu, J. Che, Z. Liu, X. Wei, Z. Pei, The effect of composition on microstructure and properties of PNW-PMS-PZT ceramics for highpower piezoelectric transformer, Mater. Sci. Eng. A 393 (2005) 36–41.
- [6] H. Du, Z. Pei, W. Zhou, F. Luo, S. Qu, Effect of addition of MnO<sub>2</sub> on piezoelectric properties of PNW–PMS–PZT ceramics, Mater. Sci. Eng. A 421 (2006) 286–289.
- [7] B. Cherdhirunkorn, D.A. Hall, Effects of Mn concentrations on the physical and electrical properties of rhombohedral Mg–Mn doped PZT ceramics, Chiang Mai J. Sci. 32 (3) (2005) 301–305.
- [8] M.C. Marco De Lucas, F. Rodríguez, C. Prieto, M. Verdaguer, H.U. Güdel, Local structure determination of Mn<sup>2+</sup> in the ABCl<sub>3</sub>:Mn<sup>2+</sup> chloroperovskites by EXAFS and optical spectroscopy, J. Phys. Chem. Solids 56 (1995) 995–1001.
- [9] I.W. Chen, P. Li, Y. Wang, Structural origin of relaxor perovskites, J. Phys. Chem. Solids 57 (1996) 1525–1536.
- [10] S.I. Zabinsky, J.J. Rehr, A. Ankudinov, R.C. Albers, M.J. Eller, Multiple-scattering calculations of X-ray-absorption spectra, Phys. Rev. B 52 (1995) 2995–3009.







Physica B 376-377 (2006) 686-689

www.elsevier.com/locate/physb

# Probing deactivations in Nitrogen doped ZnO by vibrational signatures: A first principles study

Sukit Limpijumnong<sup>a,b,\*</sup>, Xiaonan Li<sup>c</sup>, Su-Huai Wei<sup>c</sup>, S.B. Zhang<sup>c</sup>

<sup>a</sup>National Synchrotron Research Center, Nakhon Ratchasima, Thailand <sup>b</sup>School of Physics, Suranaree University of Technology, Nakhon Ratchasima, Thailand <sup>c</sup>National Renewable Energy Laboratory, Golden, CO, USA

#### Abstract

Based on first principles calculations, we investigate two probable types of deactivation mechanisms that hinder current efforts of doping ZnO p-type. (i) Passivation by Hydrogen. H prefers to bind with  $N_O$  at the anti-bonding site and form  $N_O$ -H complexes with a binding energy of about 1 eV. (ii) Passivation by the formation of substitutional diatomic molecules (SDM). Carbon impurities and excess N strongly prefer to passivate  $N_O$  and form low-energy SDM on the Oxygen site, (NC) $_O$  or (N2) $_O$ , both of which are donors with several-eV binding energies. Our calculated vibrational frequencies of  $N_O$ -H complexes and SDMs are consistent with the frequencies recently observed by IR measurement on N-doped ZnO, which is not p-type.

© 2005 Elsevier B.V. All rights reserved.

PACS: 61.72.Bb; 61.72.Vv; 63.20.Pw; 78.30.Fs

Keywords: Zno; First principles; Vibrational frequency; Wide band gap

# 1. Introduction

Recent SIMs results on nitrogen-doped ZnO grown by chemical vapor deposition technique show a substantial amount of H, C and N in unwanted forms [1–4]. These impurities are likely to play important roles in compensating or passivating N acceptors, making it difficult to dope ZnO p-type. Recent IR measurements on N-doped ZnO, which is not p-type, revealed several peaks associated with H, including a peak at 3020 cm<sup>-1</sup> which is consistent with the N–H stretch vibration frequency. In addition, the spectrum in the lower frequency range contains several peaks in the range of 1800–2000 cm<sup>-1</sup>, which are close to the frequencies of diatomic molecules.

E-mail address: sukit@sut.ac.th (S. Limpijumnong).

Based on first principles calculations, we found two types of defect complexes that are likely to form. While isolated H is predicted to exclusively be a donor in ZnO [5,6], it can also passivate N<sub>O</sub> acceptors and form an electrically inactive N<sub>O</sub>-H complex (Fig. 1) [3]. For the second type of complex, C impurities and excess N atoms prefer to passivate N<sub>O</sub> acceptors and form a "substitutional diatomic molecule" (SDM), which is a strongly bound NC or N<sub>2</sub> molecule substituted on an oxygen site [(NC)<sub>O</sub> or (N<sub>2</sub>)<sub>O</sub>] (Fig. 2) [7,8]. The (NC)<sub>O</sub> or (N<sub>2</sub>)<sub>O</sub> SDMs are single and double donors, respectively. These SDMs have electronic and structural properties similar to free diatomic molecules. The calculated local vibrational modes (LVM) of these defects are in good agreement with the peaks recently observed by FTIR measurement on N-doped ZnO. These results suggest that, in addition to H, one should be careful with a C impurity that can turn an existing N acceptor (No) into an (NC)o SDM, which is a donor. In addition, excessive N incorporation could lead to an unwanted (N<sub>2</sub>)<sub>O</sub> SDM, which is a double donor, instead of the desired No.

<sup>\*</sup>Corresponding author. School of Physics, Suranaree University of Technology, Nakhon Ratchasima 30000, Thailand. Tel.: +6644224319; fax: +6644224185.

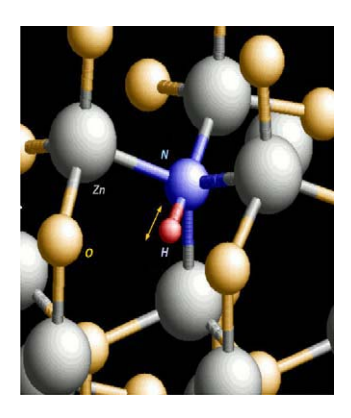


Fig. 1. Atomic structure of the  $N_0$ -H complex. Large sphere is Zn and small sphere is O. Impurities N and H are labeled.

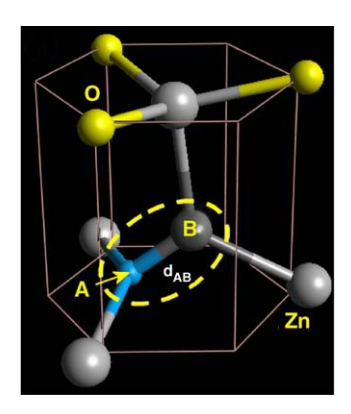


Fig. 2. Atomic structure of the substitutional diatomic molecule, where the encircled AB dimer replaces an O atom in ZnO. For  $(N_2)_O$  SDM, A = B = N. For  $(NC)_O$  SDM, A = N and B = C. The large sphere is Zn and the small sphere is O.

# 2. Theoretical approach

# 2.1. Total-energy and formation energy calculations

Our first principles calculations are based on the pseudopotential planewave method with density-functional theory in the local-density approximation. The Vanderbilt-type ultra-soft pseudopotential [9], as implemented in the VASP codes [10], is used. The use of ultrasoft versions of the pseudopotentials allows relatively low energy cutoffs (300 eV) to be used for the planewave basis set. The Zn 3d electrons are treated as valence electrons. The calculated heat of formation for ZnO of 3.58 eV agrees with the experimental value of 3.60 eV.

To study defects, we use a supercell approach with a supercell containing at least 36 atoms. Test calculations for the  $(N_2)_O$  and  $N_O$ –H complexes are performed with a larger 96-atom cell to ensure that the convergence is within  $\pm 0.2\,\mathrm{eV}$ . For charged defects, a jellium background was used. Since LDA substantially underestimates the ZnO band gap, we have instead examined the electronic properties at the  $2\times2\times2$  Monkhorst-Pack special k

points, which are also used for the Brillouin zone integration. The band gap at the special k points is 2.5 eV. All atoms in the cell are allowed to relax until the magnitude of the residue force on each atom is  $<0.05\,\mathrm{eV/Å}$ . The defect formation energy  $(\Delta H_\mathrm{f})$  which has been described in detail elsewhere (for example, Refs. [11,12]), can be defined as

$$\Delta H_{\rm f} = E_{\rm tot}(D, q) - E_{\rm tot}(0) + \Delta n_{\rm Zn} \mu_{\rm Zn} + \Delta n_{\rm O} \mu_{\rm O}$$
$$+ \Delta n_{\rm X} \mu_{\rm X} + q E_{\rm F}, \tag{1}$$

where  $E_{\text{tot}}(D,q)$  and  $E_{\text{tot}}(0)$  are the total energies from first principles calculations of the supercell with and without the defect, D, and X = H, N, C represents impurity elements. Quantities  $\Delta n_A$  and  $\mu_A$  are the number of species A (=Zn, O, H, N, C) removed from a defect-free cell to its respective reservoir to form the defect cell and the corresponding reservoir chemical potential. The chemical potentials  $\mu_{Zn}$ ,  $\mu_{\rm O}$ ,  $\mu_{\rm H}$ ,  $\mu_{\rm N}$  and  $\mu_{\rm C}$  have upper limits at their respective natural phases, i.e. the energies of metallic Zn, gaseous  $O_2$ , H<sub>2</sub>, N<sub>2</sub> and solid-state C, which are offset to zero in the present study. To keep the ZnO thermodynamically stable, it is also required that  $\mu_{\rm Zn} + \mu_{\rm O} = \mu_{\rm ZnO,calc} = -3.58$  eV. This imposes an additional constraint that  $\mu_{\rm O}$  be in the range  $-3.58 \text{ eV} \le \mu_{\text{O}} \le 0$  and redefines  $\mu_{\text{Zn}} = -3.58 \text{ eV} - \mu_{\text{O}}$ . Unless noted otherwise, all calculations in this paper are done in the Zn-rich limit, i.e.  $\mu_{\rm Zn}=0$ . In Eq. (1), q and  $E_{\rm F}$  are the defect charge state and Fermi level with respect to the VBM.

# 2.2. Vibration frequency calculations

We use the so-called frozen phonon calculation approach. After the defect is relaxed to the lowest energy configuration, we dislocate the vibrating atom (for example H atom in the N–H LVM case) along the vibrating direction in a small step at a time (typical step is 0.05 Å). For each step, the calculated total energy is recorded. The potential energy curve is constructed from the plot of total energy versus the vibrating distance.

In the case of  $N_O$ –H complex, it is a good approximation to dislocate only the H atom to construct the potential energy curve. This is because H is much lighter than other atoms. However, when calculating the N–H stretch frequency the reduced mass of N and H atoms must be used. Due to its light mass, the H atom vibrates with a large amplitude, i.e.  $\sim 10\%$  of the bond distance in the ground state and 20% in the first excited state. Therefore, it is important to include anharmonic effects in the LVM calculation [13,14].

In the case of SDMs, the situation is somewhat different. N and C have a comparable mass that is over ten times heavier than H, leading to a much smaller zero-point vibration amplitude. Since the amplitude of the vibration is small, the anharmonicity in N–C and N–N vibrations are much smaller than that of the H–N vibration. For example, including anharmonicity in the calculation only leads to a

change in the LVM of a free  $N_2$  molecule by  $<20 \,\mathrm{cm}^{-1}$  out of a total frequency of about  $2000 \,\mathrm{cm}^{-1}$  [14]. In calculating the LVM of SDMs, both atoms in the dimer are simultaneously dislocated with the same amplitude in opposite directions. Other atoms in the supercell are fixed.

#### 3. Results and discussions

# 3.1. Passivation by hydrogen

Using the definition of the formation energy given above, we calculated the formation energies of an isolated interstitial H, a nitrogen acceptor No, and a No-H complex in ZnO. An isolated interstitial H is exclusively a donor in ZnO and always exists in the form of H<sup>+</sup>. For an isolated H<sup>+</sup> location, there are four low-energy sites surrounding an O atom with the so-called BC<sub>||</sub> site being the site with the lowest energy [6,15]. The other three sites have slightly higher energies (approximately within 0.2 eV). An isolated No is an acceptor. Currently the exact location of the ionization energy of No is still under debate [3]. Over almost the entire Fermi energy range, the isolated  $N_0$  is stable in a (1-)-charge state whereas an isolated interstitial H atom is always stable in a (1+)-charge state. The two defects, therefore, have a Coulomb attraction and have a strong tendency to form a N<sub>O</sub>-H defect complex. The formation energy of H<sup>+</sup> (at BC<sub>||</sub> site) and N<sub>O</sub> are plotted (dashed lines) as a function of Fermi level in Fig. 3 with the sum of the two formation energies shown as dotted lines. In the same figure, we also plot the formation energy of the N<sub>O</sub>-H complex (thick solid line). The binding energy of the N<sub>O</sub>-H complex is 0.95 eV, i.e. the difference in energy between the dotted and solid line. For the N<sub>O</sub>-H defect complex, the  $AB_{N\perp}$  configuration (Fig. 1) has the lowest

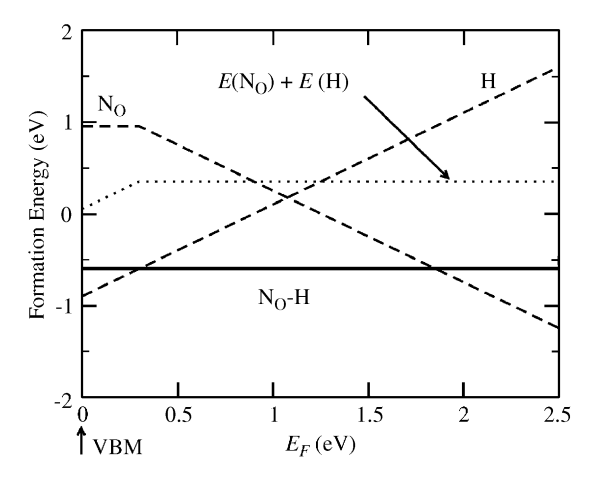


Fig. 3. Formation energy of an interstitial H,  $N_O$  (dashed lines) and a  $N_O$ –H complex (solid line) in ZnO as a function of electron Fermi energy. The dotted line shows the sum of the formation energies of an isolated interstitial hydrogen and an isolated  $N_O$ . The Zn-rich condition,  $N_2$  and  $H_2$  phase precipitation limits were assumed. The energy difference between the dotted line and the solid line is the binding energy of the  $N_O$ –H complex.

formation energy. The AB<sub>N</sub> configurations are energetically more stable than the BC by about 0.2-0.3 eV, making the likelihood of forming BC configurations negligible. The difference in formation energy between the two AB<sub>N</sub> configurations is within the computational error bar. Both AB<sub>N</sub> configurations have a similar N-H stretch mode frequency, with an average value of 2927 cm<sup>-1</sup>. The anharmonic contributions are rather large, i.e. approximately 8%. Both BC configurations also have a similar N-H stretch mode frequency, with an average value of  $3319 \,\mathrm{cm}^{-1}$ , which is clearly higher than those of the AB<sub>N</sub> configurations. The anharmonic contributions are less than half of those for the AB<sub>N</sub> cases. The smaller anharmonic contribution in BC in comparison with AB<sub>N</sub> agrees with the usual trend found for an isolated H in ZnO [6] as well as in the GaN system [13]. To estimate the systematic error of our calculation, we calculated the known stretch-mode frequency of a free ammonia (NH<sub>3</sub>) molecule. We obtained the symmetric stretch LVM of 3194 cm<sup>-1</sup> which is 143 cm<sup>-1</sup> smaller than the known experimental value (3337 cm<sup>-1</sup>). Assuming that our calculated LVM of the N-H bond in ZnO is underestimated by similar amount, our adjusted value for AB<sub>N</sub> of  $2927 + 143 = 3070 \,\mathrm{cm}^{-1}$  is in reasonable agreement with the recently observed peak at  $3020\,\mathrm{cm}^{-1}$  [3].

# 3.2. Passivation by the formation of substitutional diatomic molecules

The diatomic molecule is one of the most common forms for first row elements, namely, C, N, and O, because these small atoms tend to form strong triple bonds with each other. Recently, similar complexes, such as  $N_2$  and NC inclusions in GaAs have been studied both theoretically and experimentally [16,17]. In the case of ZnO, the  $(N_2)_O$  and  $(NC)_O$  SDM are found to have bonding and antibonding characteristics very similar to their free molecules confirmed by the detailed investigation of the electronic wavefunctions [7,8]. Here, we will focus only on the energetic and the LVM of the complexes.

Fig. 4 shows the  $E_{\rm F}$  dependence of the formation energy  $(\Delta H_{\rm f})$  in the Zn-rich, N-rich, and C-rich conditions  $(\mu_{Zn} = \mu_N = \mu_C = 0)$  for  $(CO)_O$ ,  $(NC)_O$ ,  $(NO)_O$ , and  $(N_2)_O$ . Since the isolated interstitials N<sub>i</sub> and C<sub>i</sub> have very high formation energies, they tend to immediately bind with the closest lattice O, forming (NO)<sub>O</sub> and (CO)<sub>O</sub>. However, in the presence of N<sub>O</sub>, (NO)<sub>O</sub> and (CO)<sub>O</sub> are unstable against the formation of (N<sub>2</sub>)<sub>O</sub> and (NC)<sub>O</sub>. The binding energies are typically several eV due in part to Coulomb attraction between oppositely charged impurities and in part to the combination of two impurities into one. This can significantly reduce the formation energy because, for example, when  $N_O + (NO)_O \rightarrow (N_2)_O + O_O$ , one less oxygen site is disturbed by the impurities after the reaction. In the right panel of Fig. 4, the formation energy of No and (NO)<sub>O</sub> are shown as the dashed line and the thin solid line with the sum of the two as the dotted line. The sum is to be

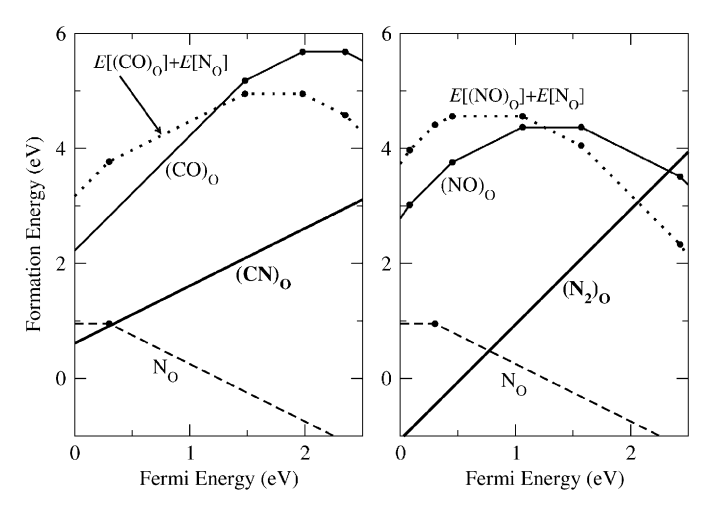


Fig. 4. Formation of (left panel)  $(NC)_O$  from isolated  $N_O$  and  $(CO)_O$  and (right panel)  $(N_2)_O$  from  $N_O$  and  $(NO)_O$ . The Zn-rich condition,  $N_2$  and diamond phase precipitation limits were assumed.

compared with the thick solid line, which is the formation energy of  $(N_2)_O$  defect. We can immediately see that the binding energy, which is the difference between the dotted line and the thick solid line, depends somewhat on the Fermi energy, but has a typical value of several eV. The binding energy is of similar magnitude for the case of  $(NC)_O$ , as shown in the left panel. This is especially true in the case of p-type ZnO, for which the binding energies are large enough to make both  $(N_2)_O$  and  $(NC)_O$  lower in energy than isolated  $N_O$ . It is therefore expected that the formation of  $(N_2)_O$  and  $(NC)_O$  will compete with the formation of  $N_O$  acceptors. Since these SDMs are donors in p-type samples, their formation further hinders p-type doping by compensating the already lowered  $N_O$  acceptors.

The situation could be worse when one tries to increase N concentration, [N], above the equilibrium value via non-equilibrium growth methods. Effectively, this is similar to increasing the nitrogen chemical potential  $\mu_N$ . Although the formation energy of  $N_O$  decreases as one raises  $\mu_N$ , the formation energy of the  $(N_2)_O$  complex decreases twice as fast. In thermal equilibrium, this would end up increasing the concentration of the donor  $(N_2)_O$  complex instead of the acceptor  $N_O$ . However, because the formation of  $(N_2)_O$  from  $N_O + (NO)_O$  involves the breakup of one SDM, the diffusion of  $N_i$ , and the formation of another SDM, one might be able to adjust the growth temperature to be low enough that  $(N_2)_O$  is suppressed.

The calculated frequencies for  $(N_2)_O^{-1}$  and  $(NC)_O^+$ , which are the most stable form for these complexes in p-type ZnO, are 2108 and 1995 cm<sup>-1</sup>, respectively. These frequencies fall within  $200 \, \text{cm}^{-1}$  of the experimentally observed values [2]. Moreover, recent XPS experiments have found strong signals of N-N and C-N bonds with similar characteristics to those of free diatomic molecules [4]. These observations strongly suggest the existence of  $(N_2)_O$  and  $(NC)_O$  in these samples.

#### 4. Conclusion

First principles total energy calculations show that H, C, and N can passivate  $N_O$  acceptors in ZnO. H can passivate  $N_O$  and form  $N_O$ –H complexes with the binding energy of approximately 1 eV. C and excess N can passivate  $N_O$  and form low energy (NC) $_O$  and ( $N_2$ ) $_O$  substitutional diatomic molecules (SDM) on the oxygen site in ZnO. The calculated vibrational frequencies are in qualitative agreement with recent IR experiments. Our calculations also show that both (NC) $_O$  and ( $N_2$ ) $_O$  are donors in p-type ZnO. These results should shed new light on efforts to improve the fabrication of high quality p-type ZnO by nitrogen.

# Acknowledgements

This work was supported by AFOSR/AOARD under Contract No. FA5209-05-P-0309 and by the Thailand Research Fund under Contract No. BRG4880015. The work at NREL was supported by the US DOE/BES and DOE/EERE under contract No. DE-AC36-99GO10337. The authors thank T.J. Coutts, B.M. Keyes, and C.L. Perkins for helpful discussions and M.F. Smith for proofreading the manuscript.

# References

- S.J. Pearton, D.P. Norton, K. Ip, Y.W. Heo, T. Steiner, J. Vac. Sci. Technol. B 22 (2004) 932.
- [2] B.M. Keyes, L.M. Gedvilas, X. Li, T.J. Coutts, J. Cryst. Growth 281 (2005) 297.
- [3] X. Li, B.M. Keyes, S.E. Asher, S.B. Zhang, S.-H. Wei, T.J. Coutts, S. Limpijumnong, C.G. Van de Walle, Appl. Phys. Lett. 86 (2005) 122107.
- [4] C.L. Perkins, S.-H. Lee, X. Li, S.E. Asher, T.J. Coutts, J. Appl. Phys. 97 (2005) 034907.
- [5] C.G. Van de Walle, Phys. Rev. Lett. 85 (2000) 1012.
- [6] S. Limpijumnong, S.B. Zhang, Appl. Phys. Lett. 86 (2005) 151910.
- [7] S. Limpijumnong, X. Li, S.-H. Wei, S.B. Zhang, Appl. Phys. Lett. 86 (2005) 211910.
- [8] E.-C. Lee, Y.-S. Kim, Y.-G. Jin, K.J. Chang, Phys. Rev. B 64 (2001) 085120.
- [9] D. Vanderbilt, Phys. Rev. B 41 (1990) 7892.
- [10] G. Kresse, J. Furthmüller, Comput. Mater. Sci. 6 (1996) 15.
- [11] S.B. Zhang, J.E. Northrup, Phys. Rev. Lett. 67 (1991) 2339.
- [12] C.G. Van de Walle, S. Limpijumnong, J. Neugebauer, Phys. Rev. B 63 (2001) 245205
- [13] S. Limpijumnong, J.E. Northrup, C.G. Van de Walle, Phys. Rev. B 68 (2003) 075206.
- [14] S. Limpijumnong, in: N.H. Nickel, M.D. McCluskey, S.B. Zhang (Eds.), Hydrogen in Semiconductors, MRS Symp. Proc. No. 813, Materials Research Society, Pittsburgh, 2004, p. H3.6.
- [15] E.V. Lavrov, J. Weber, F. Börrnert, C.G. Van de Walle, R. Helbig, Phys. Rev. B 66 (2002) 165205.
- [16] W. Ulrici, B. Clerjaud, Phys. Rev. B 72 (2005) 045203.
- [17] P. Carrier, S.-H. Wei, S.B. Zhang, S. Kurtz, Phys. Rev. B 71 (2005) 165212.

# Author's personal copy



Available online at www.sciencedirect.com



MECHANICS
RESEARCH COMMUNICATIONS

Mechanics Research Communications 35 (2008) 73-80

www.elsevier.com/locate/mechrescom

# Effect of load triaxiality on polymorphic transitions in zinc oxide

A.J. Kulkarni <sup>a</sup>, K. Sarasamak <sup>b</sup>, J. Wang <sup>c</sup>, F.J. Ke <sup>c,d</sup>, S. Limpijumnong <sup>b</sup>, M. Zhou <sup>a,\*</sup>

> Received 31 August 2007 Available online 21 September 2007

# **Abstract**

Molecular dynamics (MD) simulations and first-principles calculations are carried out to analyze the stability of both newly discovered and previously known phases of ZnO under loading of various triaxialities. The analysis focuses on a graphite-like phase (HX) and a body-centered-tetragonal phase (BCT-4) that were observed recently in  $[01\bar{1}0]$ - and [0001]-oriented nanowires respectively under uniaxial tensile loading as well as the natural state of wurtzite (WZ) and the rocksalt (RS) phase which exists under hydrostatic pressure loading. Equilibrium critical stresses for the transformations are obtained. The WZ  $\rightarrow$  HX transformation is found to be energetically favorable above a critical tensile stress of 10 GPa in  $[01\bar{1}0]$  nanowires. The BCT-4 phase can be stabilized at tensile stresses above 7 GPa in [0001] nanowires. The RS phase is stable at hydrostatic pressures above 8.2 GPa. The identification and characterization of these phase transformations reveal a more extensive polymorphism of ZnO than previously known. A crystalline structure—load triaxiality map is developed to summarize the new understanding.

© 2007 Elsevier Ltd. All rights reserved.

Keywords: Phase transformations; Load triaxiality; Zinc oxide; Molecular dynamics; Density functional theory

# 1. Introduction

Polymorphic transitions occur in materials with non-convex free energy landscapes or materials that display multiple local minima along with a global minimum under ambient conditions. The global minimum in free energy corresponds to a stable crystalline structure and is the natural state of the material. Each local minimum, on the other hand, represents a metastable lattice structure that the material can assume under external stimuli. Traditionally, external loading and temperature changes are used to transform materials from their stable structures to metastable states. Stress-induced phase transformations are widely observed in

<sup>\*</sup> Corresponding author. Tel.: +1 404 894 3294; fax: +1 404 894 0186. E-mail address: min.zhou@gatech.edu (M. Zhou).

groups IV, III–V and II–VI materials including ZnO, which have been predominantly studied through compressive loading (Mujica et al., 2003). Having a parent wurtzite (WZ,  $P6_3mc$  space group) structure, these materials transform to a rocksalt (RS,  $Fm\bar{3}m$  space group) structure under high hydrostatic pressures. The recent fabrication of defect-free, single-crystalline nanowires, nanobelts and nanorings of ZnO (IIB–VIA), GaN (IIIA–VA) and CdSe (IIB–VIA) necessitates the analyses of responses to loading of various triaxialities, including bending and uniaxial tension since these materials have slender quasi one-dimensional geometries and are capable of undergoing significant elongations (Diao et al., 2004; Kulkarni et al., 2005; Liang and Zhou, 2006).

There are three hitherto known polymorphs of ZnO, including WZ, RS and zinc blende (ZB,  $F\bar{4}3m$ ) (Ozgur et al., 2005). WZ is the natural state under ambient conditions. RS occurs under high hydrostatic pressures. ZB can only be grown on certain crystalline surfaces of cubic crystals. So far, the existence of polymorphs other than WZ, ZB and RS at various loading triaxialities has not been extensively studied. Recently, we observed a graphitic structure (hereafter referred to as HX) in  $[01\bar{1}0]$ -orientated nanowires (Kulkarni et al., 2006) and a body-centered-tetragonal phase (hereafter referred to as BCT-4) in [0001]-oriented nanowires under uniaxial tensile loading (Wang et al., accepted for publication). Here, we characterize the phase transformations from WZ that lead to these novel structures. For comparison and overall perspective, the WZ-to-RS transformation is also analyzed. Our analyses use first-principles calculations based on the density functional theory (DFT) and molecular dynamics (MD) simulations. Particular interest is on the crystallographic changes and critical loading condition for each transformation. A crystalline structure–load triaxiality map is developed to summarize the relationship between the structures and load condition.

# 2. Computational framework

The MD simulations use the Buckingham potential with charge interactions (Binks and Grimes, 1993; Wolf et al., 1999). The calculations concern the quasi-static uniaxial tension of nanowires with the  $[01\bar{1}0]$  growth orientation and nanorods with the [0001] growth orientation and the hydrostatic compression of bulk ZnO. The initial structures considered are single-crystalline and wurtzite-structured with lattice constants a=3.249 Å and c=5.206 Å, as illustrated in Fig. 1(a) (Wang, 2004). The computational cell for bulk structure is  $29.24\times28.13\times31.24$  Å in size and is created by repeating a unit wurtzite cell along the [0001],  $[01\bar{1}0]$  and  $[2\bar{1}\bar{1}0]$  directions. Periodic boundary conditions (PBCs) are specified along the three directions to approximate infinite material extension. The  $[01\bar{1}0]$ -oriented nanowires have rectangular cross-sections and  $\{2\bar{1}\bar{1}0\}$  and  $\{0001\}$  lateral surfaces and the computational cell size is  $21.22\times18.95\times150.83$  Å. The [0001]-oriented nanorods have hexagonal cross-sections with a six-fold symmetry around the [0001] axis and six  $\{01\bar{1}0\}$  lateral surfaces. The corresponding computational cell size is  $28.14\times65.0\times145.8$  Å. PBCs are specified only along the axial directions for the nanowires.

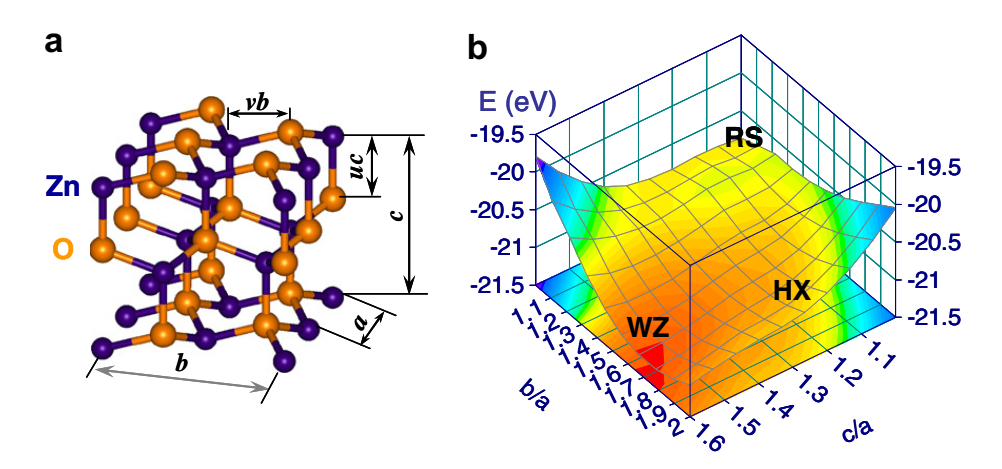


Fig. 1. (a) The wurtzite (WZ) crystal structure and (b) formation energy surface of ZnO with minima corresponding to the WZ, HX and RS structures.

Since the crystallographically constructed computational cells may not be in equilibrium, pre-loading relaxations are carried out to obtain their free standing configurations. Following this initial equilibration, approximate quasi-static tensile loading in each deformation increment is achieved though successive loading (at a specified rate of 0.005/ps) and equilibration steps (for 3 ps) using a combination of algorithms for NPT (Melchionna et al., 1993; Spearot et al., 2005) and NVE ensembles (Haile, 1997). The loading process results in a longitudinal strain increment of 0.25% (dilatation increment of  $\sim 0.75\%$ ) per deformation increment. Unloading is implemented in a similar manner with a reduction in strain for each unloading step. The virial formula is used to calculate the stress (Zhou, 2003).

The DFT calculations use the VASP code (Kresse and Furthmüller, 1996) with local density approximation (LDA) and ultrasoft pseudopotentials (Vanderbilt, 1990) and focus on the evaluation of the total energy in the natural and deformed states. The stability of each crystal structure is determined by analyzing enthalpy as a function of lattice parameter ratios *cla* and *bla*. The enthalpy per unit cell (2 Zn–O pairs) under uniaxial loading is defined as

$$H(c/a, b/a) = E(c, b, a, u, v) - \frac{1}{2} f_i q_i, \tag{1}$$

where E is the formation energy,  $f_i$  is the uniaxial force along the i direction,  $q_i$  is the lattice parameter in the i direction, and  $f_iq_i$  (summation not implied) is external work per unit volume V. For tension along the  $[01\overline{1}0]$  axis, i = b,  $f_b = \sigma_b \times (ac)$  and  $q_b = b$ , with  $\sigma_b$  being the tensile stress. For tension along the c axis, i = c,  $f_c = \sigma_c \times (ab)$ , and  $q_c = c$ , with  $\sigma_c$  being the tensile stress. For hydrostatic compression, the enthalpy is

$$H(c/a, b/a) = E(c, b, a, u, v) + \frac{1}{2}pV,$$
 (2)

where p is the pressure and V = abc is the volume of two unit cells containing 4 Zn–O pairs. For each c/a and b/a pair, the internal parameters u and v and the volume V are allowed to relax so that the configuration that yields minimum H is obtained. For a given load condition, the minima on the enthalpy surface with c/a and b/a as the independent variables identify the corresponding stable and metastable structures.

# 3. Results and discussion

# 3.1. Stress-free state

Under ambient conditions, ZnO assumes the WZ structure which belongs to the  $P6_3mc$  space group. As shown in Fig. 1a, this structure consists of two hexagonal close packed sublattices (one for Zn and the other for O) with an offset of 'uc' along the [0001] axis. The lattice parameters a, b, c, u = uc/c, v = vb/b which completely define the structure are also indicated in the figure. Fig. 1b shows the formation energy (or enthalpy at zero external loading) landscape for ZnO. The structures corresponding to WZ, RS and HX are shown. The global minimum occurs at the WZ structure with (c/a, b/a) = (1.61, 1.73). Clearly, WZ is the most stable structure with the lowest energy; HX and RS have higher energies and are not stable under ambient conditions.

# 3.2. Uniaxial tension along the $[01\overline{1}0]$ orientation

Fig. 2a shows an intermediate configuration during the tensile loading of a  $[01\bar{1}0]$ -oriented nanowire with the cross-sectional size of  $21.22 \times 18.95$  Å using MD simulations. The corresponding stress-strain ( $\sigma$ - $\varepsilon$ ) response is shown in Fig. 2b. The region between A and B corresponds to elastic stretching of the WZ structure. Loading beyond B results in a stress drop from 10.02 to 6.98 GPa (B  $\rightarrow$  C) at  $\varepsilon$  = 5.14%. This softening behavior corresponds to the nucleation of the HX phase. At this stage, u changes from its initial value of 0.38 for WZ to a value of 0.5 for HX, implying the flattening of the buckled wurtzite basal plane (Zn and O atoms becoming co-planar) [Fig. 2c]. As a result, Zn atoms are at equal distances from O atoms along the [0001] axis and the structure acquires the additional symmetry of a mirror plane perpendicular to the [0001] axis. This process occurs while the orientation of the basal plane remains invariant. Since v remains unchanged, HX has the same hexagonal symmetry around the c-axis as WZ. As the deformation progresses, the transformed

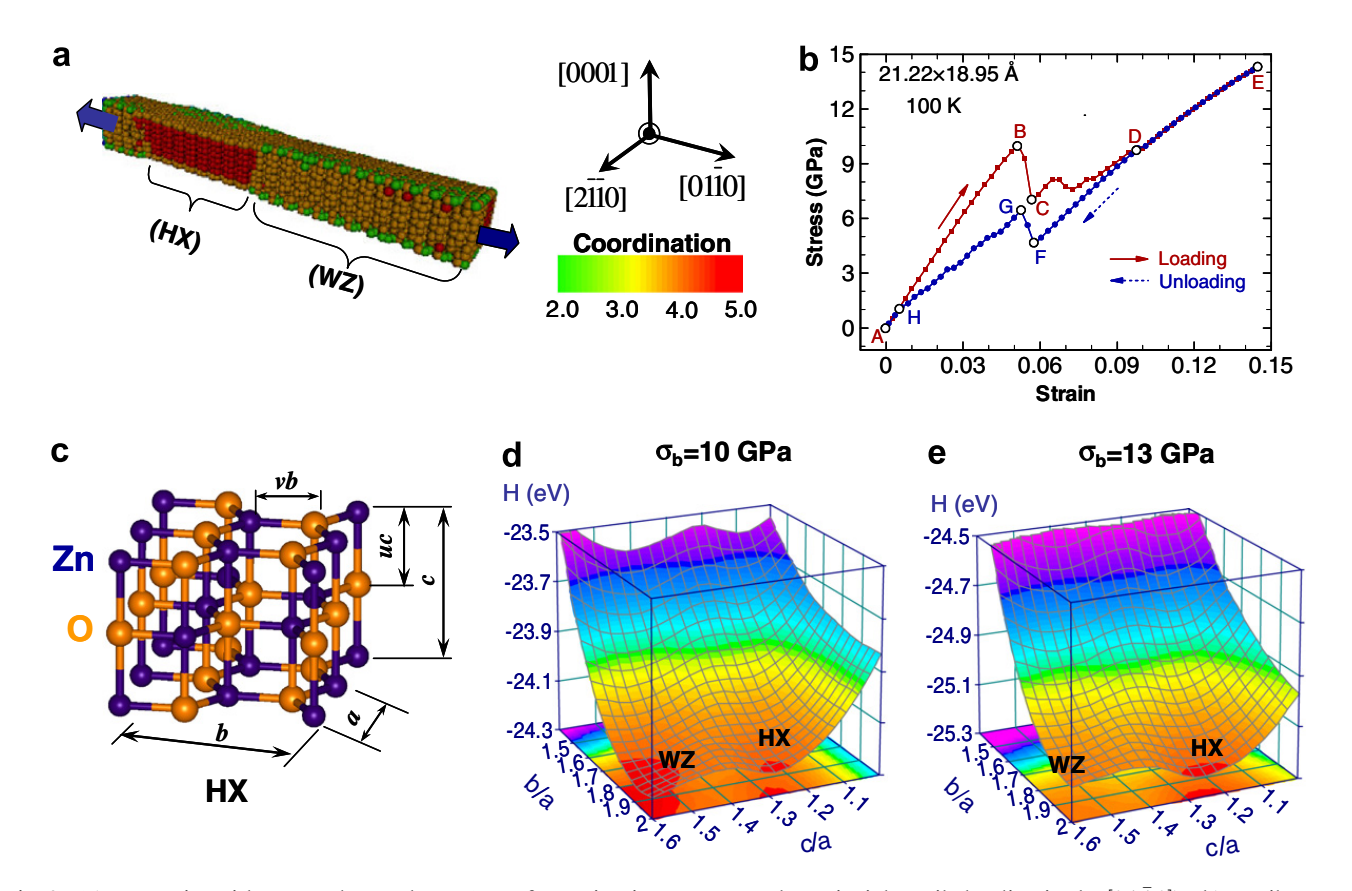


Fig. 2. (a) Nanowire with HX and WZ phases (transformation in progress under uniaxial tensile loading in the  $[0\,1\,\bar{1}\,0]$ ), (b) tensile stress–strain response of a  $21.22 \times 18.95$  Å nanowire at 100 K during loading–unloading, (c) newly discovered hexagonal (HX) crystal structure, (d) enthalpy surface map obtained from DFT calculations with tensile stress  $\sigma_b = 10$  GPa, and (e) enthalpy surface map with tensile stress  $\sigma_b = 13$  GPa.

region sweeps through the entire wire length  $(C \to D)$  and the transformation completes at  $\varepsilon = 9.71\%$  ( $\sigma = 9.65$  GPa). Further deformation occurs through the elastic stretching of the transformed structure (HX) and ultimate fracture occurs at  $\varepsilon = 16\%$  ( $\sigma = 15.29$  GPa, not shown) through cleavage along  $\{\bar{1}2\bar{1}0\}$  planes.

Unloading from any strain prior to the initiation of failure, e.g. point E with  $\varepsilon = 14.5\%$ , is first associated with the recovery of the elastic deformation within the HX structure (E  $\rightarrow$  F). A reverse transformation from HX to WZ (F  $\rightarrow$  G  $\rightarrow$  H) initiates at  $\varepsilon = 5.77\%$  ( $\sigma = 4.59$  GPa, point F) and completes at  $\varepsilon = 0.6\%$  ( $\sigma = 1.15$  GPa, point H). Unloading beyond H occurs through elastic deformation within the WZ structure (H  $\rightarrow$  A). Strains up to 14.5% can be recovered, highlighting a very unusual aspect of the behavior of ZnO which normally is quite brittle. Obviously, the large recoverable strains observed here are associated with the unique structural transformation process. The energy dissipation associated with the stress–strain hysteresis loop is  $\sim$ 0.16 GJ/m³, much lower than that for the WZ  $\leftrightarrow$  RS transformation in bulk ( $\sim$ 1.38 GJ/m³ with a maximum recoverable volumetric strain of 17% in compression) (Desgreniers, 1998).

Fig. 2d and e shows the enthalpy surfaces (eV/unit cell) for  $\sigma_b = 10$  and 13 GPa, respectively. In each case, there are two minima. The first minimum  $(H_{\min}^{WZ})$  is in the vicinity of  $c/a \approx 1.6$  and  $b/a \approx 1.9$  corresponding to a WZ structure with lattice parameters slightly different from those at zero stress. The second minimum  $(H_{\min}^{HX})$  in the vicinity of  $c/a \approx 1.3$  and  $b/a \approx 1.9$  corresponds to the HX phase. At a stress value of 10 GPa,  $H_{\min}^{HX}$  and  $H_{\min}^{WZ}$  are comparable and consequently both WZ and HX are equally favored. At an applied stress of 13 GPa [Fig. 3e],  $H_{\min}^{HX}$  is lower than  $H_{\min}^{WZ}$ , indicating that HX is more stable. Obviously, the critical stress value for the WZ-to-HX transformation is  $\sigma_b \approx 10$  GPa. As the magnitude of  $\sigma_b$  is increased above this equilibrium transition value, HX becomes more stable and simultaneously the transformation barrier is even lower, resulting in an increased driving force for transformation.

# 3.3. Uniaxial tension along the [0001] orientation

Fig. 3a shows the configuration of a [0001]-oriented nanorod with a lateral dimension of  $d = 32.5 \,\text{Å}$ . Fig. 3b shows the corresponding stress–strain response. Four distinct stages  $(A \to B, B \to C, C \to D)$  and  $D \to E$ ) are observed. The first stage (A  $\to$  B) corresponds to the elastic stretching of the WZ structure up to a strain of 7.5%. Further deformation results in a precipitous stress drop (B  $\rightarrow$  C) associated with the WZ to BCT-4 phase transformation which initiates in a local zone and propagates along the length of the nanorod. Crystallographic analysis reveals that the transformed phase consists of four-atom (2 Zn and 2 O) rings arranged in a BCT lattice [Fig. 3c]. The four-atom ring at the center has an orientation different (rotated by 90°) from that of the rings at the corners of the tetragonal lattice cell. The BCT-4 structure thus obtained preserves the initial tetrahedral coordination such that each Zn/O atom is at the center and four O/Zn atoms are at the vertices of a distorted tetrahedron. The distortion in the coordination tetrahedron can be analyzed through a quantification of the 3-D O–Zn–O bond angles ( $\alpha_i$ , i = 1..6). For WZ, the bond angles are approximately equal ( $\alpha_i \approx 108^\circ$ ). For BCT-4, the formation of 4-atom rings results in three distinct groups of bond angles ( $\alpha_1 \approx 90^\circ$ ,  $\alpha_2 \approx 112.7^\circ$  and  $\alpha_3 \approx 113.7^\circ$ ). Throughout the transformation, the *b/a* ratio remains at its initial value of 1.73 ( $\pm 0.02$ ), reflecting the symmetries of the loading and the lattice. The transformation completes at a strain of 8.5%. Further loading causes the elastic stretching of the BCT-4 structure ( $C \rightarrow D$ ) and culminates in the eventual failure at a strain of 16.9% (point E).

To analyze the stability of the WZ and BCT-4 structures, unloading is performed from points B and D which correspond, respectively, to the states prior to the transformation initiation and failure initiation of the nanorod. The unloading path from B coincides with the loading path, confirming that the deformation from A to B is indeed the elastic response of the WZ structured nanorod. Unloading from D also results in the elastic recovery of the stretched BCT-4 structure and continued unloading beyond the transformation completion strain (point C) does not result in a reverse transformation back to WZ. Instead, the nanorod

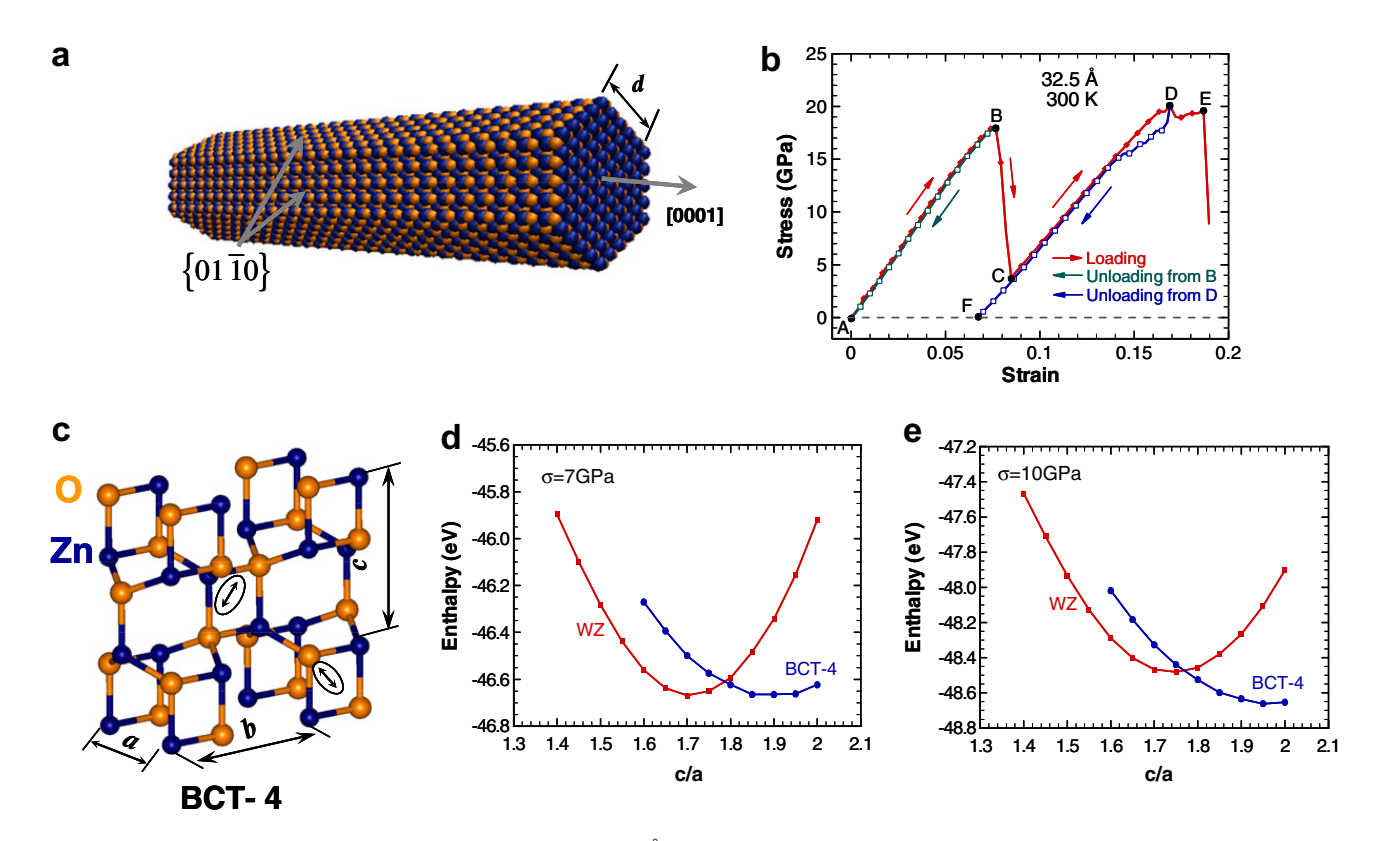


Fig. 3. (a) Configuration of a [0001] nanorod with d = 32.5 Å, (b) stress-strain curve of this nanorod at 300 K during loading and unloading, (c) newly discovered body-centered-tetragonal with four atom rings (BCT-4) structure, (d) enthalpy (per 4 Zn-O pairs) as a function of c/a obtained from DFT calculations for b/a = 1.73 at a tensile stresses of  $\sigma_c = 7$  GPa, and (e) enthalpy map at  $\sigma_c = 10$  GPa.

retains the BCT-4 structure when the stress is reduced to zero [F in Fig. 3b]. The residual strain at F in Fig. 3b is 6.8% according to both MD and DFT. It reflects the dimensional difference between the unstressed WZ and BCT-4 structures in the [0001] direction. This unstressed BCT-4 structure corresponds to the "ideal" BCT-4 structure predicted by the DFT calculations with b/a = c/a = 1.73.

Fig. 3d and e show the enthalpy values (eV per 4 Zn–O pairs) for both WZ and BCT-4 with b/a = 1.73 at  $\sigma = 7$  and 10 GPa. At any stress level, each structure has its own enthalpy minimum. The first minimum ( $H_{\rm min}^{\rm WZ}$ ) is in the vicinity of  $c/a \approx 1.6$  which corresponds to a WZ structure with lattice parameters slightly different from those at zero stress and the second minimum ( $H_{\rm min}^{\rm BCT-4}$ ) is in the vicinity of  $c/a \approx 1.7$ –1.9 which corresponds to the BCT-4 structure. At a stress of 7 GPa,  $H_{\rm min}^{\rm WZ}$  and  $H_{\rm min}^{\rm BCT-4}$  become comparable, indicating that WZ and BCT-4 are equally favored. This value of stress corresponds to the equilibrium transition stress for the two phases. At 10 GPa [Fig. 3c],  $H_{\rm min}^{\rm BCT-4}$  is lower than  $H_{\rm min}^{\rm WZ}$  and BCT-4 is clearly favored. Further increases in stress result in a higher driving force for and the eventual initiation of the phase transformation into the BCT-4 structure as  $H_{\rm min}^{\rm BCT-4}$  becomes progressively lower than  $H_{\rm min}^{\rm WZ}$ . The gradual evolution of the local enthalpy minimum for the BCT-4 at  $\sigma = 0$  into a global minimum as stress increases confirms that the phase transformation is indeed favorable.

# 3.4. Hydrostatic compression

Fig. 4a and b show the initial WZ and transformed RS structures for ZnO. The corresponding pressure—dilatation relation is shown in Fig. 4c. Three distinctive stages of response during loading (A  $\rightarrow$  B, B  $\rightarrow$  C and C  $\rightarrow$  D) and unloading (D  $\rightarrow$  E, E  $\rightarrow$  F and F  $\rightarrow$  G) are observed. During loading, the first stage (A  $\rightarrow$  B) corresponds to the elastic deformation of the WZ structure. The precipitous drop in pressure at p = 9.4 GPa is associated with the transformation of the initial WZ structure to the RS structure. Crystallographically, the

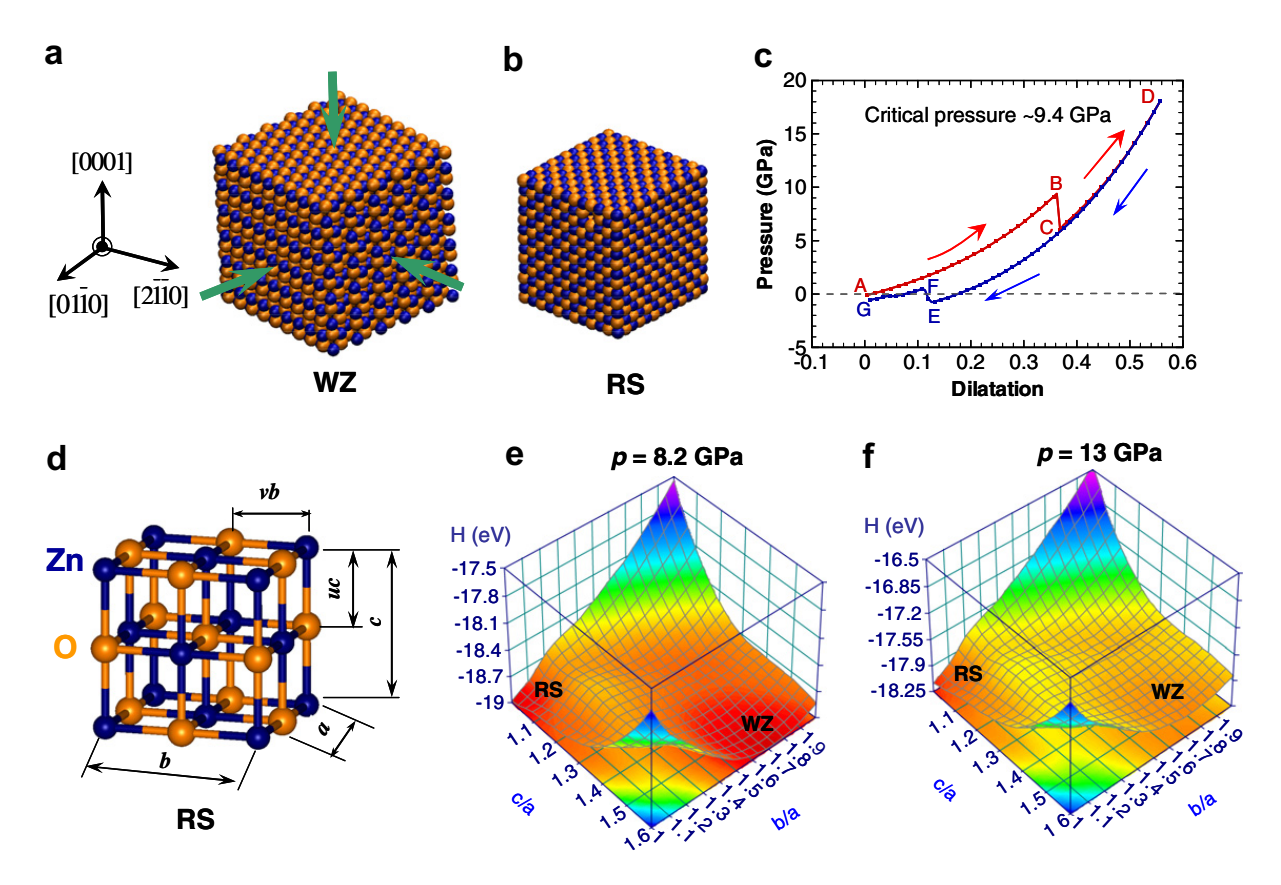


Fig. 4. (a) Bulk ZnO with the WZ structure under hydrostatic compression, (b) the RS structure as a result of the WZ-to-RS transformation, (c) pressure–dilatation relation of bulk ZnO during loading and unloading at 300 K, (d) lattice structure of the RS phase, (e) enthalpy surface obtained from DFT calculations for a hydrostatic pressure of p = 8.22 GPa, and (f) enthalpy surface for p = 13 GPa.

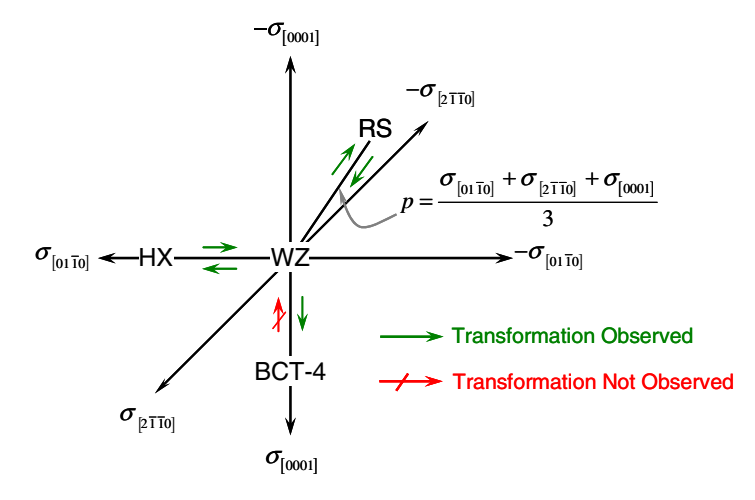


Fig. 5. Crystalline structure–load triaxiality map showing the relationship between applied loading and the resulting polymorphs of ZnO.

transformation proceeds such that both u and v change to 0.5 and the b/a and c/a ratios become unity [Fig. 4d]. Consequently, the RS structure has a six-fold coordination and belongs to the  $Fm\bar{3}m$  space group. The transformation pressure observed here is consistent with experimental measurements in the range of 8.7–9.1 GPa (Desgreniers, 1998; Karzel et al., 1996). These values are higher than the phase equilibrium stress predicted by first-principles calculations (6.6–8.5 GPa) (Jaffe and Hess, 1993; Jaffe et al., 2000; Limpijumnong and Jungthawan, 2004). The difference is that, while the MD and experimental values are actual transformation stresses which reflect the effect of the energy barrier between the WZ and RS phases, the DFT phase equilibrium stress only indicates the level of stress at which the two phases are equally favored but does not relate to the stress required to overcome the energy barrier and activate the transformation.

Upon transformation completion, further increase in pressure results in the elastic deformation of the RS phase. Unloading is carried out from various stages of deformation of the RS phase to analyze the reversibility of the transformation. Specifically, unloading from point D along the loading path results in the recovery of the elastic deformation of the RS phase. Decrease in pressure beyond the transformation initiation point (B) does not result in the reverse transformation. Instead, the RS structure remains upon complete unloading. This retention of the RS structure upon full unloading has been reported in experiments (Recio et al., 1998). However, a spontaneous reverse transformation has also been observed in experiments (Mujica et al., 2003). Both sets of experimental results are reasonable because in experiments temperature is controlled only in an average sense and different experiments are carried out at different temperatures. Excess thermal energy in high temperature regions can allow the energy barrier between the RS and WZ structures to be overcome, resulting in the reverse RS-to-WZ transformation upon unloading. Furthermore, in experiments, defects such as grain boundaries in polycrystalline ZnO samples can act as potential nucleation sites for the reverse transformation and this effect is not considered in the calculations. In the simulations, the RS structure can easily revert to the WZ structure upon the application of a small negative hydrostatic pressure  $(E \to F)$ , leading to full elastic recovery of the volumetric strain  $(F \to G)$ .

Fig. 4e and f show the enthalpy landscapes for p=8.22 and 13 GPa, respectively. Similar to what is seen for the HX and BCT-4 transformations, there are two minima; one corresponds to WZ ( $H_{\rm min}^{\rm WZ}$ ,  $cla\approx 1.6$  and  $bla\approx 1.6$ ) and the other corresponds to RS ( $H_{\rm min}^{\rm RS}$ ,  $cla\approx 1.0$  and  $bla\approx 1.0$ ). At p=8.22 GPa,  $H_{\rm min}^{\rm WZ}=H_{\rm min}^{\rm RS}$  and WZ and RS are equally favored. This value of pressure is the phase equilibrium pressure for ZnO. As the pressure is increased to 13 GPa,  $H_{\rm min}^{\rm RS}$  becomes much lower than  $H_{\rm min}^{\rm WZ}$  and the transformation to RS is energetically favored.

# 4. Summary

The identification of the novel HX and BCT-4 crystalline structures and the characterization of the WZ-to-HX and WZ-to-BCT-4 phase transformations lead to a more complete understanding of the nature of

polymorphism in ZnO and its dependence on load triaxiality. Obviously, polymorphism is much more pronounced in ZnO than previously understood and load triaxiality plays a very significant role in determining the structures. Fundamentally, this complexity is a reflection of the anisotropy and tension–compression asymmetry embedded in the atomic bonding and crystalline structures. It is possible to construct a crystalline structure—load triaxiality map for ZnO, as shown in Fig. 5. Among the previously well known phases, WZ is the most stable and naturally occurring phase and RS is observed under hydrostatic compressive conditions. Both BCT-4 and HX are stabilized under uniaxial loading, with HX occurring under tension along the  $[01\bar{1}0]$  and BCT-4 occurring under tension along the [0001] direction.

# Acknowledgement

Support from NSF (CMS9984298) and NSFC (10772012, 10432050, and 10528205) is acknowledged. SL and KS are supported by TRF (BRG4880015 and PHD/0264/2545) and CHE (CHE-RES-RG "Theoretical Physics"). Computations are carried out at the NAVO, ARL, AHPCRC & ASC MSRCs.

# References

Binks, D.J., Grimes, R.W., 1993. Incorporation of monovalent ions in ZnO and their influence on varistor degradation. J. Amer. Cer. Soc. 76, 2370–2372.

Desgreniers, S., 1998. High-density phases of ZnO: Structural and compressive parameters. Phys. Rev. B 58, 14102-14105.

Diao, J. et al., 2004. Surface stress driven reorientation of gold nanowires. Phys. Rev. B 70, 075413.

Haile, J.M., 1997. Molecular Dynamics Simulation. Wiley Interscience, New York.

Jaffe, J.E., Hess, A.C., 1993. Hartree-Fock study of phase changes in ZnO at high pressure. Phys. Rev. B 48, 7903-7909.

Jaffe, J.E. et al., 2000. LDA and CGA calculations for high-pressure phase transition in ZnO and MgO. Phys. Rev. B 62, 1660-1665.

Karzel, H. et al., 1996. Lattice dynamics and hyperfine interactions in ZnO and ZnSe at high external pressures. Phys. Rev. B 53, 11425–11438.

Kresse, G., Furthmüller, J., 1996. Efficiency of ab initio total energy calculations for metals and semiconductors using a plane-wave basis set. Comp. Mat. Sci. 6, 15–50.

Kulkarni, A.J. et al., 2005. Orientation and size dependence of the elastic properties of ZnO nanobelts. Nanotechnology 16, 2749–2756. Kulkarni, A.J. et al., 2006. Novel phase transformation in ZnO nanowires under tensile loading. Phys. Rev. Lett. 97, 105501–105504, 105502.

Liang, W., Zhou, M., 2006. Atomistic simulations reveal shape memory of fcc metal nanowires. Phys. Rev. B 73, 115401–115411, 115409. Limpijumnong, S., Jungthawan, S., 2004. First-principles study of the wurtzite-to-rocksalt homogeneous transformation in ZnO: A case of a low-transformation barrier. Phys. Rev. B 70, 054101–054104, 054104.

Melchionna, S. et al., 1993. Hoover NPT dynamics for systems varying in shape and size. Mol. Phys. 78, 533-544.

Mujica, A. et al., 2003. High-pressure phases of group-IV, III-V, and II-VI compounds. Rev. Mod. Phys. 75, 863.

Ozgur, U. et al., 2005. A comprehensive review of ZnO materials and devices. J. Appl. Phys. 98, 041301.

Recio, J.M. et al., 1998. Compressibility of the high-pressure rocksalt phase of ZnO. Phys. Rev. B 58, 8949-8954.

Spearot, D. et al., 2005. Nucleation of dislocations from [001] bicrystal interfaces in aluminum. Acta Mat. 53, 3579-3589.

Vanderbilt, D., 1990. Soft self-consistent pseudopotentials in a generalized eigenvalue formalism. Phys. Rev. B 41, 7892.

Wang, J. et al., accepted for publication. Molecular dynamics and density functional studies of a body-centered-tetragonal polymorph of ZnO. Phys. Rev. B.

Wang, Z.L., 2004. Zinc oxide nanostructures: growth, properties and applications. J. Phys.:Cond. Matt. 16, R829-R858.

Wolf, D. et al., 1999. Exact method for the simulation of Coulombic systems by spherically truncated, pairwise r<sup>-1</sup> summation. J. Chem. Phys. 110, 8254–8282.

Zhou, M., 2003. A new look at the atomic level virial stress: on continuum-molecular system equivalence. In: Proceedings of the Royal Society of London 459, 2347–2392.